Université d'Ottawa · University of Ottawa

Université d'Ottawa · University of Ottawa

FACULTÉ DE ÉTUDES SUPÉRIEURES ET POSTDOCTORALES

FACULTY OF GRADUATE AND POSTDOCTORAL STUDIES

Sébastien DELORME

AUTEUR DE LA THÈSE - AUTHOR OF THESIS

Ph.D. (Mechanical Engineering)

GRADE - DEGREE

Department of Mechanical Engineering

FACULTÉ, ÉCOLE, DÉPARTEMENT - FACULTY, SCHOOL, DEPARTMENT

TITRE DE LA THÈSE - TITLE OF THE THESIS

Biomechanical Analysis of Ankle Kinematics in Snowboarding

S. Tavoularis

DIRECTEUR DE LA THÈSE - THESIS SUPERVISOR

M. Lamontagne

CO-DIRECTEUR DE LA THÈSE - THESIS CO-SUPERVISOR

EXAMINATEURS DE LA THÈSE - THESIS EXAMINERS

J. Kofman

T. Oxland

D. Redekop

D. Russell

J.-M. De Koninck, Ph.D

LE DOYEN DE LA FACULTÉ DES ÉTUDES SUPÉRIEURES ET POSTDOCTORALES

DEAN OF THE FACULTY OF GRADUATE AND POSTDOCTORAL STUDIES

Biomechanical Analysis of Ankle Kinematics and Ligament Strain in Snowboarding

By Sébastien Delorme

A Thesis submitted to
The University of Ottawa in Partial Fulfillment of the Requirement
for the Doctor of Philosophy in Mechanical Engineering

January 2004

Department of Mechanical Engineering, University of Ottawa
Ottawa-Carleton Institute for Mechanical and Aerospace Engineering

Your file Votre référence
ISBN: 0-494-01691-4
Our file Notre référence
ISBN: 0-494-01691-4

Abstract

Because snowboarders are known to injure their ankles more often than alpine skiers, it has been postulated that stiffer snowboard boots would provide better protection to the ankle ligaments than current soft boots do.

To test this hypothesis, we have measured the kinematics of the feet and lower legs of five snowboarders riding down a course of 10 gates on a ski hill using an electromagnetic motion tracking system. Results were obtained with each snowboarder wearing soft boots and stiffer step-in boots. The measurements were expressed in anatomically relevant rotations of the ankle joint complex.

Two models were developed to predict ligament strains from rotations of the ankle joint complex: 1) a statistical model using published ligament strain measured on cadaver specimens at various combinations of ankle rotations as an interpolation and extrapolation table to predict strains in two ankle ligaments at the rotations measured during the snowboarding trials; 2) a personalized 2-degrees-of-freedom kinematic model of the ankle joint complex, based on the Denavit-Hartenberg formulation of serial-link manipulators, to predict strains in five ankle ligaments from the relative position of the shank and foot.

The experimental results showed that the left and right ankles are asymmetrically rotated, mostly in dorsiflexion, eversion and external rotation. Compared to step-in boots and bindings, soft boots and strap bindings allowed more rotation of the ankle joint complex and more strain in the anterior talofibular ligament, according to the statistical model. The kinematic model was not sensitive enough to detect differences in ligament strains between the 2 types of equipment. A functional determination of the axes of

rotation of the talocrural and subtalar joints could further improve the predictions of this model.

This is the first known study to document experimentally the kinematics of snowboarding. It generally confirms the expectation that softer boots allow significantly wider ranges of ankle rotation and ligament strain.

Acknowledgements

This research was funded by the *Fonds québécois de la recherche sur la nature et les technologies*, the *Natural Sciences and Engineering Research Council of Canada*, and the University of Ottawa Faculty of Health Sciences Development Fund.

I would first like to thank my co-supervisors Mario Lamontagne and Stavros Tavoularis for their constant support, precious advices and wise direction throughout the project.

I would also like to thank snowboard instructor Robert Joncas, for his tremendous help during the winter 2002 experiments at the Bromont ski resort, not only for recruiting volunteers for the experiment but also for taking care of the logistics and guaranteeing the collaboration of the Bromont staff and snowboard instructors.

I would also like to thank: Christian Charrette, director of the Bromont ski school, for providing ski-lift tickets at the Bromont ski resort; Christian Giguère, associate professor at the School of Rehabilitation Sciences, for lending the Fastrak system; Jacques de Guise, professor at École de Technologie Supérieure, for providing spare sensors; Gaétan Schnob, from the Faculty of Health Sciences, for his technical help with the electronics; Dany Lafontaine and Daniel Théorêt, from the Biomechanical Research on Hockey Laboratory, for their help during the winter 2001 pre-experiments; Serge Van Sin Jan, from University of Brussels, and the VAKHUM project (Virtual Animation of the Kinematics of the Human for Industrial, Educational and Research Purposes) for providing CT-scan images; and all the volunteers who participated in the experiment.

Finally, I would like to specially thank Raymond Gauvin, my father André Delorme, and my wife Chantal Gauvin, not only for their precious advices, but also for supporting me in every way possible throughout this project, and giving me the will to achieve this thesis.

Table of contents

List of Tables

List of Figures

List of abbreviations

2D: two-dimensional

3D: three-dimensional

AA: abduction/adduction (Figure 2-9)

AJC: ankle joint complex

ATFL: anterior talofibular ligament (Figure 2-8)

az: azimuth (Figure 3-9)

BECS: bone-embedded coordinate system (Figure 3-12)

Ca: calcaneus (Figure 2-8)

CA: upper ridge of the calcaneus posterior surface (Figure 3-7)

CFL: calcaneofibular ligament (Figure 2-8)

DL: deltoid ligament (Figure 2-8)

DOF: degree of freedom

DP: dorsiflexion/plantar flexion (Figure 2-9)

FM: medial aspect of first metatarsal head (Figure 3-7)

EI: eversion/inversion (Figure 2-9)

el: elevation (Figure 3-9)

GCS: global coordinate system (Figure 3-12)

HF: apex of the head of the fibula (Figure 3-7)

JCS: joint coordinate system (Figure 3-12)

LM:	distal apex of the lateral malleolus (Figure 3-7)
MM:	distal apex of the medial malleolus (Figure 3-7)
PTFL:	posterior talofibular ligament (Figure 2-8)
RMS:	root mean square
ro:	roll (Figure 3-9)
SB:	snowboarding
SM:	dorsal aspect of second metatarsal head (Figure 3-7)
SP:	supination/pronation (Figure 2-9)
STTL:	superficial tibiotalar ligament (Figure 2-8)
Ta:	talus (Figure 2-8)
TCS:	technical coordinate system (Figure 3-12)
TCL:	tibiocalcaneal ligament (Figure 2-8)
TiFi:	tibia-fibula (Figure 2-8)
TT:	prominence of the tibial tuberosity (Figure 3-7)
VM:	lateral aspect of fifth metatarsal head (Figure 3-7)

Glossary

Abduction: rotation of the foot in the transverse plane consisting of pointing the foot laterally (Section 2.2.3, Figure 2-9).

Adduction: rotation of the foot in the transverse plane consisting of pointing the foot medially (Section 2.2.3, Figure 2-9).

Aetiology: the study of the causes of diseases or health problems (Section 2.4).

Alpine: in snowboarding, riding style that consists of turning while leaning into the curve close to the ground, in a slalom course or in powder snow (Section 2.1.2).

Anterior talofibular ligament (ATFL): lateral ankle ligament going from the talus to the fibula, almost horizontally (Section 2.2.2, Figure 2-8).

Calcaneofibular ligament (CFL): lateral ankle ligament going from the calcaneus to the fibula (Section 2.2.2, Figure 2-8).

Calcaneus: heel bone (Section 2.2.1, Figure 2-8).

Carving: see Alpine.

Deltoid ligament (DL): medial ankle ligament joining the tibia to the calcaneus, talus and navicular bones (Section 2.2.2, Figure 2-8).

Distal: the part of an appendix or organ that is furthest from its attachment point. Opposite: proximal (Section A.2).

Dorsiflexion: rotation of the foot in the sagittal plane consisting of pointing the foot towards the knee (Section 2.2.3, Figure 2-9).

Epidemiology: the part of medicine that studies the different factors conditioning the apparition, the frequency, the diffusion mode and the evolution of diseases or health problems affecting a group of individuals (Section 2.4).

Eversion: rotation of the foot consisting of a combination of abduction, pronation and dorsiflexion (Section 2.2.3, Figure 2-9).

External rotation: see abduction.

Fastrak: company product name of an instrument that can track the position and orientation of up to four sensors using electromagnetic fields (Section D.1, Figure D-1).

Fibula: small outer shinbone, lateral to the tibia (Section 2.2.1, Figure 2-8).

Forward leg: in snowboarding, the leg whose foot is attached closest to the nose of the snowboard.

Freeride: in snowboarding, riding style that is a mix between freestyle and alpine. Freeride snowboards are all-around boards that can be used for tricks, powder snow or carving (Section 2.1.2).

Freestyle: in snowboarding, riding style that involves performing tricks, jumps and other aerial manoeuvres in a mogul hill, a snow "half pipe" or a snow park (Section 2.1.2).

Frontal plane: the vertical plane perpendicular to the sagittal plane (Section A.1, Figure A-1).

Heel turn: in snowboarding, manoeuvre consisting of leaning backwards and turning on the snowboard edge on the heel side.

Hindfoot: the portion of the foot from the midSection to the heel.

Hyper: more than physiologically normal (opposite: hypo).

Hypo: less than physiologically normal (opposite: hyper).

***In vitro*:** outside the living body and in an artificial environment (opposite: *in vivo*). Experiments performed on a body part removed from the rest of the body are done *in vitro*.

***In vivo*:** in a living body (opposite: *in vitro*). Experiments performed on living subjects, either conscious or under anaesthesia, are done *in vivo*.

Insertion (of a ligament): distal point of attachment of a ligament to a bone.

Internal rotation: see adduction.

Inversion: rotation of the foot consisting of a combination of adduction, supination and plantar flexion (Section 2.2.3, Figure 2-9).

Lateral: away from the sagittal plane of the body. Opposite: medial (Section A.2).

Malleolus: outer bony prominence on the medial side of the distal tibia and on the lateral side of the distal fibula (Section 2.2.1, Figure 2-8).

Medial: towards the sagittal plane of the body. Opposite: lateral (Section A.2).

Origin (of a ligament): proximal point of attachment of a ligament to a bone.

Plantar flexion: rotation of the foot in the sagittal plane consisting of pointing the foot away from the knee (Section 2.2.3, Figure 2-9).

Posterior talofibular ligament (PTFL): lateral ankle ligament going from the talus to the fibula, almost vertically (Section 2.2.2, Figure 2-8).

Process: bony prominence.

Pronation: rotation of the foot in the frontal plane consisting of turning the foot outward (Section 2.2.3, Figure 2-9).

Proximal: the part of an appendix or organ that is closest to its attachment point. Opposite: distal (Section A.2).

Sagittal plane: the vertical plane that divides the human body into "symmetric" (apart from internal organ locations) right and left halves (Section A.1, Figure A-1).

Sensor: the receiving antenna of the electromagnetic position sensors system (Fastrak). The sensor reports its position and orientation with respect to the coordinate system defined on the source (Section D.1, Figure D-1).

Source: the emitting antenna of the electromagnetic position sensors system (Fastrak). All sensor measurements are done in a coordinate system defined on the source (Section D.1, Figure D-1).

Static metallic noise: a static perturbation of the electromagnetic fields generated by the Fastrak source, often caused by the presence of ferromagnetic or highly conductive materials in the vicinity of the source. This perturbation translates into measurement errors by the sensors (Section D.1, Figure G-2).

Stylus: a plastic rod with a sharp stainless steel tip that can be rigidly attached to a Fastrak sensor and used to measure points located at its tip (Section F.1, Figure F-1).

Subtalar joint: joint formed by the talus and the calcaneus (Section 2.2.1, Figure 2-8).

Supination: rotation of the foot in the frontal plane consisting of turning the foot inward (Section 2.2.3, Figure 2-9).

Talocrural joint: the joint formed by the tibia, the fibula and the talus; true ankle joint (Section 2.2.1, Figure 2-8).

Talus: foot bone between the tibia, fibula and calcaneus, which is involved in both the talocrural and the subtalar joints (Section 2.2.1, Figure 2-8).

Tibia: main shinbone (Section 2.2.1, Figure 2-8).

Toe turn: in snowboarding, manoeuvre consisting of leaning forward and turning on the snowboard edge on the toe side.

Transverse plane: any plane perpendicular to both the sagittal and frontal planes (Section A.1, Figure A-1).

1 Introduction

1.1 Motivation for the present study

The human ankle joint is the one that most often sustains ligament sprains, mainly during sport activities. Ankle sprains are responsible for the second greatest number of days lost from work due to injury[39]. The incidence of injuries to the collateral ligaments of the ankle is as high as one in 10000 people per day[21].

Between 1989 and 2001, the number of snowboarders in the United States more than tripled, while the number of alpine skiers decreased by almost one third[1]. In 2001, snowboarders made up 41% of those using the slopes in the United States, making snowboarding the world's fastest growing winter sport. The incidence of trauma from snowboarding is 2 to 6 for every 1000 medical examinations, which is slightly higher than that in alpine skiing[19,68,177,178,179]. In addition to the physical and psychological damage to the injured, snow-sport related injuries result in significant financial costs for the health care system and the individuals.

Since the early years of snowboarding, significant advances have been made in snowboard equipment design. Current boards have metal edges, like those of skis, and specifically designed bindings and boots. However, there is currently no established standard for the mounting of the boot to the binding, with each binding manufacturer producing a system that fits essentially only its own boots. Unlike ski bindings, none of the bindings used in snowboarding automatically release when a force exceeding a certain magnitude is exerted on them. Despite the existence of hard boots, like the ones used in alpine skiing, soft boots are still broadly used in snowboarding. These boots provide little protection to the ankle but allow a wide range of movement, which is necessary to perform aerial manoeuvres.

With consideration to injury patterns, snowboarders are more prone to ankle injuries than alpine skiers are[19,170,179]. Also, snowboarders with soft boots have a higher incidence of ankle injuries than snowboarders with hard boots have[19,68,97,151,152,179]. This led some scientists to suggest two possible ways to reduce the risk of ankle injuries in snowboarding: 1) using releasable bindings just like those used in alpine skiing[3,45,68,178], and 2) increasing the rigidity or reducing the range of movement of soft boots[45,68,151,152,178,179].

The evolution of snowboard equipment is currently very dynamic but still intuitive. On the one hand, research and development in snowboarding is motivated by:

- the dramatically increasing popularity of snowboarding and
- the high cost of snowboard related injuries.

On the other hand, it is limited by:

- the particular patterns of injuries to the lower limbs associated with the practice of snowboarding and
- the lack of information about the mechanisms causing these injuries.

In view of the above discussion, it is evident that there is a need to document the internal stresses generated in the ankle and to understand their relationship with the type of snowboard equipment used and, ultimately, with ankle injuries.

1.2 Current state of research

Mechanical properties of the ankle have been studied from different perspectives. Some investigators have measured the passive[9,149,133,165,169,181,182,196] and active[7,74,143] ranges of motion of the ankle joint complex and reported physiological limits in the three orthogonal directions. Others have measured the mechanical properties of the ligaments surrounding the ankle joint complex at different strain rates and have observed a viscoelastic behaviour[10,67,144,180,185], although failure strain remains unaffected by strain rate in other animal and human ligaments and tendons[44,113,207]. Three studies have established statistical models to predict ligament strain from ankle rotation[41,144,164].

In alpine skiing, on-field kinematic measurements have been done in 2-D with electrogoniometers[101,115,129,131,136,137,138,157,159] and gyroscopes[101], and in 3-D with videographic techniques[139,170] and electromagnetic motion tracking systems[73], the latter offering the advantage of an unlimited field of measurement. Dynamic measurements of forces acting on ski boots done with strain gauges[131,138] and 6-DOF dynamometers[65,83,101,115,121,122,129,136,142,157,158,159,160,193,198,205,206] were adapted to snowboarding[14]. Commercial off-the-shelf force plates specifically designed for alpine skiing and snowboarding measurements are now available[98]. On-field kinematic measurements in snowboarding have not been reported in the literature.

Kinematic models of the ankle joint were developed based on the assumption of fixed-axis revolute joints [6,109,194] or instantaneous axes of rotation[80,183,194]. Mechanical models have used 3D reconstructions of cadaver or living specimens from biomedical images, and represented the articular surfaces as contact surfaces and ligaments as either elastic[36,209] or viscoelastic elements[111]. The only available mechanical model used for the analysis of snowboarding[63] modeled the ankle in 2-D using torsion springs based on passive stiffness data.

1.3 Objectives and scope of the thesis

The general objective of this work is to better understand the biomechanics of snowboarding and the mechanisms responsible for the associated injuries to the ankle. This would help develop rational strategies for design modifications to snowboard equipment in order to reduce the incidence of ankle injuries and their severity. More specifically, this work will focus on documenting and explaining the effect of snowboard equipment on the strain in ankle ligaments.

In order to realise this objective, three specific objectives are pursued:

1) To document experimentally the kinematics of the lower extremities in snowboarding.

2) To analyze the rotations of the ankle and the strain in its main ligaments.

3) To compare the effects of different designs of snowboard boots and bindings on ankle rotation and ligaments strain.

The study is limited to measuring the lower leg kinematics of 10 human subjects snowboarding down a course of 10 gates on a ski hill. Two types of snowboard equipment were used with each snowboarder, reflecting different boot stiffness and binding ankle support. Kinematics and anatomical landmark measurements are used to calculate ankle three-dimensional rotation, and to predict ligament strains using both a statistical model and a mechanical model. Ankle rotations and ligament strains are compared to physiological limits.

1.4 Organization of the thesis

Chapter 2 presents background information on snowboarding and anatomy, as well as a literature survey on ankle injuries, ankle physiology, experimental measurements in snowboarding, and biomechanical modelling of the ankle. Chapter 3 describes the experimental procedures and instrumentation to measure the kinematics of the ankle. Chapter 4 presents the experimental results. Chapter 5 focuses on biomechanical models developed to predict ligament strains from ankle kinematics. Chapter 6 discusses methodological issues, interprets the experimental results and analyses the predictions of the biomechanical models. Chapter 7 draws conclusions and suggests paths for further research in the area of snowboard injuries.

2 Background and Literature Survey

This chapter first presents background information on snowboarding and ankle anatomy. The extents of the problem of ankle injuries in snowboarding and the proposed improvements to snowboarding equipment are then reviewed from the scientific literature and patents. Finally, previous work on the mechanical properties of the ankle and its ligaments, kinematics and kinetic measurement techniques in skiing and snowboarding, and biomechanical modelling of the ankle joint are summarized.

2.1 Snowboarding

2.1.1 History of the snowboard

Snow-surfing ("snurfing") was invented in the mid-1960's by the American surfer Sherman Poppen. The "Snurfer" (Figure 2-1) was a very simple piece of wood, resembling a single water-ski without bindings. A handle attached to a rope fastened at

Figure 2-1: Left, "snurfer" ad (from www.toyadz.com, reprinted with permission). Right, early snowboard prototypes (from www.bulgariaski.com).

the front and a traction pad were the sole aids to balance.

Through the 1970's, snurfers refined their tools, modifying Sherman's original plywood plank by making it wider and longer and by adding skegs for stability. A "snurf freak" from Vermont, named Jake Burton Carpenter, attached rubber straps to his board for better control. This was a breakthrough that led him to start the Burton Snowboard Company, a forerunner in the snowboard industry. Meanwhile, on the west coast of the United States, skateboard world champion Tom Sims had also begun snowboard production. In the mean time, in New York, Dimitrije Milovich, an engineer, had formed a company called "Winterstick" to make epoxy/fibreglass boards.

This intuitive tinkering, continuing over the next ten years, led to one innovation that revolutionized the sport: highback bindings. With highbacks, riders could control a snowboard on hard-packed snow and safely ride on resort terrain.

Snowboarding is now the world's fastest growing winter sport[85,130] (Figure 2-2). In 2001, it was estimated that snowboarders made up 41% of those using the slopes[1].

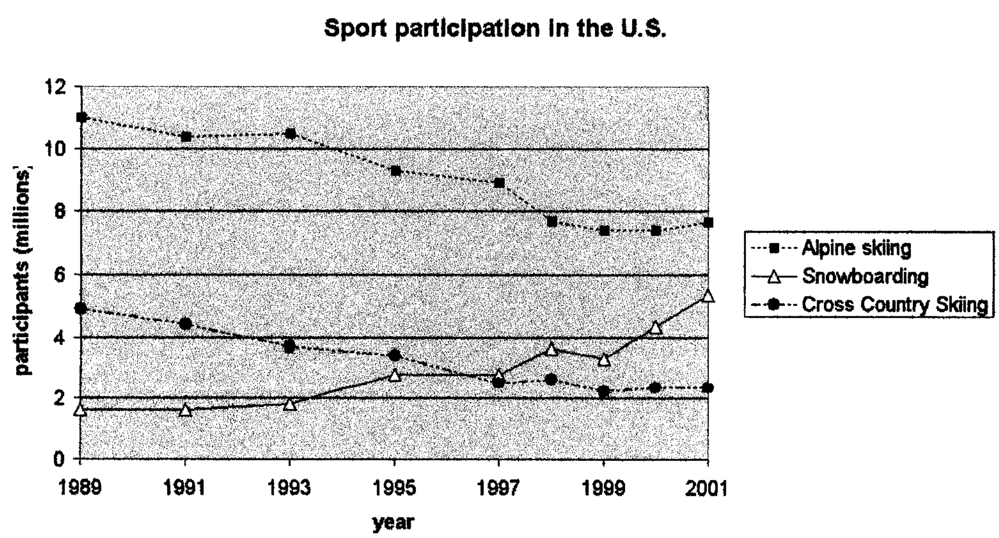

Figure 2-2: Snow sport participation in the U.S from 1989 to 2001[1].

2.1.2 Snowboarding equipment

The basic snowboard equipment includes a board, two bindings and a pair of boots. The snowboarder stands sideways on the board, with his/her boots attached to the board via the bindings. The snowboarder stance is similar to the surfer or skateboarder stances (Figure 2-3).

Snowboard equipment has evolved and become specialized, according to the type of snowboarding activity. Board length, width, sidecut and stiffness, binding design and boot stiffness vary.

"Alpine" snowboarding involves racing or "carving", i.e. turning while leaning into the curve close to the ground (Figure 2-4a), in a slalom course or in powder snow. "Freestyle" involves performing tricks, jumps and other aerial manoeuvres (Figure 2-4b) in a mogul hill, a snow "half pipe" or a snow park, where the snowboarder will find all kinds of obstacles (e.g. a school bus, a picnic table, etc.) to perform stunts over. "Freeride" snowboarding is a mix of freestyle and alpine snowboarding.

Snowboarders who practice freestyle snowboarding generally prefer a wider, shorter and less stiff board, with a nose at each end, "strap" or "step-in" bindings and soft boots. Snowboarders who practice alpine snowboarding would rather select a longer, stiffer

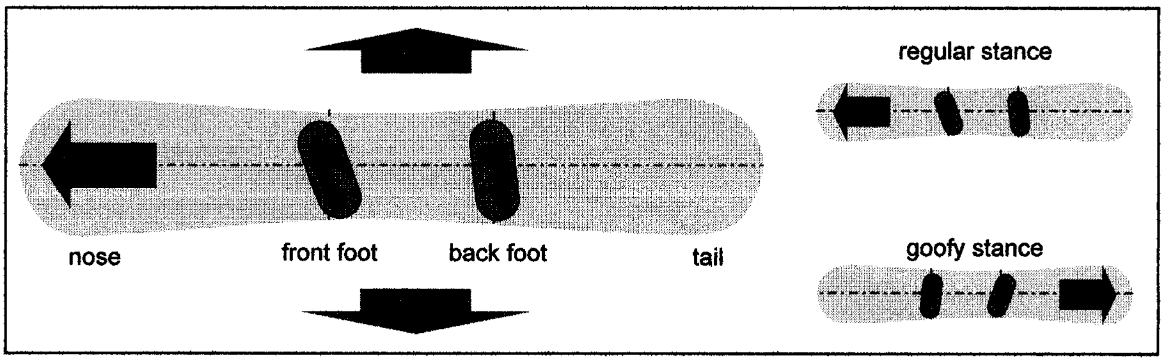

Figure 2-3: Snowboard stance.

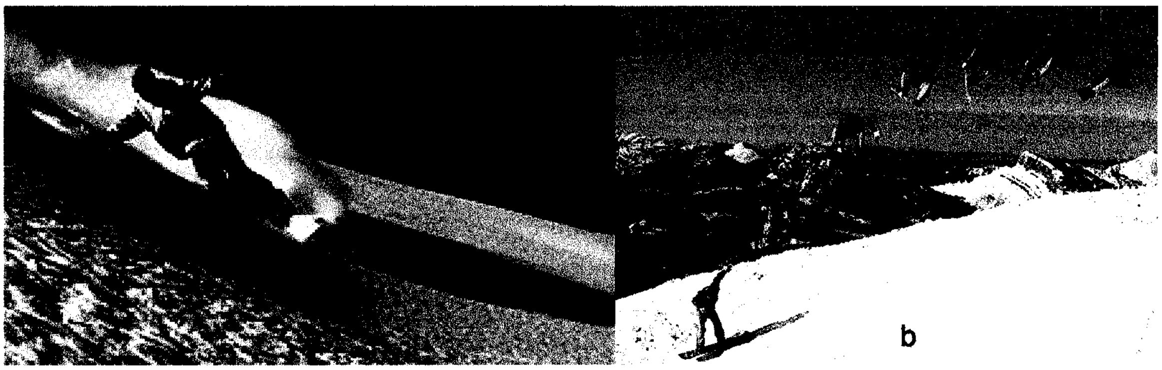

Figure 2-4: Snowboarding styles a) alpine (from www.gorp.com) and b) freestyle (from www.actionreporter.com).

board with "plate" bindings and hard boots.

2.1.2.1 Types of boards

2.1.2.1.1 Freeride

The "freeride" board design (Figure 2-5a) has emerged as the most commonly sold type (60% of the market). It is an all-around board, which can be used for tricks, powder snow, and carving. Like any all-around product, while usable for any of these purposes,

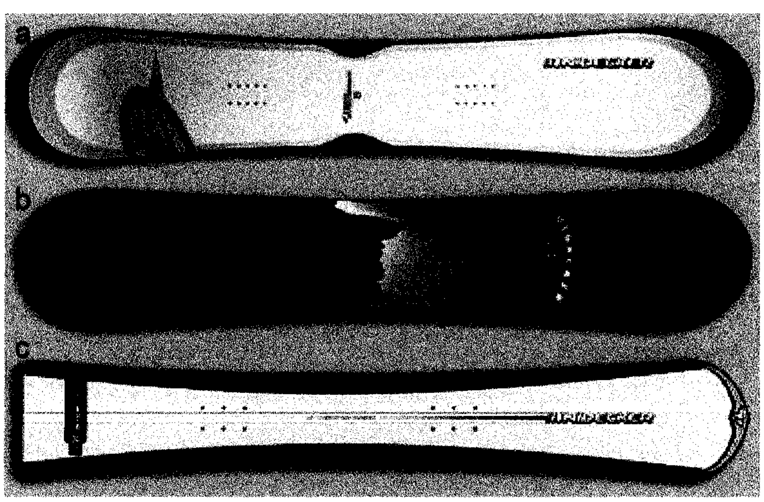

Figure 2-5: Types of snowboards a) freeride, b) freestyle, c) alpine. From www.nidecker.ch, reprinted with permission of Nidecker.

freeride boards typically will not excel at any specific activity.

While freeride boards resemble, in some aspects, freestyle boards, as they both have identical noses and tails, they also have significant differences. In a typical freeride board, the binding inserts are set back toward the tail about 2 cm, to improve their performance and their carving ability in powder; by contrast, on a freestyle board the inserts are perfectly centred. The freeride board's flex pattern also varies along its length. To boost their carving capabilities, freeride boards are stiffer in the tail than in the nose.

2.1.2.1.2 Freestyle

Once the most popular design, "freestyle" boards (Figure 2-5b) now represent 35% of the market. They have an even (symmetrical) flex pattern and a smaller amount of side-cut than the freeride boards. In general, they are easy to identify from their symmetrical "twin tip" designs. This design means that the board can be ridden equally well backwards ("switchstance") as forwards. This type of board excels at all types of tricks. These boards have a centred binding insert pattern. Some models have relatively low "tip/tail heights", which can create problems in deep powder snow.

2.1.2.1.3 Alpine

The "alpine" (carving) boards (Figure 2-5c), which account for less than 5% of the market, are designed for speed. Most of them have a flat tail, like a ski, and a lower shovel than freestyle models. These design characteristics can make them more difficult to ride "switch" (backwards), as the blunt tail can have a tendency to dig into moguls. These boards tend to be stiff with very pronounced side-cuts and a much more narrow overall shape. When placed on edge they can "carve" spectacular tracks.

2.1.2.2 Types of bindings

2.1.2.2.1 Strap bindings

The most common binding style, strap bindings work with all types of soft boots (Figure 2-6). These bindings have two or three adjustable ratchet straps. They are available with a small, medium or large highback, depending on the need for mobility versus support and the size of the boot. Highback bindings are good for freeriders as well as freestylers. Freestylers usually prefer strap bindings with a lower back for more flexibility and mobility. Others use a soft binding that has no base. This puts the boot in contact with the board for more sensitivity.

2.1.2.2.2 Step-in bindings

These increasingly popular bindings do not automatically release in the same way ski bindings do, but they easily fasten the boot to the board without straps. Most step-in bindings are boot-specific, so boots and bindings must be bought together as a system. Currently, eight boot manufacturers have adopted the binding system developed by Switch (San Francisco, CA, USA) as their standard, while others, like K2 and Burton, still

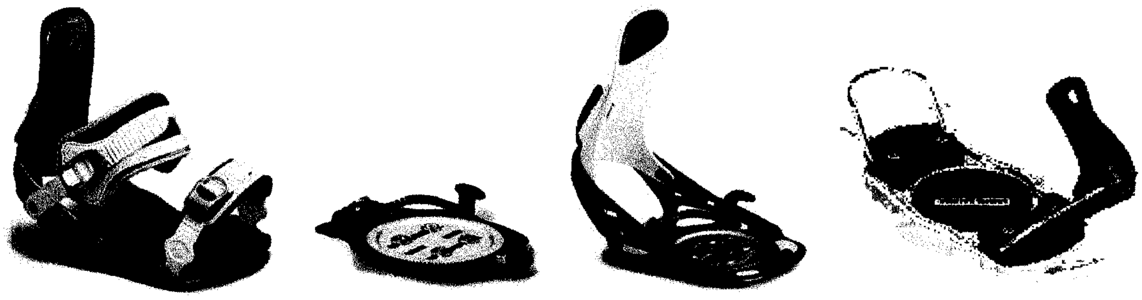

Figure 2-6: From left to right: strap bindings, step-in bindings, step-in bindings with high back, plate bindings. First 3 images from www.k2snowboards.com. Last image from www.nidecker.ch, reprinted with permission of Nidecker.

produce step-in bindings only compatible with their own boots. Some step-in bindings do not have a highback. Instead, compatible boots either have a built-in highback or an external highback for support. Others do have a highback, creating a similar feeling to the strap bindings and allowing the boarder to use a softer boot without the hassle of the straps. Freestylers and freeriders who want the convenience of a step-in system choose these bindings.

2.1.2.2.3 Plate bindings

Most often found on alpine boards, plate bindings are paired with rigid boots that resemble alpine ski boots. A simple clip, or bail, holds the boot on the board and can be released quickly. Some have pivoting turntables. On technical descents, plate bindings with hard boots give excellent edge control, but they do not allow as much lateral flex or mobility. These bindings are usually chosen for racing or carving.

2.1.2.3 Types of boots

Just as there are soft, step-in and plate bindings, there are also soft, step-in and hard boots to match them (Figure 2-7). In addition, boots are associated with riding style. Freestyle usually requires soft, short boots. Freeride requires a boot that is tall and stiff for good support. Alpine riding demands a hard boot for maximum support and control.

2.1.2.3.1 Soft boots

Soft boots are best for half-pipe, freestyle, freeride and jumping. They have a non-rigid outer boot, a padded liner and a deep-treaded sole. They close with straps and/or laces and are flexible. Soft boot bases are rounded at the ends, which makes walking easier when off the board. Freeriders may prefer a stiffer, more supportive soft boot, while freestylers usually like a lighter boot with more mobility.

Figure 2-7: Soft boot (left), step-in boot (middle) and hard boot (right). First 2 pictures from www.k2snowboards.com, last picture from www.startingate.net.

2.1.2.3.2 Step-in boots

Step-in boots look much like soft boots, but they are designed to be compatible with a particular step-in binding. Because a step-in binding has no straps, a step-in boot is stiffer and heavier than the standard soft boot, and it has a specific mechanism for locking into the binding. Most step-in boots have a more rigid sole than soft boots.

2.1.2.3.3 Hard boots

Hard boots are best for high-speed carving on powder and hard snow. They have a plastic outer shell, a rigid sole, thick padded inners, and an overlapping centre tongue. They support the foot, ankle, and lower leg firmly. Hard boots look similar to alpine ski boots, but they have chamfered tips to avoid overhang and permit more bending while doing turns. They are usually adjusted with buckles and clips. Some models allow the shell to be adjusted for flexibility.

2.2 Anatomy of the ankle

Before getting into the detailed anatomy of the ankle, it would be helpful to define some basic anatomical terms (see also Appendix A).

2.2.1 Bones

The ankle is a complex mechanism. What we normally think of as the ankle is actually made up of two joints: the subtalar joint, and the talocrural joint.

The talocrural joint is composed of three bones (Figure 2-8): the tibia (shin bone) which forms the inside, or medial, portion of the ankle; the fibula which forms the lateral, or outside portion of the ankle; and the talus, which is underneath the other two. Beneath the talocrural joint is the second part of the ankle, the subtalar joint, which consists of the talus on top and calcaneus (the heel bone) on the bottom.

The end of the tibia forms the inner bony prominence of the ankle, called the medial malleolus. The outer bony prominence is called the lateral malleolus and is formed by the small outer bone in the foreleg called the fibula. The ability of the joint to follow a fixed path of motion without dislocating depends on the unique structural arrangement of the bones forming the joint and the surrounding ligaments.

2.2.2 Ligaments

Surrounding the bones of the ankle are ligaments, which are fine collagen fibres woven in parallel bundles that provide elasticity and resist tension in one direction of motion. The anatomy of the ligaments may be divided into medial and lateral structures. The three lateral ligaments (Figure 2-8) provide stability by attaching the lateral malleolus to the bones below the ankle joint (talus and calcaneus). These are the following:

- The anterior talofibular ligament (ATFL, from the talus to the fibula).
- The calcaneofibular ligament (CFL, from the calcaneus to the fibula).
- The posterior talofibular ligament (PTFL, from the talus to the fibula).

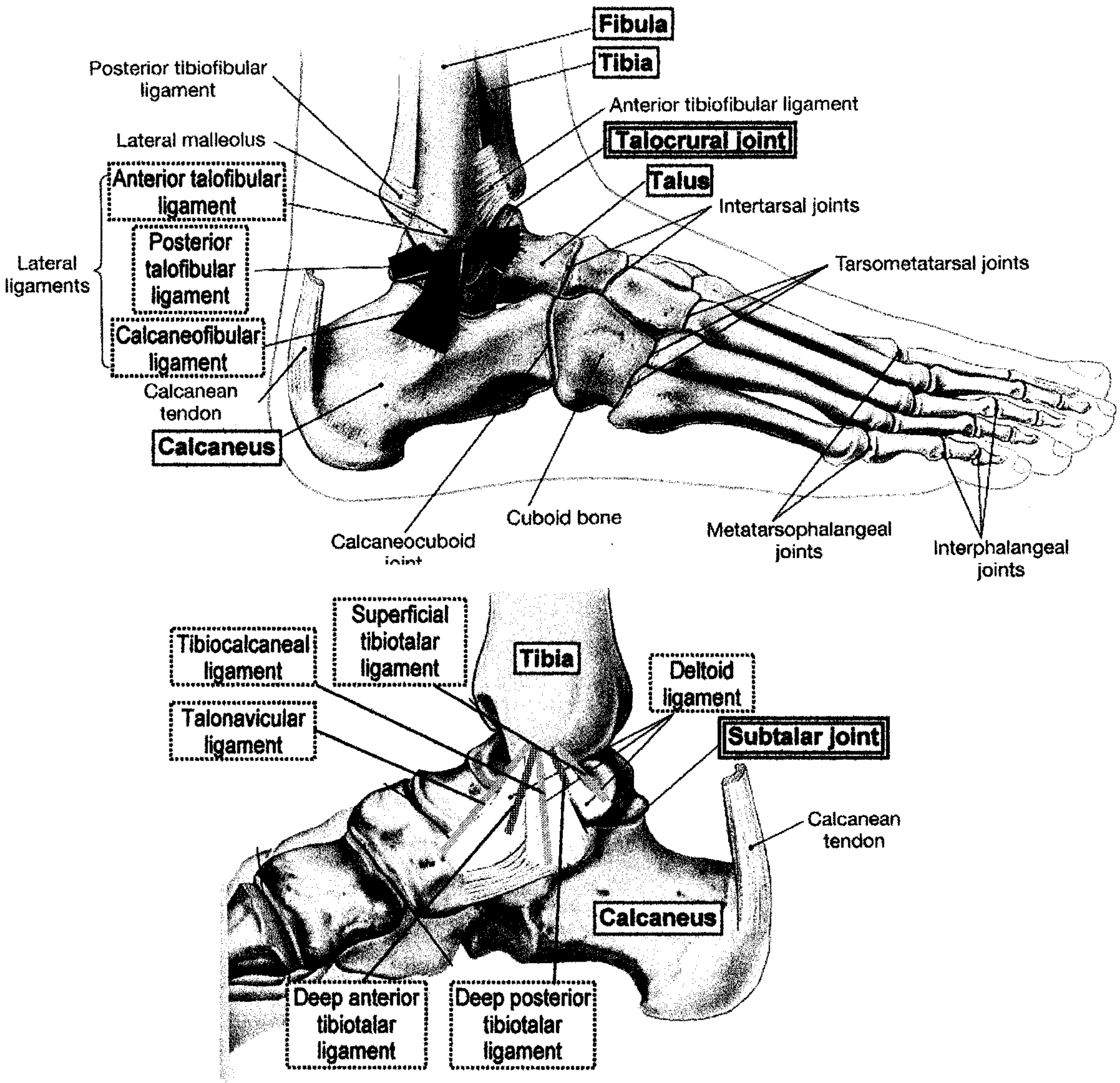

Figure 2-8: Anatomy of the ankle: lateral view (top) and medial view (bottom). Joint labels are framed with a double line, bones with a single line and ligaments with a dotted line (adapted from Martini *et al.*[127], reprinted by permission of Pearson Education, Inc.).

The ATFL keeps the ankle from sliding forward and the CFL keeps the ankle from rolling over on its side.

On the medial side of the ankle (Figure 2-8) is the deltoid ligament complex (DL), which connects the medial malleolus of the tibia to the talus and calcaneus and provides medial stability. Pankovich and Shivaram[148] have identified five distinct fibre bundles in the deltoid ligament complex:

- The talonavicular ligament (TNL, from the talus to the navicular bone).
- The tibiocalcaneal ligament (TCL, from the talus to the calcaneus).
- The superficial tibiotalar ligament (STTL, from the tibia to the talus).
- The deep anterior tibiotalar ligament (DATTL, from the tibia to the talus).
- The deep posterior tibiotalar ligament (DPTTL, from the tibia to the talus).

2.2.3 Joint movements

Some joints can rotate around three mutually perpendicular axes of rotation. For the ankle joint complex, flexion is the rotation in the sagittal plane around the medio-lateral axis (Figure 2-9a). Plantar flexion consists of pointing the foot away from the knee, while dorsiflexion consists of pointing the foot towards the knee. Inversion and eversion are rotations that occur in the frontal plane around the postero-anterior axis (Figure 2-9b). Eversion consists of turning the plantar side of the foot laterally (turning the foot outwards), while inversion consists of turning the plantar side of the foot medially (turning the foot inwards). Although some authors have used pronation and supination to describe these rotations, the International Society of Biomechanics has recently recommended the use of inversion and eversion[204]. Internal and external rotations, also referred to as adduction and abduction, respectively, are rotations in the transverse

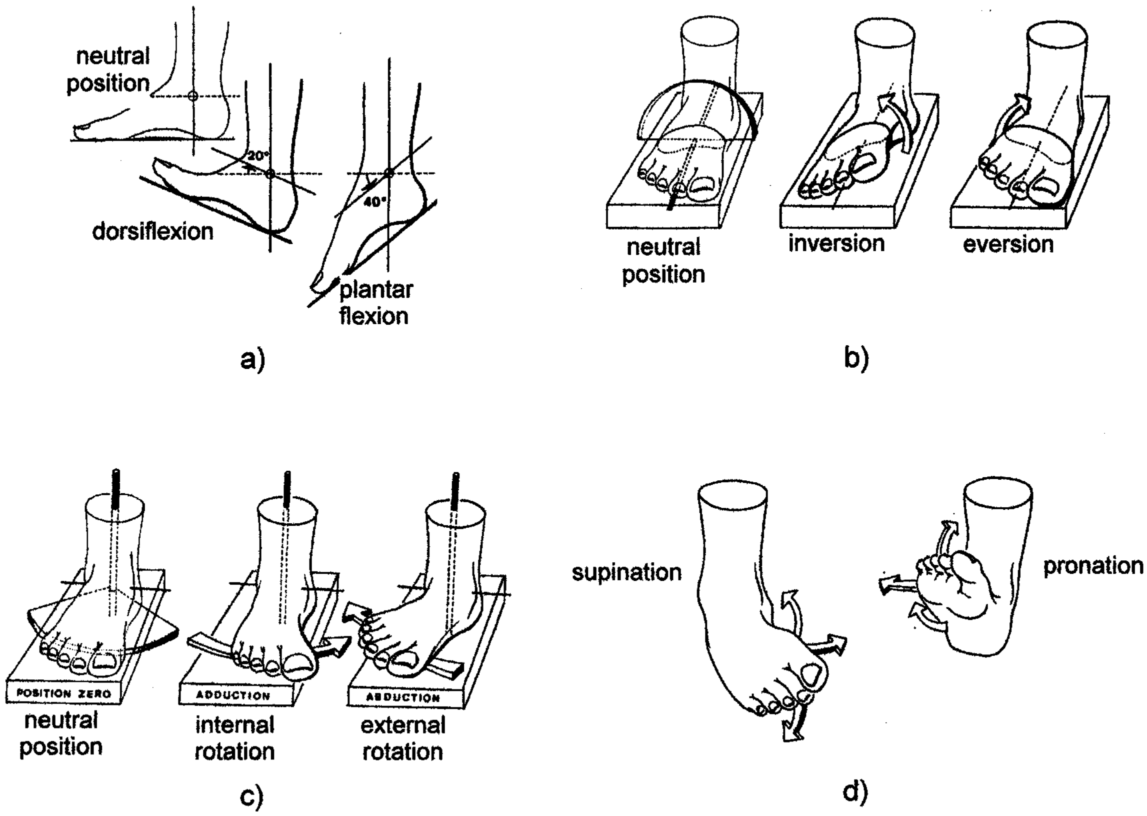

Figure 2-9: Rotations of the ankle; a) dorsiflexion and plantar flexion, b) inversion and eversion, c) internal and external rotation, d) supination and pronation. Images adapted from Castaing *et al.*[34].

plane (Figure 2-9c). Internal rotation (adduction) consists of pointing the foot medially, while external rotation (abduction) consists of pointing the foot laterally.

Supination and pronation are combinations of rotations that naturally occur in the normal foot (Figure 2-9d). Supination is a combination of internal rotation, inversion and plantar flexion. Pronation is a combination of external rotation, eversion and dorsiflexion.

2.2.4 Articular surfaces and physiological axes of rotation

The orthogonal rotations described above were defined by engineers to study the ankle joint complex using three-dimensional Cartesian analysis. Physiologically, the articular surfaces and the ligaments guide the motion about the talocrural and subtalar joints (Figure 2-10).

In the talocrural joint, the concave surface of the distal end of the tibia, called the mortise, fits into the convex surface of the talus, called the trochlea tali (Figure 2-11, a and b). This particular method of articulation makes the talocrural joint somewhat of a

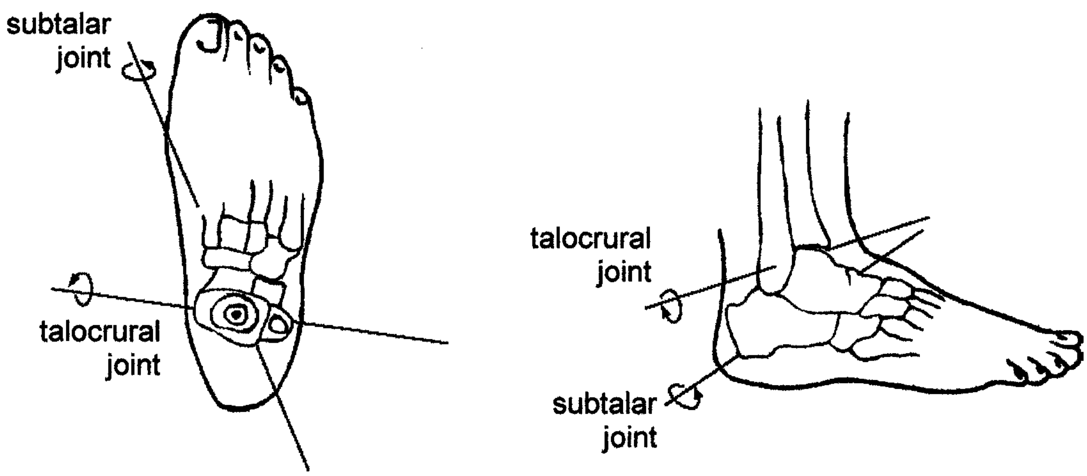

Figure 2-10: Physiological axes of rotation of the ankle joint complex (adapted from Konradsen and Voigt[100], © Blackwell Publishing 2002, with permission).

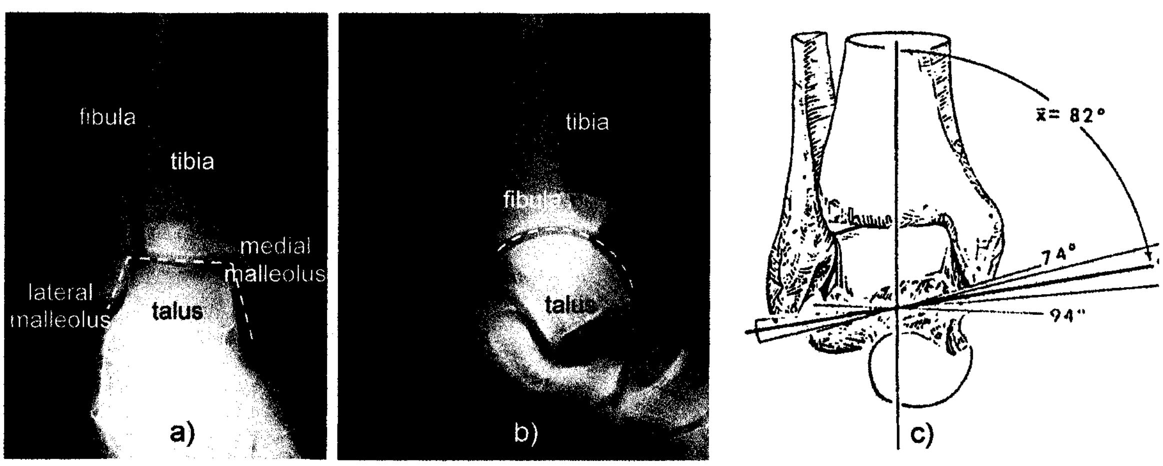

Figure 2-11: Talocrural joint: a) articular surface in frontal view; b) articular surface in sagittal view (adapted from www.rad.washington.edu); c) orientation of the axis of rotation (from Stiehl[188]).

hinge joint, which was first thought to only permit motion about a single axis[86] (Figure 2-11c). Although widely accepted for the description of hindfoot (the portion of the foot from the midsection to the heel) motion[57,59,60,106,135,183] and adopted in many mathematical models of the ankle[58,155,174,187,194], the hypothesis of an ideal hinge joint was weakened by other studies[22,61,109,117,120,161,181] which have shown that the axis of rotation moves continuously throughout the entire range of motion. The medial and lateral malleoli, the easily palpable bony prominences on the sides of the ankle, prevent the talus from medial and lateral motion. The strong collateral ligamentous support and the hard malleoli permit mostly plantar flexion and dorsiflexion of the ankle joint complex, while limiting inversion and eversion.

The subtalar joint is made of three mating articular surfaces on the calcaneus and talus (Figure 2-12a). Functionally, these three articular surfaces act as a single unit and share a common oblique axis of rotation[166] anteriorly oriented on average 42° upward and 16

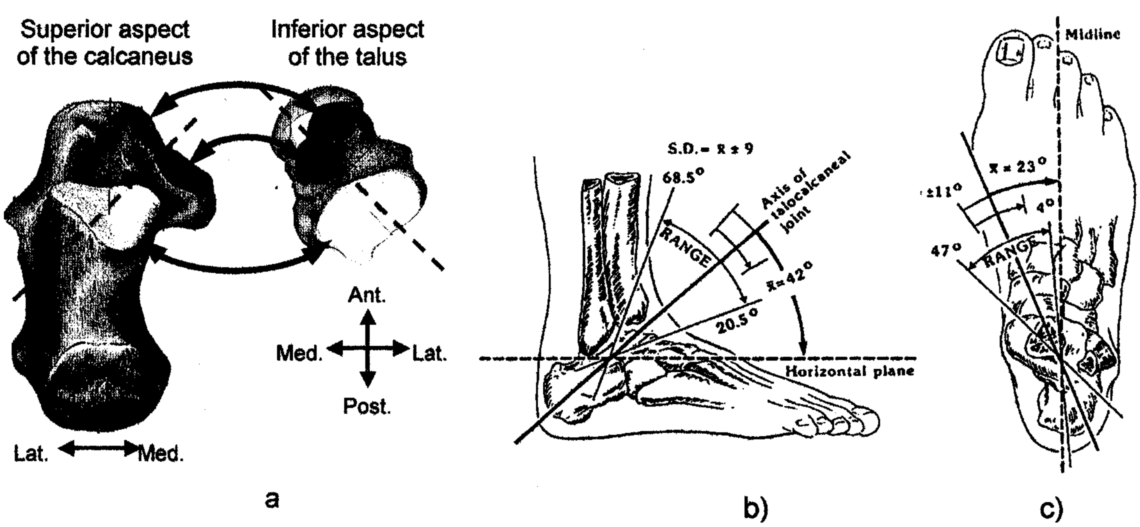

Figure 2-12: Subtalar joint: a) mating articular surfaces on the calcaneus and talus (adapted from www.bartelby.com, © Bartleby.com, reprinted with permission); axis of rotation in b) lateral and c) top view (from Stiehl[192]).

to 23° medially[86,126,195] (Figure 2-12, b and c). The subtalar joint is mainly responsible for pronation and supination of the ankle joint complex. Some investigators[78,167] have observed pure rotation at the subtalar joint, while others[86,87,126,195] have reported a screw-like motion, a combination of rotation about and translation along the axis of rotation.

2.3 Ankle injuries in sports

The ligaments allow for motion of the bone at the joint, but only within certain ranges of motion. Ankle sprains occur when the ankle is turned in any direction further than the ligaments are able to tolerate. This results in a partial tearing or complete tearing of the ligament. This ligament damage results in the development of abnormal motion at the joint due to the loss of stability.

The term sprain merely indicates that a ligament has been damaged. Sprains are divided into several groups depending on the severity of damage to the involved ligament. A grade I injury is designated for patients who exhibit localized tenderness but no instability. The ligaments connecting the ankle bones are often over-stretched and damaged microscopically, but not actually torn. The ankle still maintains the normal range of motion with little or no impairment of function. A grade II injury is more severe and indicates that the ligament has been more significantly damaged, but without significant instability. This is caused by partial tearing of ligament fibres. A grade III injury, which is the most severe case (Figure 2-13a), indicates that the ligament has been significantly damaged, and that instability has resulted. A grade III injury means that the ligament has been torn. More than 50% of all ankle injuries are grade I injuries and do not require invasive surgery or massive rehabilitation procedures.

The ankle sprain, the lateral ankle sprain in particular, is the most common sports-related injury[69]—occurring mostly in sports involving running or jumping. This ankle

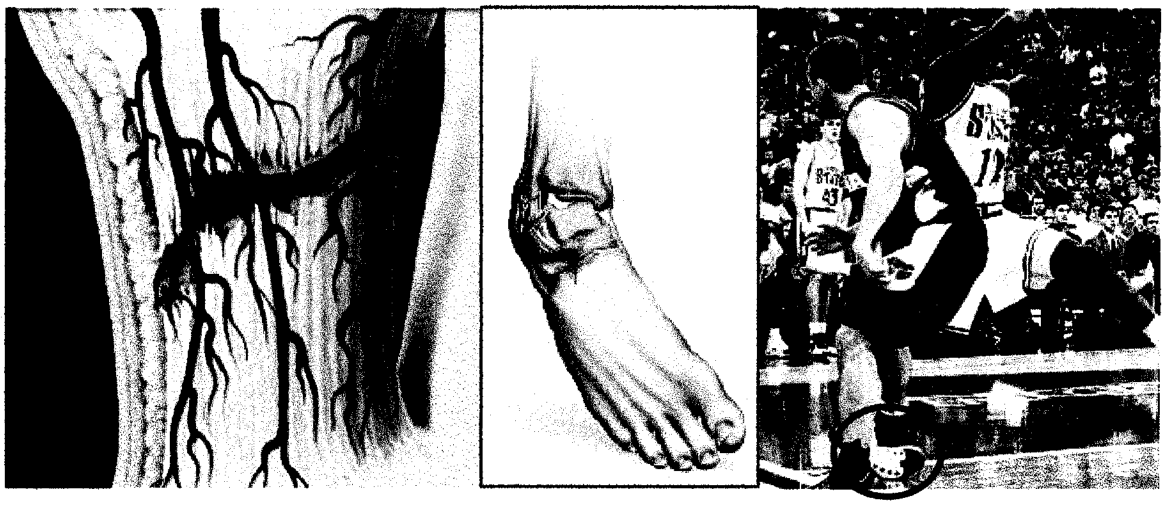

a) b) c)

Figure 2-13: Ankle sprains: a) grade III ligament sprain resulting from complete disruption of ligament fibres (from www.medicalmultimediagroup.com, © Medical Multimedia Group 1997, reprinted with permission); b) inversion sprain of the ankle, anterior view (from www.acfas.com, © The American College of Foot and Ankle Surgeons, reprinted with permission); c) basketball player injuring his ankle (from www.usatoday.com).

sprain results from an inversion injury in 90% of all cases (Figure 2-13b). This can result from an athlete landing on his or her inverted foot, landing on a team-mate's or opponent's foot (Figure 2-13c), or landing on an obstacle. The major damage to the ligaments occurs during the follow-through motion of the body due to its inertia, increasing the degree of inversion and the moment exerted on the inverted joint. The inversion tears the anterior talofibular and calcaneofibular ligaments. At the moment of the ankle spraining, an athlete's ability to activate his or her shin muscles is critical to providing resistance to counter this inversion.

Occasionally, when the ligaments heal, they are weaker or looser than prior to the injury. This results in an ankle that is more likely to be unstable and twist more easily. Sometimes, it is necessary to wear a brace to support the ankle (Figure 2-14a) when walking on uneven ground or during sports. On rare occasions, it is necessary to surgically reconstruct the ligaments (Figure 2-14b).

2.4 Ankle injuries in snowboarding

The number of sport-related injuries that require medical assistance is nearly equal to twice the number of injuries caused by motor vehicle accidents[82]. A recent study[75], done at the Hospital for Sick Children in Toronto (Ontario, Canada), shows that hospital costs for snow-sport (including ski, snowboard and toboggan) injuries were over 27000$ per patient, outpatient services (rehabilitation hospitals, home care nursing and physiotherapy) over 15000$ per patient and financial impact to the family (including lost parental wages) over 1500$ per patient.

The following sections present a review of epidemiological studies on snowboard injuries, propose aetiological explanations and suggest corrective measures. Epidemiology refers to the prevalence of a health problem and the characterization of

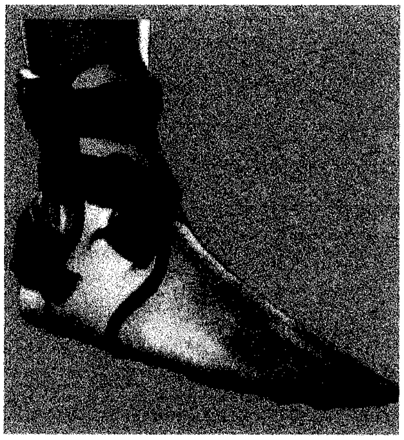

a)

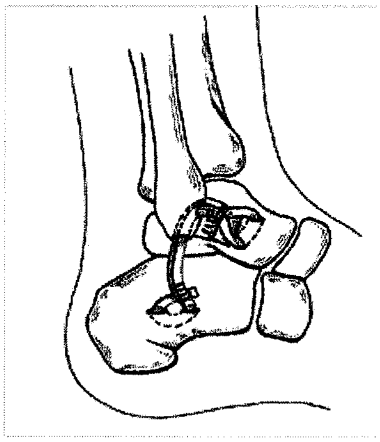

b)

Figure 2-14: a) MalleoLoc ankle brace by Bauerfeind (from www.orthobionics.com); b) ankle ligament reconstruction (from www.orthobluejournal.com).

the affected population. Aetiology is the study of the causes of health problems.

2.4.1 Epidemiology

Injury patterns in snowboarding resemble the kind of injury patterns that occurred in alpine skiing 30 years ago. Before the 1970s, ankle injuries were common in alpine skiing. The last 30 years, however, have seen a shift in the injury pattern in alpine skiing, from ankle sprains and tibial fractures to knee injuries (anterior collateral ligament strain or tear), mainly due to the change in design of the ski boots, which became higher and more rigid.

The incidence of trauma from snowboarding is 2 to 6 for every 1000 medical examinations, which is slightly higher than that in alpine skiing, as reported in epidemiological studies comparing the two populations[17,19,68,176,177,178,179]. In the largest published epidemiological study[176], involving 19019 reported injuries over an 8-year period, the injury rate in snowboarders was 36% higher than in alpine skiers, which represents a statistically significant difference.

Shealy *et al.*[177] have reported the injury rate distribution by comparing it to a control group and taking into account the gender and skill level. They observed a higher injury rate (per 1000 skier-days) for women (4.1) than for men (2.8), which, once distributed according to skill level, become equal. This difference comes from the fact that beginner snowboarders have a higher injury rate (men: 11.2; women: 11.7) than intermediate (men: 2.2; women: 2.0) or advanced (men: 0.78; women: 0.62) snowboarders and that a higher proportion of beginners is found in the women group than in the men group in this sport.

Unlike alpine skiers, snowboarders have both feet attached to the same board with non-release bindings and most of them wear very flexible boots. Therefore, it is not surprising that injuries are distributed differently on the body in snowboarding and in alpine skiing (Table 2-1). Among the largest differences, snowboarders are 4.9 times more prone to injure their wrist and 2.4 times more prone to injure their ankle, while skiers have 15.9 times more chance to injure their thumb and 2.6 times more knee injuries.

Apart from differences with alpine skiers, snowboarders are injured differently, depending on their type of equipment or their stance on the snowboard. Snowboarders with soft boots have a higher incidence of ankle injuries than snowboarders with hard boots[19,68,97,151,152,179]. Some authors[16,18,19,45,89,97,150,152] have also observed a higher proportion of injuries to the lower extremity (leg, knee, ankle and foot) located forward on the snowboard (62.5% to 91%). Others[3,151,178,179] report more injuries to the left leg (54.4% to 75.4%) than the right leg, also mentioning that the majority of snowboarders

Table 2-1: Percentage of injuries to each body part in snowboarding and alpine skiing (pooled results of 14 epidemiological studies).

	snowboarding	alpine skiing
pooled number of injuries	6178	37779
time period covered	1986-1997	1988-1997
references	3,19,28,40,45,68,97,107, 151,152,168,178,190,192	19,40,45,76,107, 168,178,190,192
head/face/neck	11.4	14.7
shoulder	8.2	10.1
upper arm	2.5	1.5
elbow	2.7	0.0
lower arm	6.4	1.8
wrist	18.2	3.7
hand	3.4	0.3
thumb	0.7	11.1
finger	1.0	0.0
trunk/back/pelvis/hip	8.4	3.8
knee	14.0	36.2
lower leg	4.0	8.6
ankle	15.8	6.6
foot	1.5	0.1
other	1.6	1.4

(52% to 62.8%) use the position called "regular", i.e. with the left leg forward, rather than "goofy", i.e. with the right leg forward.

2.4.2 Aetiology

Few authors have looked at the cause of injuries[20,40,45,68,76]. Much of the time (23%[20] to 32%[45]), injuries in snowboarding involve no particular activity other than riding in a straight line, standing still or stopping ("regular snowboarding"). Turns are involved in 21%[45] to 55%[20] of injuries. According to other investigators, 10%[76], 14%[45], 16%[20] and even 41%[40] of injuries in snowboarding occur while jumping or performing an aerial manoeuvre. Collisions are responsible for few injuries (4%[20] to 9%[40]).

The most frequent mechanism of snowboard injuries is falling (impact with snow), accounting for an average of 62.7%, while torsion and flexion are involved in about 32.7% of injuries[16,17,68,97,152,177,179]. Shealy[179] reports that falls are more frequent in snowboarding than in alpine skiing.

Epidemiological studies have shown that the forward leg is more often injured than the other leg. Pino and Colville[152] explained this phenomenon by the unequal distribution of the weight of the snowboarder, who, in order to make a turn, puts more weight on the front leg, thus increasing the mechanical stresses in this leg. Davidson and Laliotis[45] add that the front foot is often placed at an angle between 30 and 45 degrees relative to the transverse axis of the board instead of being parallel to this axis like the rear foot. During a fall, the extremity of the board rammed into the snow acts like a lever, exercising different moments to the two legs, which may be more harmful to the front leg.

Several investigators[19,89,97,150,152,168] describe the mechanism of ankle injury to be a combination of hyper-dorsiflexion and inversion of the foot. This mechanism would also be responsible for the fracture of the lateral process of the talus, a fracture more frequent in snowboarding than in any other sport and called the "snowboarder's ankle"[150]. Indeed, when the foot is inverted, the subtalar joint loses its congruence and the pressure is concentrated on the lateral process of the talus. Other authors also mention hyper plantar flexion, inversion and eversion when the snowboarder falls backwards[152], as well as eversion and the combination of eversion and dorsiflexion for the fracture of the lateral process of the talus[150].

Some studies have tried to correlate injuries to the lower extremities with the type of boots used (soft or hard). Some investigators inferred that the injury pattern observed during the evolution of alpine ski boots could repeat itself in snowboarding. Pino and Colville[152] reported an injury rate in snowboarders wearing soft boots that was twice that in those wearing hard boots. Some have observed that a higher proportion of snowboarders with ankle injuries wore soft boots, while a higher proportion of snowboarders with knee injuries wore hard boots[19,68,97,179]. Others, although not having specifically documented the types of boot in their injured population, have attributed the higher proportion of ankle injuries in snowboarding than in skiing to the skiers' use of hard boots[40,45,107]. Pigozzi *et al.*[151] conclude that snowboarders wearing hard boots are less prone to injuries to the lower limbs than those wearing soft boots.

Finally, based on their epidemiological data, Kirkpatrick *et al.*[97] have reached the following conclusions:

- Soft boots expose the ankle to a higher risk of sprain but protect it against fractures of the lateral process of the talus.
- Hard boots expose the ankle to a higher risk of fractures of the lateral process of the talus.

2.5 Snowboard equipment technological advances

2.5.1 Epidemiologists' recommendations

Some authors noticed that non-release bindings found on most snowboards reduce the frequency of certain types of injuries such as lacerations[3,190] and knee injuries[19,146,151,168,190], especially to the medial ligament[3]. Nevertheless, several others suggested that release bindings could reduce the number of ankle injuries[3,16,18,45,68,178]. In that case, given the weight of the snowboard, when one foot is released, a mechanism should automatically release the other foot to avoid creating large moments on a leg still attached to the snowboard[19,89,178,190]. Moreover, the snowboard should include a braking system instead of a strap attached to one of the legs to avoid the snowboarder from being hit by his or her own snowboard during a fall[19,178]. However, using release bindings would limit freestyle activities, in which extreme movements are common and a sudden release of the bindings could be dangerous[19]. Shealy *et al.*[176] suggested, as a compromise, a binding that can "relax" without releasing.

Some studies showed that snowboarders wearing hard boots or boots with an ankle support have fewer ankle injuries[152,190]. Soft boots seem to protect less the ankle[40,45,68,150] but produce lower stresses on the legs, thus reducing the chance of contusions or fractures[3]. Some authors thus recommended the use of more rigid boots[68,178], although they mentioned that these rigid boots could interfere with turning techniques[178] or increase the frequency of knee injuries while decreasing the frequency of ankle injuries[3,45,68,151]. The use of boots containing a rigid insert[45,68] or which could limit the motion of the ankle to a safe range[178,179], at least for the front leg[151,152], would be the best solution according to other investigators. These "hybrid" boots would be especially recommended for beginners[18,19,45], because they are more comfortable than hard boots and an injury, if it should happen, would have more chances of being an ankle sprain, which is less severe than an injury to a knee ligament[19]. Finally, others suggested that different protection solutions should be used for men and women[26,177], the latter having about 2.5 times more knee injuries than men, while men have twice as many ankle injuries as women[177].

2.5.2 Unreleased patented products

Although since 1988 several releasable binding designs have been patented in Canada[55,172] and the USA[15,24,54,64,71,79,94,162], there has been no consensus on their use and, to our knowledge, none of them has been released in the market. A review of the scientific literature reveals no documentation of the movements leading to ankle injuries in snowboarding. Thus, it appears that these design modifications to bindings and boots are intuitive and the determination of their efficiency is based on speculation. This is especially disconcerting for releasable bindings, which should release when external forces or moments that can cause injuries are applied. While the direction and magnitude of those forces remain unknown, it seems that inventors' opinions are the main justification for releasable binding mechanism designs.

There is a trend for more rigid, "hybrid", boots and rigid inserts for soft boots to become increasingly popular. Without knowledge of the injury mechanisms, hybrid boots may sacrifice range of movement in directions that are harmless to the snowboarder and, thus, unnecessarily compromise his or her performance in this sport.

2.6 Mechanical properties of the ankle

Ankle sprains result from mechanical "failure" of ligaments. Therefore, the mechanical properties of the ankle joint and of its ligaments are related to ankle sprains. The range of motion of the ankle joint provides values for maximum rotation of the ankle in every direction. If ankle injury were displacement dependent, as Dorius and Hull suggested[56], rotation past those values would cause injuries. Stability of the ankle is due to the action of its ligaments. Some ligaments rotate without elongating throughout the range of motion of the ankle. For instance, the CFL remains almost isometric throughout the flexion of the ankle joint[186]. Such ligaments guide the ankle motion in a preferred passive path and prevent dislocation of the joint. Other ligaments, such as the PTFL, are slack most of the time and start to stretch near the extremes of the range of motion of the ankle[186]. These ligaments limit the range of motion of the ankle. The range of motion and stiffness of the ankle is thus a function of the mechanical properties of the ligaments.

2.6.1 Range of motion

In vitro as well as *in vivo* studies on the ankle range of motion have been reported in the literature (Table 2-2). Early experiments were mostly done using sagittal radiographs, goniometers or potentiometers, while recent studies used more precise three-dimensional stereoscopic techniques, either sonic, video or optoelectronic.

The ranges of motion were measured passively or actively. When measured passively, the foot was rotated relative to the shank in different directions until a certain external force was required to maintain the rotation (*in vitro* and *in vivo*) or a subject-assessed pain threshold was reached (*in vivo*). Parenteau et al.[149] reported the *in vitro* rotation at failure, as determined by audible indication of tissue damage, joint popping or fracture. In active measurements (*in vivo* only), the subject was asked to rotate his or her foot in different directions until he/she reached the maximum rotation, for which muscle forces cannot overcome the stiffness of the ankle.

Table 2-2: Range of motion of the ankle (mean ± standard deviation).

First author	Sammarco		Roaas	Milgrom	Weiss	Siegler	Nigg	Grimston	Allinger		Siegler	Aström	Parenteau	pooled average
Year	1973		1982	1985	1986	1988	1992	1993	1993		1994	1995	1998	
Ref.	169		165	133	196	181	143	74	7		182	9	149	
Type of study	*In vivo*		*In vivo*	*In vivo*	*In vivo*	*In vitro*	*In vivo*	*In vivo*	*In vivo*		*In vivo*	*In vivo*	*In vitro*	
Measurement technique								Stereoscopic						
	Radiographic		Goniometric	Goniometric	Potentiometric	sonic	video	video	video		optoelec-tronic	Goniometric	Potentiometric	
(A)ctive/(P)assive	P		P	P	P	P	A	A	A		P	P	P	
Axial loading (N)	body weight	0	0	0	0	0	100	100	100		0	0	0	
Age (yr)	20-65		30-40	18-20	22-32	70±13	20-39	17-20	27±3	64±8	19-40	20-50	52-89	
No of subjects	16	5	96	272	6	15	30	31	7	10	18	121	8	
Dorsiflexion (°)	21±7	23±8	15±6		9±4	25±3	26±7	27±1	21	22	13±5		44±11	20.2
Plantar flexion (°)	23±8	23±10	40±8		48±1	41±4	45±9	45±1	35	28	31±4		72±6	39.6
Inversion (°)			28±7	32±7		16±4	21±7	27±1	19	15	20±5	28±6	34±8	28.6
Eversion (°)			28±5	4±4		16±5	15±5	12±1	11	10	22±4	10±4	33±7	11.2
Internal rot. (°)						22±6	38±8	45±1	11	5	15±3			29.3
External rot. (°)						30±8	35±10	31±14	12	16	24±4			28.0

Axial loading on the limb simulates body weight but neglects the additional compressive forces on the joint due to muscle co-contraction. Full body weight can be used to study a movement during which the subject stands on one limb at the time, like walking, whereas half the body weight can be used for movements during which the subject has his/her weight equally applied on both limbs, like diving. Unloaded conditions refer to the situation for which the testing is done with no axial force on the limb. Most authors have observed the largest range of motion in plantar flexion and the smallest ranges of rotation of the ankle in dorsiflexion and eversion.

2.6.2 Mechanical properties of the ligaments

Tendons and ligaments possess time- and history-dependent viscoelastic properties, assumed to be related to complex interactions of their constituents, namely collagen, water, proteins and ground substance[202]. Stiffness and failure load increase with strain rate whereas failure elongation and failure strain remains unchanged at traumatic strain rates (up to 150000 mm/min) versus quasi-static loading, in human Achilles tendon[113], human cervical spine ligaments[207] and rabbit knee ligaments[44]—an adequate animal model to investigate the failure of human ligaments during trauma[11]. Similarly to other collagenous tissues, ankle ligaments exhibit strain-rate dependent[10], nonlinear[10,180] stiffness. Although the failure properties of ankle ligaments were characterized at different strain rates by different investigators (Table 2-3), the effect of strain rate on failure load and elongation has not yet been reported. Despite a large discrepancy in published results, the ATFL was unanimously shown to be the weakest of all ankle ligaments, possibly explaining why it is also the one that is most often injured.

2.6.3 Relation between ankle rotations and ligament strains

The *in vitro* strain in selected ankle ligaments throughout the range of motion of the ankle were reported in three studies (Table 2-4). Cadaver ankle specimens were placed in combinations of flexion (dorsi-/plantar), version (in-/e-) and rotation (internal/external). For each combination, the ligaments strain was measured. All studies reported that the maximum strain in the ATFL occurred at the combination of maximum plantar flexion, adduction and inversion, while maximum strain in the CFL occurred at maximum dorsiflexion and inversion.

These sets of data provide statistical models to interpolate and predict ligament strain from ankle rotation. How these strains relate to ultimate values reported in Section 2.6.2 depends on the way they are reported. Nigg et al.[144] and Colville et al.[41] chose to report

Table 2-3: Failure properties of the lateral ankle ligaments (mean ± standard deviation).

First author		St. Pierre	Attarian	Siegler	Nigg	Funk	pooled average
Year		1983	1985	1988	1990	2000	
Ref.		185	10	180	144	67	
Donor Age (yr)		64±14	58	68±15	47±23	50±7	63
Height (cm)			165	171±9			168
Weight (kg)			68	69±15			69
Displacement rate (mm/min)		125	800-1000	3.2	1000	280	260
No of specimens	ATFL	36	12	20	3	2	73
	CFL		16	20	3	2	41
	PTFL		4	20		2	26
Width (mm)	ATFL	8.3±2.2	7.6±0.4				8.1
	CFL		6.8±0.4				6.8
	PTFL		7.8±0.4				7.8
Length (mm)	ATFL	13.6±4.8	10.5±0.6	17.8±3.1			12.8
	CFL		17.5±0.7	27.7±3.3			17.5
	PTFL		15.3±0.9	21.2±3.9			15.3
Cross-sectional area (mm^2)	ATFL			12.9±7.7			12.9
	CFL			9.7±6.5			9.7
	PTFL			21.9±18.1			21.9
Ultimate load (N)	ATFL	207±128	139±24	231±129	130±63	297±80	202
	CFL		346±55	307±142	296±31	598±53	336
	PTFL		261±32	418±191		554±95	404
Ultimate elongation (mm)	ATFL		5.1±0.5	2.5±0.8			3.5
	CFL		6.3±0.5	3.7±0.7			4.9
	PTFL		13.1±1.6	3.5±0.9			5.1
Ultimate Stress (MPa)	ATFL			24.2±16.9			24.2
	CFL			46.2±36.6			46.2
	PTFL			26.0±24.8			26.0
Ultimate Strain (mm/mm)	ATFL		0.53±0.06	0.15±0.06			0.29
	CFL		0.38±0.03	0.13±0.03			0.24
	PTFL		1.00±0.15	0.17±0.05			0.31

Table 2-4: Comparison of three studies reporting the *in vitro* strains in ankle ligaments throughout the range of motion of the ankle.

Author	Renström	Nigg	Colville
Year	1988	1990	1990
Ref.	164	144	41
Measurement technique	Hall effect transducers	pins, dividers and ruler	strain gauges
No of specimen	5	3	10
Age (yr)	42-67	34-73	28-79
Ligaments	ATF, CF	ATF, CF, DL	ATF, PTF, CF, DL
Range of dorsiflexion/ plantar flexion	10(D)-40(P)	15(D)-30(P)	20(D)-30(P)
Range of inversion/eversion	20(I)-15(E)	15(I)-15(E)	imposed torque ±3Nm
Range of abduction/adduction	10(Ab)-10(Ad)	13(Ab)-13(Ad)	imposed torque ±3Nm
Result format	% strain relative to length in neutral position	% strain relative to minimum length, normalized with maximum length	% strain relative to minimum length

the strain relative to the minimum length value measured throughout the range of motion for each ligament. Renström et al.[164] preferred reporting the strain relative to the length of the ligament when the ankle is in neutral position (zero rotations). It is debatable whether these "zero strain" definitions correspond to the zero strain conditions used in tensile tests.

2.7 *Kinematics and kinetic measurements in skiing and snowboarding*

On-field kinematics measurements in alpine skiing have been done in 2-D using electro-goniometers or rotary potentiometers[101,115,129,131,136,137,138,157,159] and gyroscopes[101]. Three-dimensional measurements using videographic techniques[139,170] were used to measure the whole-body kinematics, with low precision on specific joints rotations and a small measurement volume, because the position, orientation and zoom of the cameras were fixed during the data acquisition.

Electromagnetic motion tracking systems have also been used to measure 3-D kinematics of the leg in alpine skiing[73]. This technique has the advantage of allowing a measurement field virtually unlimited because it travels with the skier, but the disadvantage of referring all measurements to a coordinate system carried on the skier, which is not at a constant orientation with respect to the direction of gravity. Moreover, this technique does not account for foot motion inside the ski boot, because ankle rotation was measured as the relative motion between a sensor located on the skin over the tibia, and a sensor attached to the boot. Electromagnetic sensors are too big to fit inside a shoe or boot. Woodburn *et al.*[203] successfully by-passed this problem by cutting out a rear window in a shoe and attaching the sensor on the skin over the posterior part of the calcaneus (Figure 2-15). Electromagnetic systems are precise enough to track several foot bones (calcaneus, navicular and first metatarsal) with skin-mounted sensors in a laboratory barefoot walking experiment[43]. Static metal parts in the measurement volume create distortions in the electromagnetic field and measurement errors[46,134,145], which can be compensated for by one of several metal-mapping techniques proposed in the literature[23,47,84,95,96,99,114,132,208].

On-field kinemtic measurements of normal forces acting on ski boots have been done using strain gauges located under the boots[131,138] and pressure transducers placed inside the boots[102,103,104,105,171]. The three components of the forces and moments transmitted to the boots by the skis have been measured using six-degree-of-freedom (DOF) strain gauge dynamometers, located under the toe and heel bindings[65,83,101,115,136,142,157,158,159,193,198], and using one 6-DOF strain gauge dynamometer per ski as part of an experimental electronically releasable binding located under the middle of the boot[121,122,129,160,205,206].

Similar measurement techniques have been adapted to snowboarding. Plate bindings of alpine SB were adapted to fit on a 6-DOF strain-gauge-based dynamometer[14]. In that experiment, Bally and Taverney observed no significant correlation between measured loads and snowboarder's weight. They concluded that setting tables for snowboard release bindings, analogous to those used for alpine ski bindings, could not be produced. Other researchers[98] have simply equipped freestyle and alpine SB with two

Figure 2-15: Electromagnetic sensor attached to calcaneus posterior skin surface in modified shoe (from Woodburn *et al.*[203], by permission of the British Society for Rheumatology).

custom-made 6-DOF force plates located between each binding and the board. Knünz *et al.*[98] observed larger forces on the forward boot than on the other boot. They found that no force was applied on the forward boot during heel turns. Larger forces were also measured with carved turns (alpine snowboarding), especially toe turns, than with skidded turns (freestyle snowboarding). On-field snowboarding kinematic measurements have not been reported in the scientific literature.

2.8 Biomechanical modelling of the ankle joint

Estes *et al.*[63] published the only computer model of the ankle joint applied to snowboarding. They have modeled the ankle in 2-D as torsion springs, based on passive stiffness data from Chen *et al.*[35] to study ankle deflection during computer simulated forward falls in snowboarding.

Few 3-D geometrical or mathematical models of the ankle have been developed so far. Some authors have attempted to model the 3-D kinematics of the ankle using the instantaneous axes of rotation of the talocrural and subtalar joints throughout their physiological range of motion[80,183,194], using 4-by-4 transformation matrices between the tibia, the talus and the calcaneus[58], using a four-bar linkage between the tibia and the calcaneus[108], or using kinematic measurements on cadaver specimens as a statistical model to predict talus orientation from tibia and calcaneus orientations[62]. Other kinematic models have represented the ankle joint complex as a 2-DOF system, modelling the talocrural and subtalar joints as fixed-axis revolute joints, to predict ligament strains[6] and orientations[109], and to calculate the position of the axes of rotation[194].

Mechanical models have been used to study the effect of surgical changes in musculoskeletal geometry and the ways by which musculotendon parameters affect muscle force[50]. Finite element models of the foot and ankle were defined from 3-D reconstructions of magnetic resonance[209] or CT images[36,111] of a foot, with articular surfaces modelled as contact surfaces and ligaments modelled as tension-only truss elements[209], springs and dashpots[111] or linear elastic homogenous 4-node tetrahedral solids[36].

Several issues are raised by this literature survey. Injuries on the ski hills are anatomically distributed differently according to the type of sport, snowboarders getting fewer knee injuries and more ankle injuries, especially to the anterior talofibular ligament (ATF), than alpine skiers. Whether this is due to the differences in equipment or in specific motions associated with each sport is so far purely speculative. Whereas over 40 studies report on the epidemiology of snowboard injuries, only three have investigated the biomechanics of snowboarding.

The use of a 2-D computerized model of a snowboarder to study the mechanism of ankle injuries was reported in one article. Since the ankle joint complex is often approximated as two revolute joints having their rotation axes oriented differently in 3-D, conclusions of such a 2-D analysis of ankle biomechanics must be regarded cautiously.

Aiming at determining the threshold force for automatic release bindings, measurements of forces acting on the boots during typical snowboard manoeuvres were reported in two conference abstracts. As the failure load of ankle ligaments was observed to be strain-rate dependent, one might wonder about the possible efficiency of a binding with a release criterion based on force alone.

Despite the fact that failure strain does not seem to be affected by strain rate, no investigator has reported on the measurements of the kinematics of a snowboarder's lower limbs. This is probably due to the technical difficulties of performing precise 3-D kinematic measurements on outdoor winter sports, as demonstrated by the small number of studies on alpine skiing 3-D kinematics. Among those studies, the one using electromagnetic motion tracking technology shows attractive advantages over videographic techniques.

Finally, different types of mechanical models have been used to study the biomechanics of the ankle joint complex. Mechanical models offer the advantage of being able to predict positions, deformations or forces that are difficult to measure *in vivo*, using non-invasive kinematic or kinetic measurements as input. The use of a deformable or non-deformable bodies approach, with a finite element or a kinematic model respectively, depends on the nature of the measured input values and expected output predictions.

3 Instrumentation and Experimental Procedures

3.1 General comments

The objective of this research was to study the effect of the type of snowboard equipment on ankle kinematics under snowboard loading. This requires measurements to determine how close the ligaments are to injury limits during normal snowboarding manoeuvres.

Ankle kinematics can be used to extract physiological variables, such as the rotation of the ankle joint complex, or mechanical variables, such as ligament elongation or strain. Ligament strain, rather than load or stress in the ligament, was selected as the dependent mechanical variable to be examined in this study because ligament failure strain does not seem to depend on strain rate (as discussed in Section 2.6.2). In order to avoid invasive measurements of ligament strain on human participants, an indirect kinematic approach was chosen.

The experiments consisted of measuring the 3-D relative motions of the shanks and feet of nine participants executing regular snowboard manoeuvres, using two different types of snowboard equipment. After unsuccessful trials with a stereovideographic technique (see Appendix B), electromagnetic motion tracking was selected as the most suitable technique to measure snowboard kinematics on the ski hill.

This approach, summarized in Figure 3-1, is indirect because only the position and orientation of body segments are measured. Neglecting the motion between the bones and the skin markers used to track the segments, the combination of 3-D kinematic measurements of the shanks and feet with an anatomical calibration, to define the position and orientation of the bone with respect to its attached sensor, allows tracking the position and orientation of the calcaneus and tibia in 3-D space. Then, considering that ligaments connect two bones together from fixed insertion points, assumptions and models can be used to predict ligament strains from bone positions and orientations:

1) A **statistical model** was built on average relationships between ankle rotation

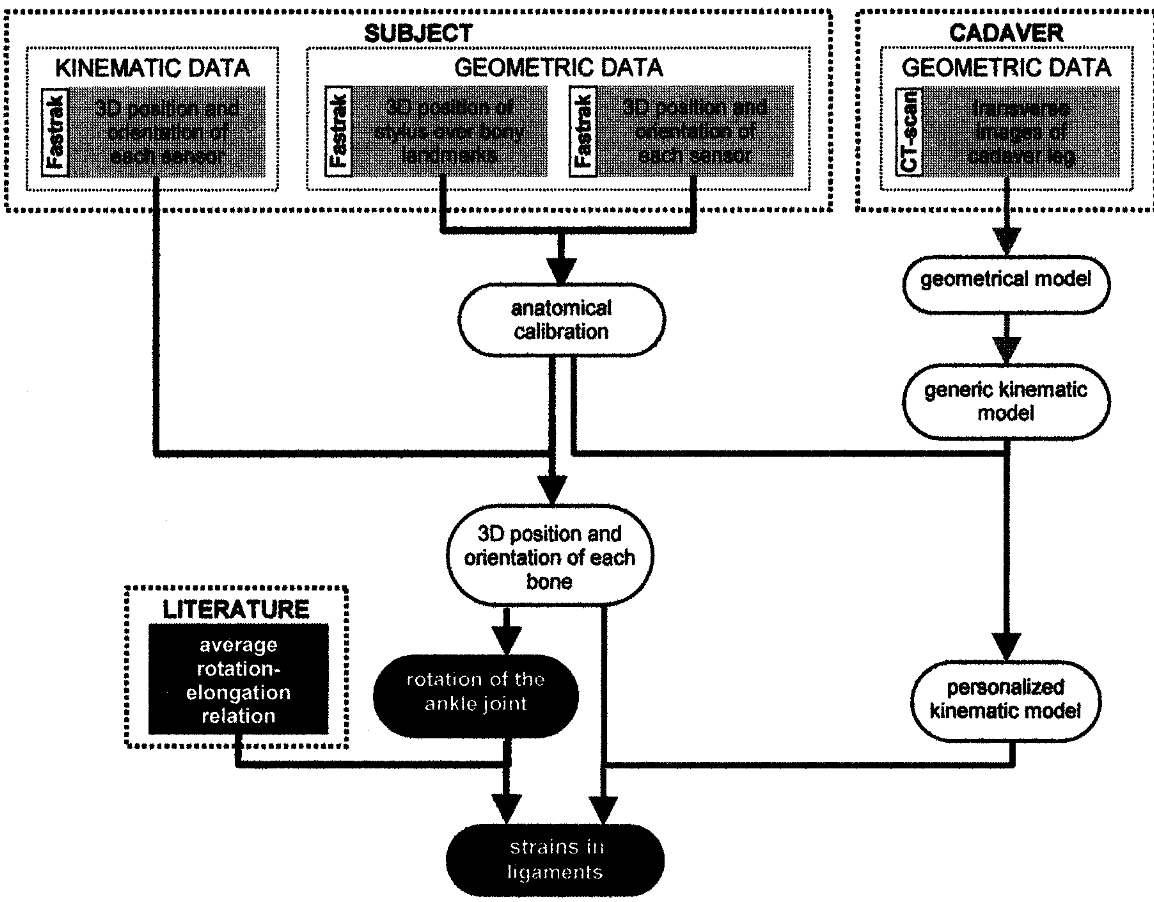

Figure 3-1: Overview of the measurements and calculations required for the project. Light grey boxes represent measurements (the tag on the side of the box indicates the type of apparatus used), dark grey boxes contain published data taken from the scientific literature, white bubbles are intermediate calculation results and black bubbles are final results to be compared with limit values from the literature. Black arrows indicate flow of data with the statistical model approach and grey arrows indicate flow of data with the kinematic model approach.

and ligament strain from published cadaver studies. Ankle rotations were calculated from relative bone orientations. The statistical model predicts the strains in ankle ligaments from ankle rotations.

2) A **kinematic model**, obtained from medical images of a cadaver leg specimen, was personalized to each participant's morphology using the anatomical calibration data. The model predicts the position and orientation of the talus, which is the missing link in the kinematic chain between the tibia and the calcaneus. The model assumes no relative motion between the tibia and the fibula. Thus, from specified positions of ligament insertion points on each bone, the model can predict the strain in ligaments joining any two bones among the tibia-fibula, talus and calcaneus.

Ligament strains obtained with either approach can then be compared with published ligament failure strains. Moreover, because the statistical model necessarily involves calculating ankle rotation, these rotations can be compared with published physiological ranges of motion for the ankle joint complex.

All assumptions and models will be detailed and discussed in chapter 5. The present chapter will describe the apparatus and procedure used in the experimental part of this project, and present the calculations required to express the experimental data in terms of ankle rotations.

3.2 Participants

Nine male volunteer snowboarders aged 20 to 34 participated in the study. The inclusion criteria were 1) willingness to participate; 2) availability at the specified dates and times; 3) expertise on a freeride or freestyle snowboard (soft boots) at an intermediate level or better as evaluated by the participant; 4) shoe size male 9;

5) agreement to sign the informed consent form (see Appendix C). The only exclusion criterion was the occurrence of any past or present musculoskeletal injury to the lower limbs that could have an effect on normal movement in snowboarding.

3.3 Equipment used

3.3.1 Snowboards

Each participant was asked to perform a total of six trials, which consisted of two sets of three repeat trials on the following types of snowboard equipment (Figure 3-2):

1) A freestyle snowboard (Limited, Ascent 159) with strap bindings (Salomon, S2) and

a) b)

Figure 3-2: Two types of snowboard equipment used: a) strap bindings (from www.salomonsnowboards.com, © Salomon, reproduced with permission) and soft boots; b) step-in bindings and step-in boots.

soft boots (Vans, Millennium).

2) A freeride snowboard (Limited, Apex 163) with step-in bindings (Switch, Special N-Type) and step-in boots (Vans, Mach).

These two typical types of equipment were chosen to be representative of popular commercial products.

Snowboard bindings were adjusted according to each snowboarder's preferred riding stance. In the vocabulary adopted by snowboarders, riders with the left foot forward are called "regular" and those with the right foot forward are called "goofy". Out of the nine volunteers, six were regular and three were goofy, a distribution that is representative of the snowboarder population. Whatever the stance, both feet were set to point in the forward direction, the binding of the forward foot being adjusted at 21 degrees and the other binding at 6 degrees (Figure 3-3). These angles are measured with respect to the transverse horizontal axis of the snowboard and are positive in the forward direction.

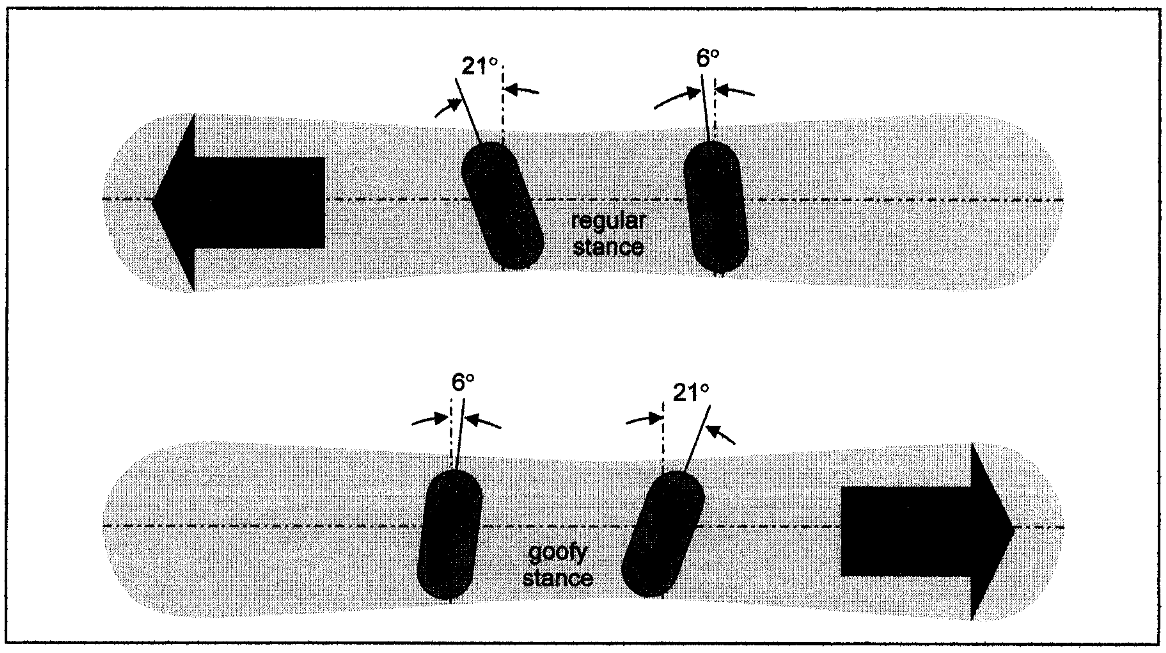

Figure 3-3: Binding settings according to riding stance.

Each binding has an indexed mechanism with 3 degrees steps, which allows for a good repetition of those settings.

3.3.2 Measuring instruments and set-up

Appendix D presents detailed specifications of each piece of equipment used in the experiment. This section presents how they work together. During the trials, each participant wore a backpack (Figure 3-4) containing the Fastrak system electronics unit (see Section D.1), a battery pack (two 12V batteries with a DC-to-DC converter) and a laptop computer (see Section D.2). The backpack and its content weighed

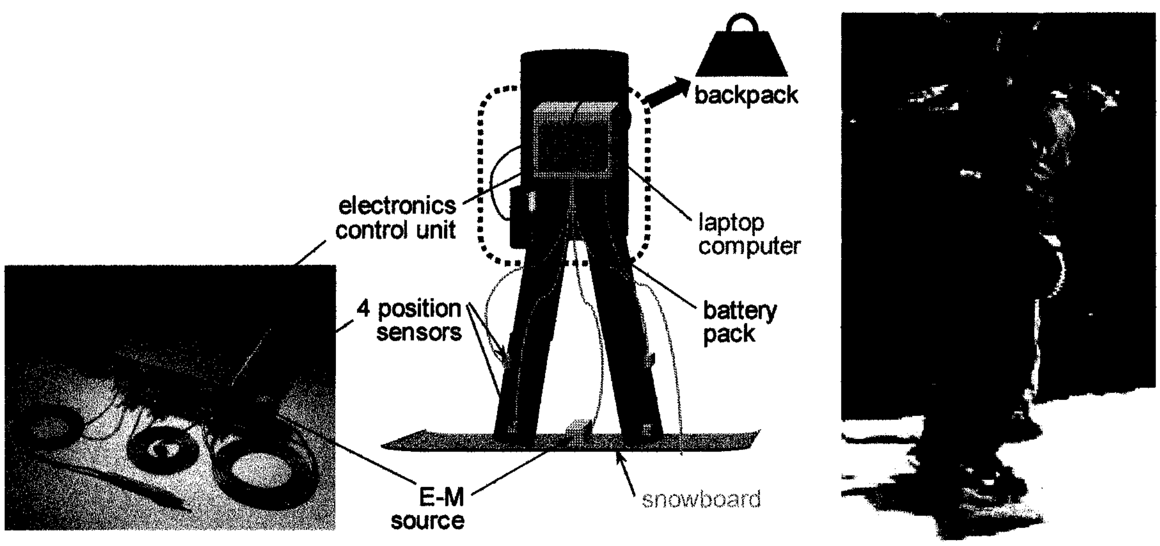

Figure 3-4: Measuring equipment worn by each participant. The Fastrak system (left, adapted from Fastrak User's Manual[154], © Polhemus Inc, reproduced with permission) is a motion tracking system with an electromagnetic source, and four 6DOF position and orientation sensors. The Fastrak system, the battery pack and the laptop computer are located in a backpack. The electromagnetic source and sensors are connected to the Fastrak system. Picture of one participant at the beginning of a trial (right).

approximately 11 kg. The trials were also filmed with a JVC digital camera (see Section D.3).

A custom-made electronics box containing a 555 signal generator and a switch were used to trigger the Fastrak system and turn on a LED (light emitting diode) also located on the box. The LED location was recorded by the digital camera, allowing synchronizing the video signal and the data recorded by the Fastrak system. This provided a qualitative visual interpretation for the Fastrak measurements.

The battery pack powered both the laptop computer and the Fastrak electronic unit, which transmitted its data to the laptop computer via the serial port. Pre-testing of the effect of voltage decrease on measurements with two types of battery pack (see Section E.1) led to the selection of low charge 12-Volt batteries (Power Sonic 1229, 2.9 A-hr).

The Fastrak electromagnetic source was attached to the top surface of the snowboard, at mid-distance between the two bindings. The source was first mounted with non-ferromagnetic 316 stainless steel screws on a polycarbonate part glued with double-sided tape to the top surface of the snowboard (Figure 3-5). Because of difficulties in making the polycarbonate adhere to the snowboard surface, especially at outdoor winter

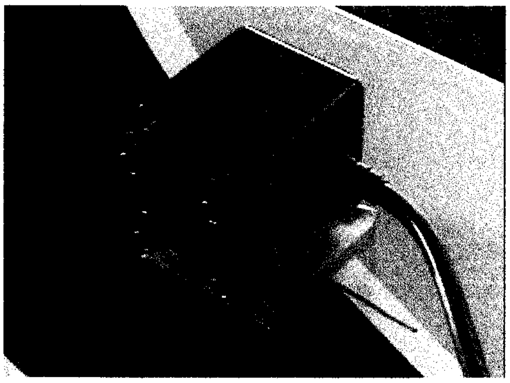

Figure 3-5: Photograph of the source mounted on the snowboard with a polycarbonate part.

temperatures, this mounting system was replaced by bolting the source directly on the snowboard through four tapered holes. The wires of the source were connected to the Fastrak electronic unit and hung loosely without touching the ground or restricting the snowboarder's movements.

Four Fastrak sensors were attached to the participant's feet and shanks, one on each foot and one on each shank. To minimise sensor motion caused by skin movement, the sensors were located at sites associated with minimal underlying soft tissue, according to the procedure used by Woodburn *et al.*[203] (Figure 2-15). Moreover, each sensor was fastened to a piece of 3 mm thick thermoformable plastic, using high-strength double-sided tape. The piece of plastic was cut and shaped to fit each participant and glued to his/her skin using liquid medical adhesive.

The sensor on the foot was located over the skin covering the posterior part of the calcaneus, inferior to the attachment of the tendo calcaneus Achilli (Figure 3-6). A "heel

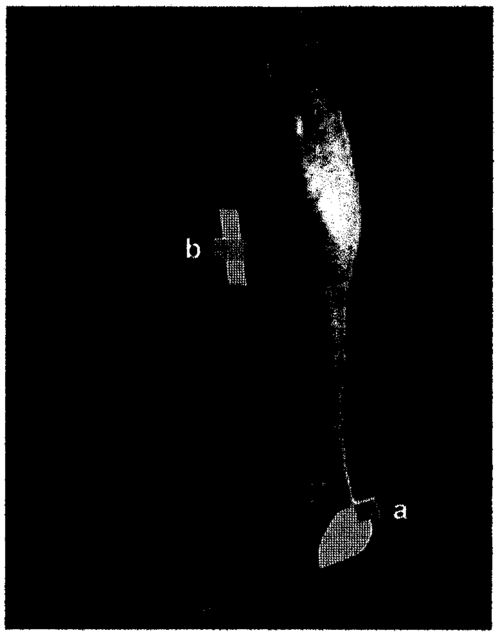

Figure 3-6: Location of the foot (a) and shank (b) sensors (adapted from thriveonline.oxygen.com).

cup" made of a 10 cm × 10 cm square piece of thermoformable plastic was moulded to the participant's heel and glued to his skin. A 4 cm diameter hole was drilled in the boots to allow the sensor to stick out of the boot and follow the foot while the foot moves relative to the boot. Because of its location behind the heel, this hole will only minimally alter the stiffness of the boot, and will do so equally on each type of boots. The sensor on the shank was located over the skin covering the tibia on the anterior part of the shank between the boot top and the knee (Figure 3-6). A 3 cm × 8 cm piece of thermoformable plastic was moulded and glued to the skin covering the tibia. The wires of the sensors were loosely fitted in the participant's pants along the leg and connected to the electronic unit in the backpack.

3.4 Measurements

All measurements were done at the Bromont ski resort in Quebec between January and April 2002. One participant was measured per experiment day. The participant was fitted with the snowboarding and measuring equipment as described above in a heated building at the mountain base. Before the first trial, at the top of the hill, an anatomical calibration was performed on the participant. Then, the kinematics of the lower legs were measured while the participant performed three trials. After the three trials were completed, the anatomical calibration was repeated to check whether the sensors had moved relative to the skin during the trials. Then, the participant was sent back to the base, changed snowboard equipment and returned to the top of the hill. One anatomical calibration, three trials with kinematic measurements, and a final anatomical calibration were performed. All these events are detailed below.

3.4.1 Anatomical landmarks

Anatomical calibration is the process that defines the position and orientation of the bone with respect to the sensor attached to the corresponding bone. It consists of measuring the position of surface landmarks on the skin that correspond to anatomical landmarks on the bone. Those surface landmarks are found by palpation. The anatomical landmarks are chosen based on their accessibility, precision of location and suitability for a proper definition of a coordinate system. During those measurements, the sensor is attached to the measured segment (shank or foot).

The anatomical landmarks and coordinate system definition proposed by Cappozzo *et al.*[33] were chosen for this study (Table 3-1,Figure 3-7). The Standardization and Terminology Committee of the International Society of Biomechanics[204] recently issued a new standard for defining the coordinate systems on the shank and foot, based on anatomical landmarks different from those used here. Unfortunately, these guidelines had not yet been published at the time of the experiment.

There is very little relative motion between the tibia and the fibula[4,91,109,184]. Therefore, the anatomical landmarks taken on those two bones will define a coordinate system that will be assumed to be rigidly attached to the tibia at any knee or ankle rotation. However, this is not the case for the foot, because motion occurs at the calcaneocuboid, intertarsal and tarsometatarsal joints, among others. Thus, the anatomical landmarks on the foot would define different coordinate systems when the foot is in a neutral, dorsiflexed or plantar flexed position. To ensure repeatability and anatomical significance, the anatomical calibration must be performed with the foot in the neutral position.

Table 3-1: Names and symbols of the anatomical landmarks used for the anatomical calibration.

Segment	Landmark	Symbol
Shank	Prominence of the tibial tuberosity	TT
Shank	Apex of the head of the fibula	HF
Shank	Distal apex of the medial malleolus	MM
Shank	Distal apex of the lateral malleolus	LM
Foot	Upper ridge of the calcaneus posterior surface	CA
Foot	Medial aspect of first metatarsal head	FM
Foot	Dorsal aspect of second metatarsal head	SM
Foot	Lateral aspect of fifth metatarsal head	VM

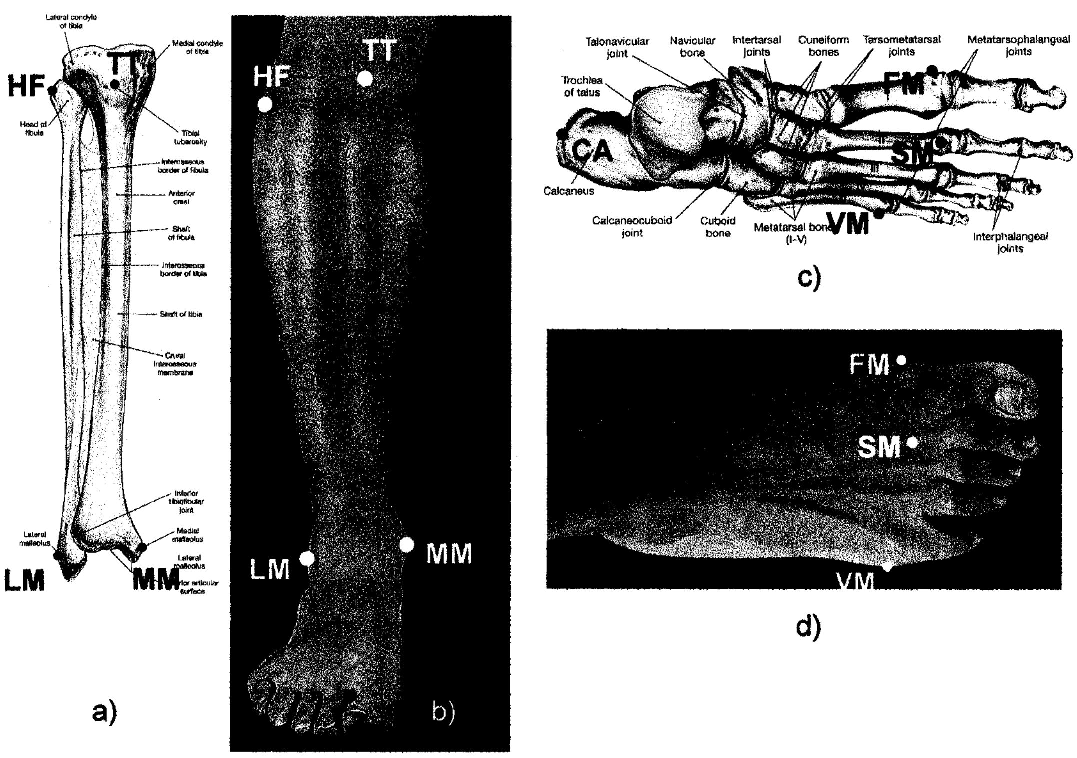

Figure 3-7: Anatomical landmarks on the shank and foot (adapted from Martini *et al.*[123], reprinted by permission of Pearson Education, Inc.). Anterior view of the right shank bones (a) and skin surface (b). Dorsal view of the foot bones (c) and foot surface (d).

10 mm diameter holes were drilled in the boots over the approximate location of the landmarks covered by the boots (Figure 3-8). The landmarks were measured through those holes with a custom-designed plastic stylus attached to one extra Fastrak sensor (see Appendix F for details on stylus design and tip calibration algorithm). One landmark (SM, see Table 3-1) was not measured because of the difficulty of drilling a hole in the boot over it without affecting the structure of the boot. Instead, its position was deduced from published average morphometric data on metatarsal distances[70] and the positions of FM and VM.

At the beginning of the experiment, before the participant put on the snowboard boots, the anatomical landmarks located inside the boots were palpated and marked on the skin with the leg in neutral position and outside the boots. At the top of the ski hill, the anatomical landmarks were measured through the holes in the boot, while the

Figure 3-8: Location of the holes drilled in the snowboard boot, shown here on a boots similar to those used in the present project (adapted from www.rakuten.co.jp). One-centimetre diameter holes for anatomical landmark measurements are shown in yellow. The four-centimetre diameter hole to let the foot sensor stick out is shown in red.

snowboarder was wearing the boots and standing in the bindings. With the strap bindings, the highbacks were removed during this procedure to allow access to the CA landmark through the hole for the foot sensor.

3.4.2 Trials

One trial consisted of snowboarding down a 100-metre course of 10 turns (5 toe turns, 5 heel turns) on a beginner-level slope (6 to 10 degrees) of groomed snow. At the end of the course, the participant performed a sideways stop.

3.4.3 Kinematic data

Kinematic measurements were done with the Fastrak system. The motions of the shank and foot bones relative to the snowboard were measured by the four position sensors attached to the participant's shanks and feet during the trials, at the maximum frequency allowed by the system, i.e. 30 Hz. A DOS-based proprietary computer program from Polhemus was used to interface the Fastrak system with the laptop computer via the serial port. Data acquisition was started and stopped using the switch box attached on the participant's shoulder. The entire trial, starting with turning on the LED on the switch box, was filmed from the top of the course. The Fastrak data were saved on the laptop computer at the bottom of the course in an ASCII file, each line containing the following values: sensor number, error code (if any), x, y and z components of position data, expressed in centimetres (two-digit precision), as well as azimuth, elevation and roll components of Euler angles (Figure 3-9), expressed in degrees (two-digit precision).

Because of the symmetry in the magnetic fields generated by the Fastrak source, the hemisphere in which the sensors are located must be specified. Preliminary testing using the top hemisphere for all four sensors (Figure 3-10a) has shown that sometimes the foot sensors went below the equator of that hemisphere, thus causing mirror values.

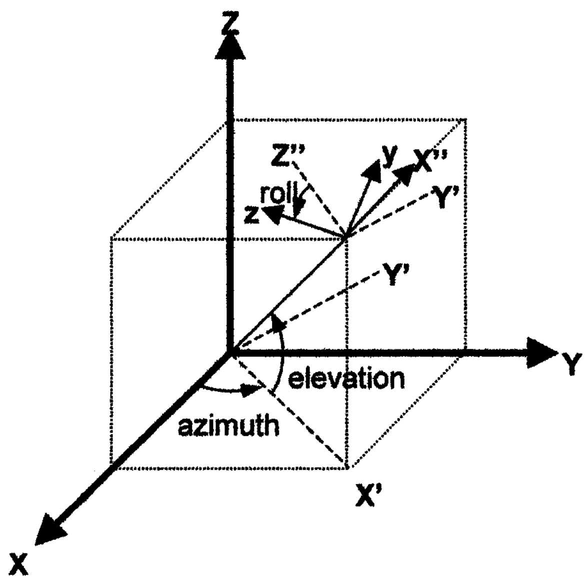

Figure 3-9: Euler angles output by the Fastrak system. Azimuth is the rotation around the Z axis. Elevation is the rotation around the Y' axis. Roll is the rotation around the X" axis.

Therefore, the left hemisphere was used for the sensors on the left leg and the right hemisphere was used for the sensors on the right leg (Figure 3-10b).

3.5 Post-processing

In order to have a biomechanical meaning, the raw data collected with the Fastrak system were transformed in several steps using a custom-made program in Matlab. Correction for static metallic noise and digital filtering were applied to minimise the noise content of the recorded signals. Anatomical calibration data were then used to transform sensor position and orientation into bone position and orientation. Finally, the three orthogonal components of the rotation of the ankle joint were calculated from the bone relative orientations.

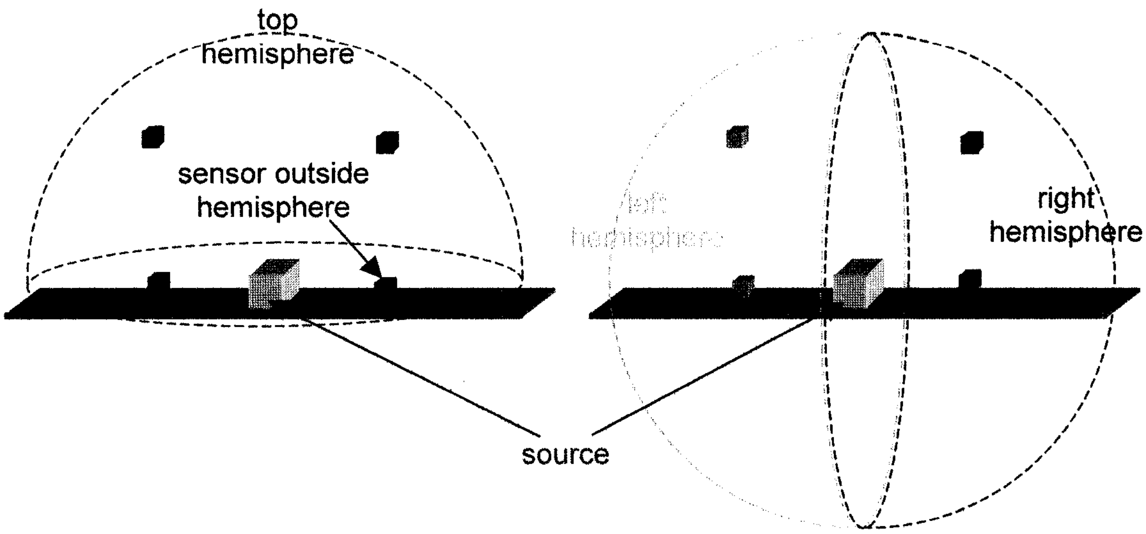

a) b)

Figure 3-10: Hemisphere settings for measurements with the Fastrak.

3.5.1 Correction for static metallic noise

Electromagnetic motion tracking systems like Fastrak are sensitive to the presence of magnetic fields or large metallic objects near the source or the sensors, which can distort the magnetic field emitted by the source and produce false readings of the sensors[46,134,145]. The magnitude of the measurement errors is related to the magnetic permeability, the conductivity, the mass of the object, and the distance between the object and the source or the sensor. If the objects that distort the field do not move with respect to the source, the metallic noise is static and can be compensated for by a process often referred to as metal mapping.

Metal mapping consists of measuring a fixed 3-D grid of points inside the volume of measurements, with and without the presence of metal. A mathematical relationship is then established to map the points measured on the grid with the metal to the points measured on the same grid without the metal. The relationship can be used afterwards to compensate for the distortion by applying it to any measurement taken inside the grid volume. Metal mapping with various mathematical formulations has been successfully used with electromagnetic tracking systems[23,27,47,84,95,96,99,114,132,134,145,208].

Preliminary tests conducted with the two snowboards available for the present study showed that the measurement errors due to the presence of metal in the snowboard, bindings and boots are negligible for the freestyle snowboard with the strap bindings but not for the freeride snowboard with step-in bindings (see Section E.2). This is mainly because the strap bindings are mostly made of plastic, except for some metallic nuts and bolts, while the step-in bindings contain a very large aluminium part and many steel parts in their mechanism. Therefore, a metal mapping algorithm was used to compensate for static metallic noise in the measurements collected with the step-in bindings only.

A jig specially constructed to measure points with the Fastrak on a 3-D grid was used to collect the metal mapping data. The mathematical formulation of the mapping algorithm chosen for this study involves the use of geometrical kriging, a technique that has been used in biomechanical studies by Delorme *et al.*[49,50] to calculate a field of deformation vectors. The details of the algorithm, the design of the jig and sample results are presented in Appendix F. Contrary to all the other mathematical formulations cited above, geometrical kriging does not require its control points to be located on a regular 3-D lattice. Therefore, kriging offers the advantage of allowing local refinement of the measurements to better capture a small perturbation, or to skip some points if they were not accessible for measurements with the sensors. In the present application, the measurement volume extends across the step-in bindings. Therefore, measurements could not be taken at points located inside the binding material or too close to the binding to position the sensor centre at this point. This added flexibility of the geometrical kriging technique justified its selection over the mathematical techniques proposed by other investigators.

3.5.2 Filtering

Digital filtering of the signals to eliminate noise was done using the technique described by Winter[199] (pp. 36-43). As recommended by Winter for human kinematic data, a dual-pass, second-order Butterworth filter was applied to the data. The second pass is done backwards so as to cancel out the 90-degree phase lag introduced by the first pass. This results in a 4^{th}-order Butterworth filter with zero lag. The cut-off frequency was calculated by a residual analysis using data from one randomly selected trial. The cut-off frequency obtained on all signals (position and orientation) for all four sensors was 2.3 Hz (Figure 3-11).

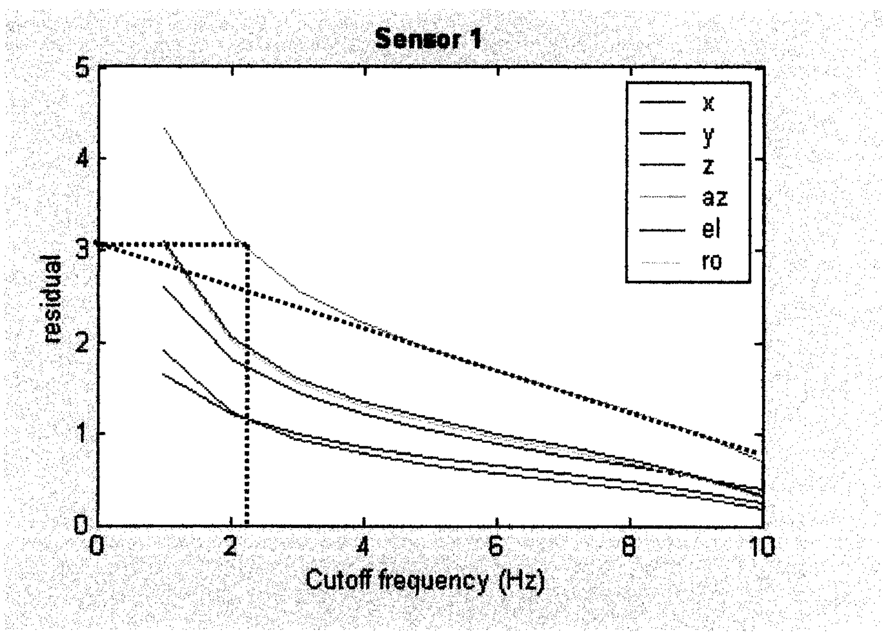

Figure 3-11: Selection of the cut-off frequency for digital filtering with a dual-pass second-order Butterworth filter.

3.5.3 Anatomical calibration

During the anatomical calibration, points that define a bone-embedded coordinate system (BECS) were measured, while the position of the corresponding bone was tracked with its attached sensor, itself defining a technical coordinate system (TCS).

Any point defined in the bone-embedded coordinate system (BECS), $\vec{P}_{BECS}$, can be expressed in the global coordinate system (GCS) as:

$$\vec{P}_{GCS} = {}_{GCS}[M]^{TCS} \times {}_{TCS}[M]^{BECS} \times \vec{P}_{BECS} \qquad [3\text{-}1]$$

where ${}_{GCS}[M]^{TCS}$ is a matrix that expresses in the GCS a point defined in the TCS. This matrix varies through time as the sensors, and thus the TCS, move during the measurements. It is easily constructed directly from the data output by the Fastrak system. With x, y, z as the three position components, and θ_z (azimuth), θ_y (elevation), and θ_x (roll) as the three Euler angles (Figure 3-9) of the sensor, one gets

$${}_{GCS}[M]^{TCS} = \begin{bmatrix} \ddots & & \cdot^{\cdot^{\cdot}} & x \\ & R & & y \\ \cdot^{\cdot^{\cdot}} & & \ddots & z \\ 0 & 0 & 0 & 1 \end{bmatrix} \qquad [3\text{-}2]$$

where

$$R = \begin{bmatrix} \cos(\theta_z) & -\sin(\theta_z) & 0 \\ \sin(\theta_z) & \cos(\theta_z) & 0 \\ 0 & 0 & 1 \end{bmatrix} \begin{bmatrix} \cos(\theta_y) & 0 & \sin(\theta_y) \\ 0 & 1 & 0 \\ -\sin(\theta_y) & 0 & \cos(\theta_y) \end{bmatrix} \begin{bmatrix} 1 & 0 & 0 \\ 0 & \cos(\theta_x) & -\sin(\theta_x) \\ 0 & \sin(\theta_x) & \cos(\theta_x) \end{bmatrix} \qquad [3\text{-}3]$$

and ${}_{TCS}[M]^{BECS}$ is a matrix that expresses in the TCS a point defined in the BECS. The latter matrix is constant through time because the sensor (TCS) is assumed to be rigidly linked to the bone (BECS). It is constructed with the vectors that define the BECS:

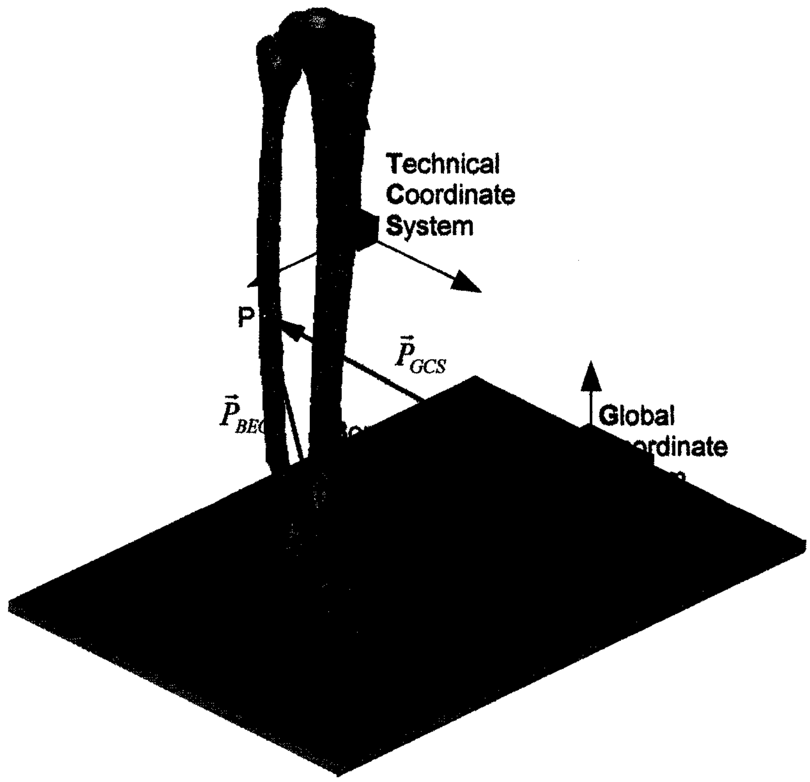

Figure 3-12: Coordinate systems associated with the snowboard (GCS), the sensor (TCS) and the bone (BECS).

$$ {}_{GCS}[M]^{BECS} = \begin{bmatrix} \begin{pmatrix} \vdots \\ X \\ \vdots \end{pmatrix} & \begin{pmatrix} \vdots \\ Y \\ \vdots \end{pmatrix} & \begin{pmatrix} \vdots \\ Z \\ \vdots \end{pmatrix} & \begin{pmatrix} \vdots \\ O \\ \vdots \end{pmatrix} \\ 0 & 0 & 0 & 1 \end{bmatrix} \qquad [3\text{-}4] $$

where X, Y, Z and O are column vectors that express in the GCS the three orthonormal vectors and the origin position vector of the BECS.

The bone embedded coordinate systems (BECS) on each shank and each foot (thin black arrows on Figure 3-13) were defined from the anatomical landmarks measured during the anatomical calibration procedure using the method described by Cappozzo *et al.*[33]

The shank BECS is defined in the following manner (refer to Table 3-1 for abbreviations):

O_s: Midpoint of the line joining MM and LM.

y_s: LM, MM and HF define a quasi-frontal plane. O_s and TT define a quasi-sagittal plane, orthogonal to the quasi-frontal plane. The y_s axis is the intersection between those two planes, with the positive direction proximal.

z_s: Lies in the quasi-frontal plane with its direction from left to right.

x_s: Orthogonal to the y-z plane with its positive direction from left to right.

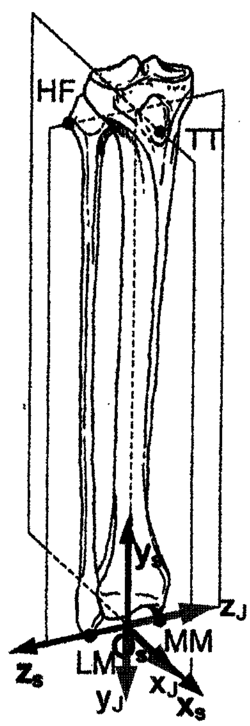

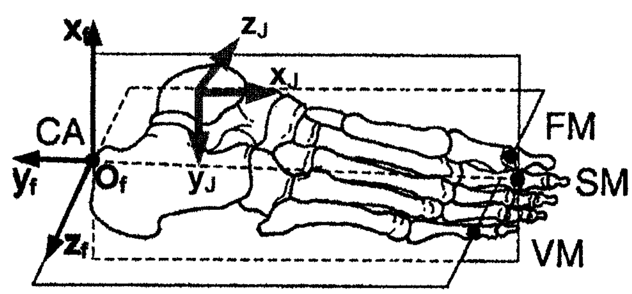

Figure 3-13: Definition of the coordinate systems on the shank and foot. Subscripts "f" designates the foot BECS, "s" the shank BECS, and "J" the JCS. (Adapted from Cappozzo *et al.*[33], © John Wiley & Sons Limited 1997, reproduced with permission.)

The foot BECS is defined as:

O_f: CA.

y_f: CA, FM and VM define a quasi-transverse plane. CA and SM define a quasi-sagittal plane, orthogonal to the quasi-transverse plane. The y_f axis is the intersection between those two planes, with the positive direction proximal.

z_f: Lies in the quasi-transverse plane with its direction from left to right

x_f: Orthogonal to the y-z plane with its positive direction dorsal.

3.5.4 Ankle rotations

Ankle rotations are derived from the relative orientation of the shank and the foot. First, a joint coordinate system (JCS) is defined for each ankle. One JCS is defined on the shank and another is defined on the foot. These JCS are defined with their axes parallel to those of the BECS in such a way that, when the ankle is in neutral position, the two JCS are superimposed (thick grey arrows on Figure 3-13)*. The JCS can be expressed by the following matrix products:

$$_{GCS}[M]^{JCS_{shank}} = {}_{GCS}[M]^{TCS_{shank}} \times {}_{TCS_{shank}}[M]^{BECS_{shank}} \times {}_{BECS_{shank}}[M]^{JCS_{shank}} \quad [3\text{-}5]$$

$$_{GCS}[M]^{JCS_{foot}} = {}_{GCS}[M]^{TCS_{foot}} \times {}_{TCS_{foot}}[M]^{BECS_{foot}} \times {}_{BECS_{foot}}[M]^{JCS_{foot}} \quad [3\text{-}6]$$

In those two expressions, only the first matrix of the product varies through time, while the last two are constant. Then,

---

* For the left ankle, the x and y axes of the JCS are set in the opposite direction as for the right ankle so that positive rotations have the same anatomical meaning (e.g. inversion, eversion, internal rotation, external rotation) for both ankles.

$$ {}_{JCS_{shank}}[M]^{JCS_{foot}} = \left[{}_{GCS}[M]^{JCS_{shank}}\right]^{-1} \times {}_{GCS}[M]^{JCS_{foot}} \tag{3-7} $$

Similarly to [3-2], the matrix ${}_{JCS_{shank}}[M]^{JCS_{foot}}$ is a 4 $\times$ 4 matrix that contains a 3-by-3 rotation matrix in its upper left corner. Developing this 3-by-3 rotation matrix R from [3-3] yields

$$ R = \begin{bmatrix} c_z c_y & c_z s_y s_x - s_z c_x & c_z s_y c_x + s_z s_x \\ s_z c_y & s_z s_y s_x + c_z c_x & s_z s_y c_x - c_z s_x \\ -s_y & c_y s_x & c_y c_x \end{bmatrix} = \begin{bmatrix} R_{11} & R_{12} & R_{13} \\ R_{21} & R_{22} & R_{23} \\ R_{31} & R_{32} & R_{33} \end{bmatrix} \tag{3-8} $$

where $c_x = \cos(\theta_x), c_y = \cos(\theta_y), s_x = \sin(\theta_x)$, etc.

The rotation matrix R can then be interpreted so as to extract θ_x, θ_y and θ_z using

$$ \theta_y = -\sin^{-1} R_{31} \tag{3-9} $$

$$ \theta_x = \sin^{-1}\left(\frac{R_{32}}{\cos\theta_y}\right) \tag{3-10} $$

$$ \theta_z = \sin^{-1}\left(\frac{R_{21}}{\cos\theta_y}\right) \tag{3-11} $$

Since the matrix transforms the foot JCS into the shank JCS, a positive θ_z represents dorsiflexion of the foot with respect to the shank, while a negative θ_z represents plantar flexion. Positive θ_y corresponds to internal rotation and negative θ_y to external rotation. Positive θ_x refers to eversion and negative θ_x to inversion.

4 Experimental Results

The experimental results will be presented in a form that is anatomically relevant, i.e. as rotations of the ankle joint complex, using the post-processing procedures described in the previous chapter. First, the characteristic features of individual participants will be presented and the validity of the measurements for each trial will be assessed and discussed. Typical rotation signals obtained during one complete trial will be shown as representative of the entire set. Finally, peak ankle rotation values for each subject will be presented and the corresponding values using the two types of available snowboard equipment will be compared.

4.1 Participant characteristics and evaluation of experimental validity

Several problems were encountered during the experiment, as the Fastrak sensors or source failed intermittently. Occasionally, those failures could not be resolved on site and parts had to be shipped to the manufacturer for replacement or repair. A total of four sensors failed. Two failed early enough to be replaced during the course of the measurements, but the last two failed at the end of the last day of the experiment. A consequence of these failures was an incomplete set of data for some participants.

The equipment manufacturer (Polhemus) recommends operating the Fastrak system at a temperature between 10 and 40°C and a relative humidity between 10% and 95%, without vapour condensation. It was verified outside the laboratory (see Section F.3) that operating the Fastrak in winter conditions down to -10°C did not adversely affect the accuracy of the measurements. Initially, the equipment failures were attributed to the contraction of metallic wires of the system due to low temperature or to condensation on the connectors or the circuits inside the electronic control box due to high relative humidity. It was later discovered with the help of Polhemus technical support that most of the failures were due to the lack of a strain-relief reinforcement on the wire protruding out of the plastic casing enclosing some of the sensors. The sensors that most often failed were the ones attached to the calcaneus and had wires that were often sharply bent at their connection to the sensor.

Participant characteristics, availability of valid measurements and explanations of failures are listed in Table 4-1. For the first two participants, measurements are usable only with one type of equipment. For the third participant, no kinematic measurement with any of the two types of equipment is available. For the fourth participant, the anatomical calibration for the left leg is unusable. Complete anatomical calibration and at least one trial with both types of equipment are available only for the last five participants.

Table 4-1: Characteristics of participants and validity of measurements; L: anatomical calibration of the left leg; R: anatomical calibration of the right leg; T1: first trial; T2: second trial; T3: third trial.

participant characteristics				date of experiment	measurement validity									
					soft boots					step-in boots				
no.	age	level	stance		L	R	T1	T2	T3	L	R	T1	T2	T3
1	21	i	g	2002-01-30	✓	✓		✓	✓					
2	22	i	r	2002-02-08	✓	✓	✓	✓	✓	✓	✓	4	4	4
3	28	i	r	2002-02-15	✓	✓	4	4	4	✓	✓	1,4		
4	25	i	r	2002-02-18	S	✓	✓	✓		✓	✓	✓	✓	✓
5	34	i	g	2002-03-08	✓	✓	✓	✓	✓	✓	✓	✓	✓	✓
6	34	e	r	2002-03-13	✓	✓	✓			✓	✓	✓	✓	✓
7	24	e	r	2002-03-19	✓	✓	✓	✓	✓	✓	✓	✓	✓	✓
8	20	e	g	2002-03-21	✓	✓	✓	✓	✓	✓	✓		✓	✓
9	26	e	r	2002-03-25	✓	✓	✓	✓	✓	✓	✓	✓	✓	✓

i : intermediate level
e : expert level
r: regular stance
g: goofy stance

✓: all data measured successfully
1: sensor #1 defective, data unusable
4: sensor #4 defective, data unusable
S: source defective, data unusable
empty: no measurements taken

4.2 *Experimental results for one typical trial*

Figure 4-1 shows an example of measurements for the forward leg of participant no. 7, wearing the soft boots. This figure shows the variations of three ankle rotations, plotted vs. time and following the convention that positive values correspond to dorsiflexion (DF), internal rotation (IR) and eversion (EV).

The initial part of the plots, lasting for approximately 6 s, corresponds to a period during which the measuring system was active but the snowboarder was getting ready to start and was approaching the first turn. The subsequent part, lasting for approximately 22 s, corresponds to a downhill run, during which 10 turns were made. The first turn occurred at around 8 s from the start of the system, as can be seen by the strong changes in the signals. This turn was toe-side, characterized by dorsiflexion of the ankle joint complex. The final part of the plots, starting at about 28 s from the start, corresponds to a sideways stop.

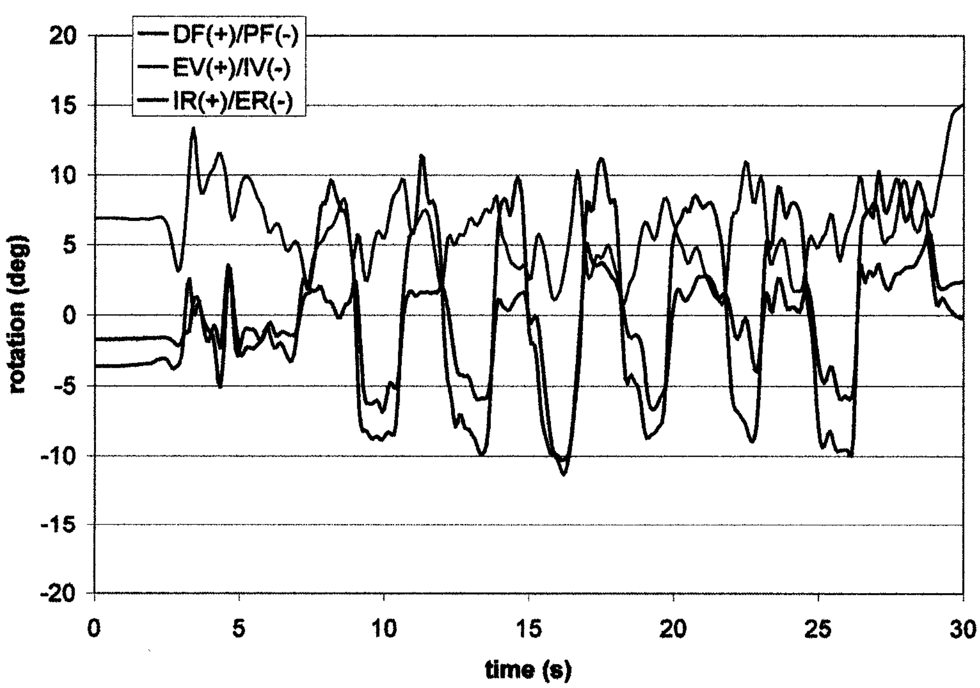

Figure 4-1: Example of forward ankle rotation signals during a complete trial.

4.3 Segmentation and parameterization of signals

For each trial, the parts of the time series which corresponded to turns were segmented into heel-side turns and toe-side turns. The DF/PF signal was selected as the segmentation criterion, as best describing the start and end of each turn; this was verified by comparing the three ankle rotation signals with the video of the snowboarders. Five local minima and five local maxima were identified on the DF/PF signal. A turn started and ended when the DF/PF signal crossed the middle DF/PF value between a local minimum and the subsequent local maximum (Figure 4-2). The signals collected from the back and front legs were segmented separately. The information related to one turn on each leg will be referred to as a "turn-leg".

Some turns were rejected from the data set because of a phenomenon called "gimbal lock". In an azimuth-elevation-roll Euler angle system (Figure 3-9), gimbal lock is an ill-conditioned angle combination that occurs when the second angle (elevation) is close to

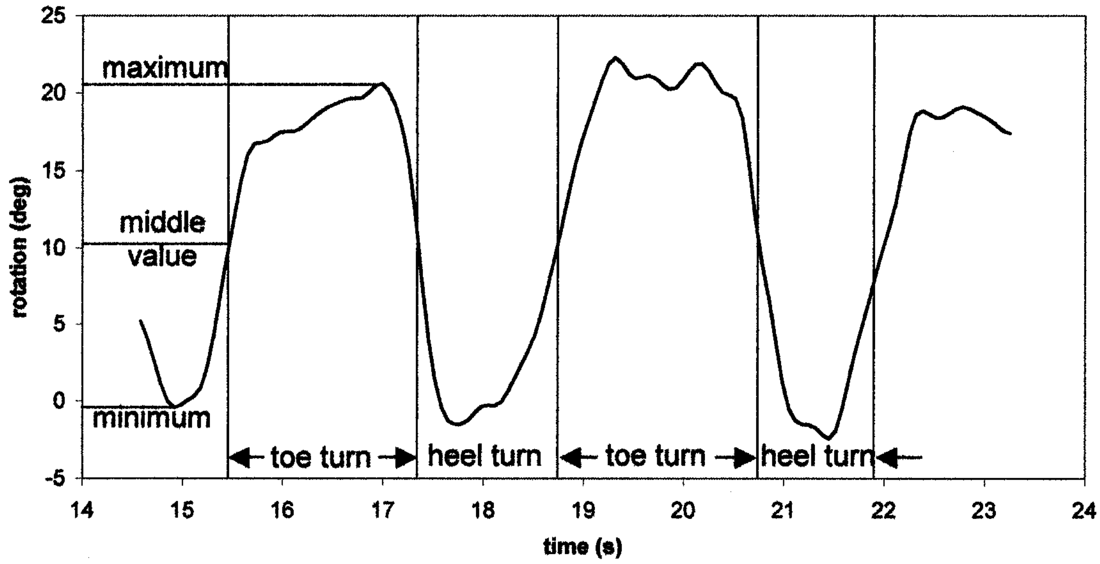

Figure 4-2: Turn segmentation method based on DF/PF signal analysis. The horizontal lines indicate the minimum, maximum and middle values for the first turn. The vertical lines indicate the start and end of each turn.

–90 or 90°. In this situation, the x'' and z axes are aligned, making the roll (rotation about the x'' axis) and the azimuth (rotation about the z axis) cancel each other out, thus yielding an indeterminate azimuth-roll combination. This can be seen by the following arguments. When

$$\begin{aligned} c_y &= \cos(\theta_y) = \cos(90°) = 0 \\ s_y &= \sin(\theta_y) = \sin(90°) = 1 \end{aligned} \qquad [4\text{-}1]$$

the rotation matrix ([3-8]) simplifies to

$$R = \begin{bmatrix} 0 & c_z s_x - s_z c_x & c_z c_x + s_z s_x \\ 0 & s_z s_x + c_z c_x & s_z c_x - c_z s_x \\ -1 & 0 & 0 \end{bmatrix} \qquad [4\text{-}2]$$

$$R = \begin{bmatrix} 0 & -\sin(\theta_z - \theta_x) & \cos(\theta_z - \theta_x) \\ 0 & \cos(\theta_z - \theta_x) & \sin(\theta_z - \theta_x) \\ -1 & 0 & 0 \end{bmatrix}. \qquad [4\text{-}3]$$

This formulation shows that adding a constant to both θ_x and θ_z will produce the same rotation matrix. Therefore, the solution for θ_x and θ_z is indeterminate because an infinite number of combinations can be found for θ_x and θ_z that will produce the same matrix R. A gimbal lock behaviour was observed on the Euler angles output of the Fastrak measurement system, corresponding to anatomically impossible ankle rotations such as 360° of rotation around one of the anatomical axes. Among 466 turn-legs measured, 47 were rejected because of a gimbal lock occurrence. These rejected cases were randomly distributed over the entire experimental data and no evidence of biased rejection was observed.

For each turn, the duration and the right-to-left lag time were calculated. The duration is the time difference between the start and end of the turn-leg. The lag is the difference between the start of the turn on the right leg and the start of the corresponding turn on the left leg. On each signal, the minimum, maximum, range and mean values were calculated for each turn-leg.

A total of 419 turn-legs, distributed as shown in Table 4-2, were analyzed. The data consist of replicate measurements on a small number of participants (5). The inter-individual differences were larger than the intra-individual differences, so the data are clustered rather than normally distributed. Therefore, a non-parametric statistical test, the Mann-Whitney U-test[125], was used to check for significant differences between the two types of equipment instead of a parametric test like the Student t-test, which assumes a normal distribution, a condition expected to be met with a cohort of at least 30 individuals. The U-test is a rank sum test that returns the probability that two samples were taken from different groups.

Table 4-2: Distribution of analyzed turn-legs with the two types of snowboard equipment.

		Equipment A	Equipment B	Total
Heel-side turn	Front leg	48	51	99
	Back leg	47	61	108
Toe-side turn	Front leg	48	52	100
	Back leg	50	62	112
TOTAL		193	226	419

4.4 Average heel-side and toe-side turns

The turn-legs were first split into four groups without taking into account the type of equipment used (one group for each line of Table 4-2). All the parameters described above were averaged over all the turn-legs in each group. Figure 4-3 shows the average heel-side turn and Figure 4-4 shows the average toe-side turn.

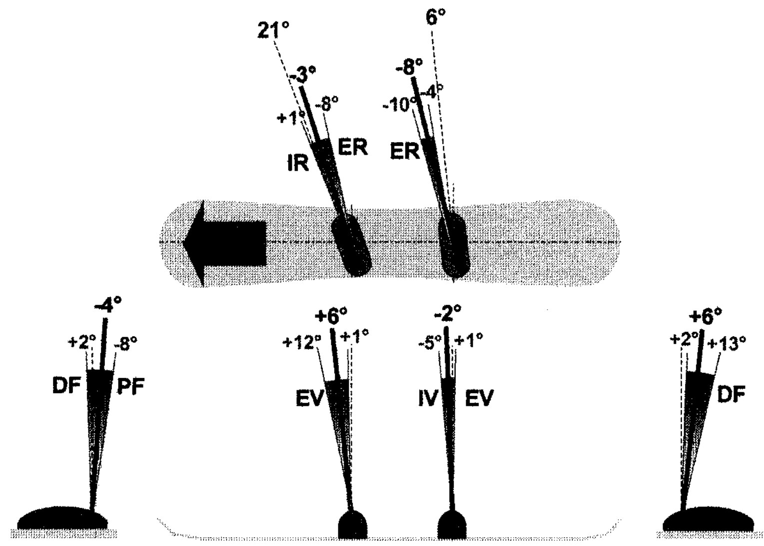

Figure 4-3: Top, back, left and right views of the average ankle rotation parameters during heel-side turns. Number of turns averaged: 99 on front leg, 108 on back leg. The minimum and maximum values are indicated in grey, the mean value in black, and the binding angles in blue.

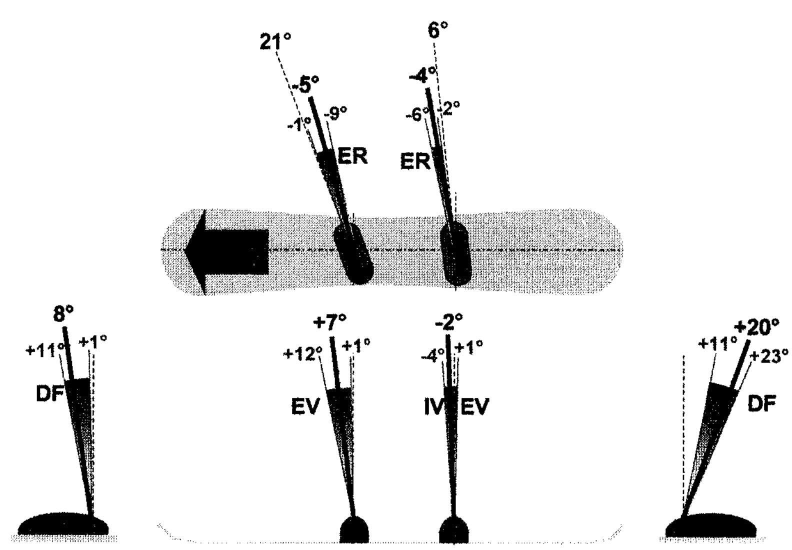

Figure 4-4: Top, back, left and right views of the average ankle rotation parameters during toe-side turns. Number of turns averaged: 100 on front leg, 112 on back leg.

During the heel-side turns, the front ankle was found to be everted, while the back ankle was rotated externally and dorsiflexed. During the toe-side turns, both ankles were dorsiflexed by 12° to 14° more than they were during the heel-side turns. The back ankle was also less externally rotated during the toe-side turns than during the heel-side turns.

Figure 4-5 shows the average timing of heel-side and toe-side turns. The front leg initiated the heel-side turn and was followed by the back leg 0.17 s later. This lag decreased to 0.06 s at the beginning of the toe-side turn. On average, the toe-side turns lasted 23% more than the heel-side turns. An average complete cycle consisting of one heel-side and one toe-side turn lasted 2.98 s.

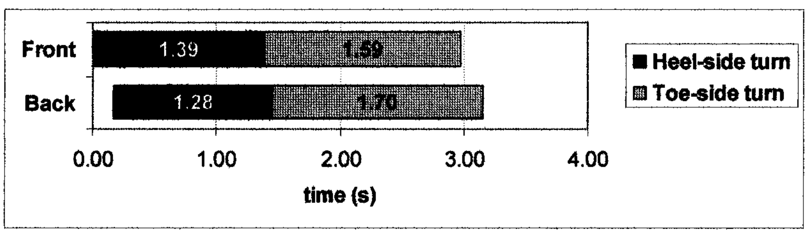

Figure 4-5: Timing of heel-side and toe-side turns.

4.5 Equipment comparison

The four turn-leg groups were further divided into eight groups by separating those obtained with equipment A from those obtained with equipment B (Table 4-2). The comparison of parameters measured on heel-side turns is presented in Table 4-3, and on toe-side turns in Table 4-4. Considering that the number of Mann-Whitney U-tests performed was relatively large (48), the level of significance was set to 0.01*. All

Table 4-3: Comparison of means, minima, maxima and ranges of ankle rotation (in degrees) on heel-side turns with snowboard equipment A and B (average absolute deviation in parentheses).

turn	leg	rot.	index	equipment A		equipment B		*p*-value
				rotation	N turns	rotation	N turns	
heel-side	back	DF/PF	mean	5.4 (7.5)	47	6.0 (8.1)	61	0.237
			min.	0.8 (7.8)	47	2.5 (7.7)	61	0.202
			max.	13.9 (6.3)	47	11.8 (7.8)	61	0.213
			range	**13.1 (2.6)**	47	**9.4 (1.5)**	61	**<0.01**
		EV/IV	mean	-1.1 (11.0)	47	-3.1 (6.2)	61	0.227
			min.	-3.9 (11.4)	47	-6.1 (6.5)	61	0.379
			max.	1.6 (11.1)	47	0.1 (6.3)	61	0.564
			range	5.5 (2.6)	47	6.2 (2.5)	61	0.118
		IR/ER	mean	**-10.9 (4.3)**	47	**-4.9 (1.9)**	61	**<0.01**
			min.	**-13.2 (4.6)**	47	**-7.1 (2.0)**	61	**<0.01**
			max.	**-7.6 (3.8)**	47	**-1.3 (2.5)**	61	**<0.01**
			range	5.6 (1.9)	47	5.9 (1.7)	61	0.252
	front	DF/PF	mean	-3.9 (5.0)	48	-4.9 (3.7)	51	0.329
			min.	-7.8 (5.6)	48	-8.0 (4.1)	51	0.902
			max.	3.6 (5.1)	48	1.0 (3.8)	51	0.041
			range	**11.4 (2.2)**	48	**9.0 (1.7)**	51	**<0.01**
		EV/IV	mean	7.2 (5.3)	48	5.0 (2.1)	51	0.329
			min.	1.1 (7.3)	48	-0.1 (3.6)	51	0.997
			max.	**14.4 (4.8)**	48	**9.6 (2.8)**	51	**<0.01**
			range	**13.3 (6.4)**	48	**9.7 (5.0)**	51	**<0.01**
		IR/ER	mean	-5.1 (7.3)	48	-0.5 (2.3)	51	0.056
			min.	**-10.8 (7.5)**	48	**-4.7 (1.9)**	51	**<0.01**
			max.	-1.0 (7.8)	48	2.5 (3.1)	51	0.365
			range	**9.7 (3.1)**	48	**7.1 (3.0)**	51	**<0.01**

* In a statistical test comparing two means, the *p*-value is the probability that the difference is due to chance. The level of significance is the maximum *p*-value for which the difference is said to be statistically significant. When less than 20 tests are performed, the commonly used level of significance is 0.05, which means that one difference out of 20 may not follow the hypothesis. Since 48 U-tests were performed, the level was set to 0.01.

Table 4-4: Comparison of mean, minimum, maximum and range of ankle rotation (in degrees) on toe-side turns with snowboard equipment A and B (average absolute deviation in parentheses).

turn	leg	rot.	index	equipment A rotation	equipment A N turns	equipment B rotation	equipment B N turns	*p*-value
toe-side	back	DF/PF	mean	21.6 (5.9)	50	18.2 (8.6)	62	0.028
			min.	11.4 (6.7)	50	11.3 (7.7)	62	0.745
			max.	25.4 (5.8)	50	21.2 (8.6)	62	0.017
			range	**14.0 (2.4)**	50	**9.9 (1.3)**	62	**<0.01**
		EV/IV	mean	-0.3 (11.2)	50	-3.2 (6.7)	62	0.138
			min.	-2.3 (11.2)	50	-5.6 (6.4)	62	0.060
			max.	2.3 (11.6)	50	-0.5 (7.0)	62	0.299
			range	4.6 (1.5)	50	5.1 (2.0)	62	0.382
		IR/ER	mean	**-6.9 (3.3)**	50	**-0.7 (2.0)**	62	**<0.01**
			min.	**-9.9 (4.1)**	50	**-3.7 (2.2)**	62	**<0.01**
			max.	**-4.8 (3.2)**	50	**1.0 (2.2)**	62	**<0.01**
			range	5.1 (1.9)	50	4.7 (1.5)	62	0.759
	front	DF/PF	mean	**9.8 (5.0)**	48	**5.5 (4.1)**	52	**<0.01**
			min.	2.1 (4.6)	48	-0.5 (3.7)	52	0.030
			max.	**13.6 (5.3)**	48	**8.6 (4.4)**	52	**<0.01**
			range	**11.5 (2.3)**	48	**9.0 (1.9)**	52	**<0.01**
		EV/IV	mean	6.9 (5.6)	48	6.3 (2.0)	52	0.501
			min.	0.9 (7.9)	48	1.3 (3.5)	52	0.617
			max.	**15.1 (4.7)**	48	**10.9 (2.7)**	52	**<0.01**
			range	**14.2 (7.3)**	48	**9.6 (4.7)**	52	**<0.01**
		IR/ER	mean	-7.8 (8.0)	48	-2.2 (3.3)	52	0.014
			min.	**-12.2 (7.5)**	48	**-5.3 (2.6)**	52	**<0.01**
			max.	-2.4 (8.4)	48	0.9 (3.8)	52	0.488
			range	**9.7 (3.1)**	48	**6.3 (2.5)**	52	**<0.01**

statistically significant differences involve smaller absolute values with equipment B, implying that smaller rotation of the ankle joint complex was measured with the stiffer step-in boots.

During heel-side turns, these differences were significant on the back leg for the range of DF/PF, as well as for the mean, minimum and maximum of IR/ER. On the front leg, the ranges of all three rotations were statistically different, and so were the maximum of EV/IV and the minimum of IR/ER. During toe-side turns, significant differences were observed on the range of DF/PF on both legs, on the mean and maximum DF/PF on the front leg, on the maximum and range of EV/IV on the front leg, on the mean, minimum and maximum of IR/ER on the back leg, and on the minimum and range of IR/ER on the front leg.

These differences must be interpreted in view of the sign convention for the three orthogonal rotations. For instance, because inversion is negative and eversion is positive, a negative value for the parameter called "EV/IV min." represents the maximum inversion rather than the minimum eversion. Compared to equipment A, equipment B was more restrictive on dorsiflexion and on external rotation for both legs; it was also more restrictive on eversion for the front leg only.

5 Development of Ankle Loading Models

One of the objectives of this project is to predict the strain in the ankle ligaments occurring during the trials with the 10 snowboarders. As was shown in Figure 3-1, two types of models were used:

- A statistical model, interpolating in a set of published experimental relationships established *in vitro* between ankle rotations and ligament strains.
- Kinematic models, including the bony and ligamentous elements of the ankle and of the subtalar joints, personalized to each participant's morphology.

This chapter presents the statistical model, three types of kinematic models, and the ligament strains calculated over all the trials with these models.

5.1 Statistical model

As mentioned in Section 2.6.3, three studies have related the strain in ankle ligaments with ankle rotations from measurements done on cadaver specimens. Colville *et al.*[41] reported ligament strains at imposed torque values rather than rotation values in the EV/IV and IR/ER directions. Nigg *et al.*[144] reported normalized ligament lengths (smallest length is 0, largest length is 1) in a manner that is difficult to compare to ultimate strain values. Renström *et al.*[164] reported ligament elongations in percentage of their length measured with the ankle in neutral position (zero rotations). The latter reference provides the only data set that can be used directly as a statistical model to predict ligament strains at the ankle rotations calculated from the experimental data acquired in this project.

For every set of DF/PF, EV/IV and IR/ER calculated from the kinematic measurements on snowboarders, the ATF and CF ligament strains were interpolated or extrapolated from Renström's data set using three-dimensional geometrical kriging (see Appendix H). In equation [G-5], the x, y and z dimensions would stand for the three rotations, and the tilde sign would denote Renström's data. Geometrical kriging has proven efficient when used in problems requiring both interpolation and extrapolation[50]. Figure 5-1 plots the ankle rotation combinations used in Renström's study (black dots) and the mean ankle rotation combination measured during each side-turn in the present study (circles and grey dots). It shows that approximately half of the experimental measurements exceed the limits of Renström's data, thus requiring the use of extrapolation (circles).

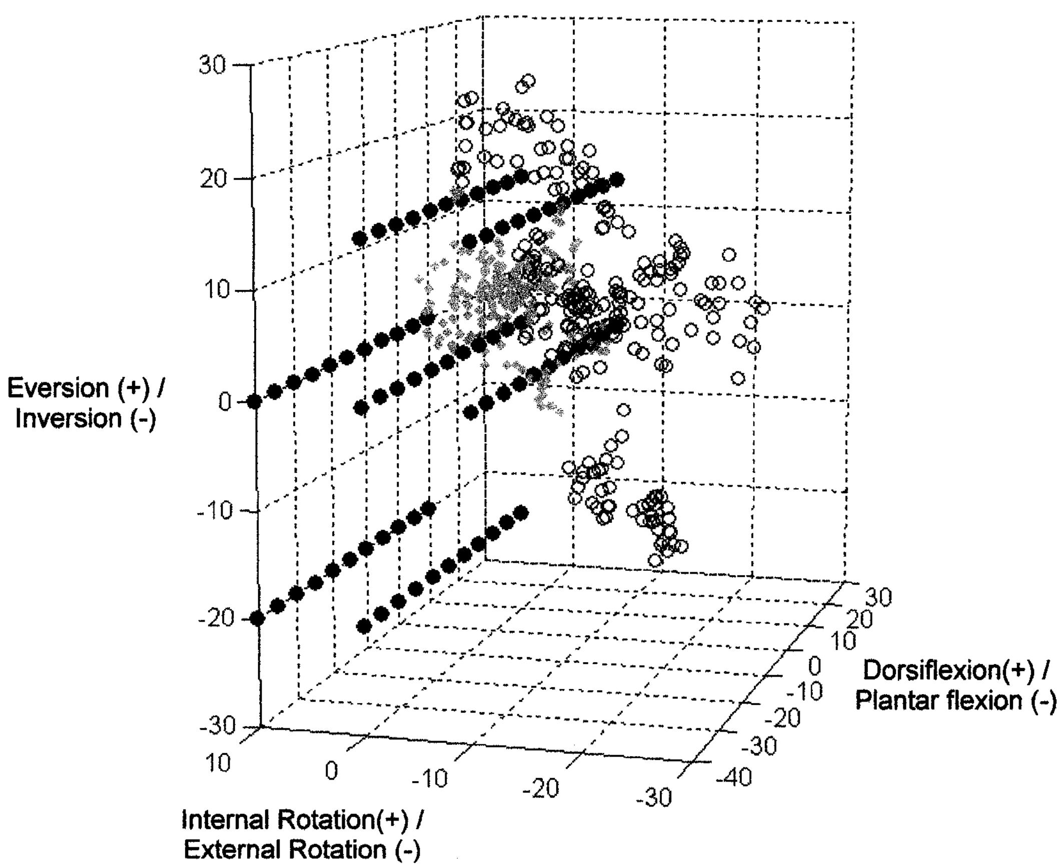

Figure 5-1: Combination of PF/DF, IR/ER and EV/IV measured in the study by Renström *et al.*[164] (black dots), and observed on the snowboarders in the present study (interpolated: cyan dots; extrapolated: red circles).

5.2 Kinematic models

Three kinematic models were constructed based on the principle that the ankle joint complex is a 2-DOF geometry-driven joint made of 3 rigid bodies: the tibia-fibula (TiFi)*, the talus (Ta), and the calcaneus (Ca). Those 3 bodies (Figure 5-2) form a kinematic chain linked by two 1-DOF revolute joints, the talocrural joint between the TiFi and the Ta, and the subtalar joint between the Ta and the Ca. The ligaments involved in the ankle joint complex (ATFL, CFL, PTFL, STTL, TCL) have each of their extremities attached to one of the four bones included in the model (Figure 2-8). For every time step in the experimental data signals, the length of each ligament can be calculated from the distance between its origin and insertion on each bone and the position and

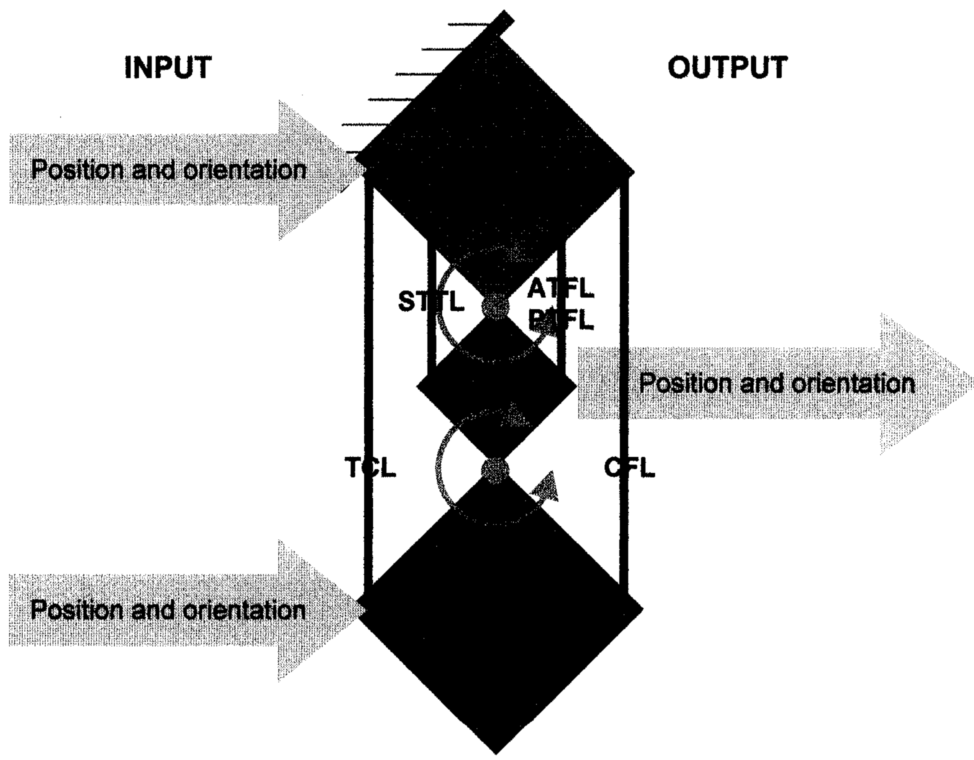

Figure 5-2: Schematic 2-D representation of the kinematic models.

* The relative motion between the tibia and the fibula is neglected.

orientation of each bone at every time frame. During the experiment, the sensors were attached to the tibia and the calcaneus. Thus, the position and orientation of the two ends of the kinematic chains, the TiFi and the Ca, are known. Using them as inputs, the kinematic model solves the position and orientation of the middle link, the Ta. Since the kinematic chain has only 2 DOF and the relative position and orientation of the TiFi with respect to the Ca is known with 6 DOF, there are 4 redundant DOF. The three kinematic models reflect three ways to deal with this redundancy.

The next sub-sections detail the construction of the kinematic models, including the steps that are common to all three models, i.e. the geometrical reconstruction of a cadaver leg specimen, the extraction of axes of rotation as well as ligaments origin and insertion points, and the personalization of the model to the specific morphology of each snowboarder. The three numerical techniques used to solve for the position and orientation of the Ta are then presented. Finally, the prediction of ligament strains is explained.

5.2.1 Generic geometrical model

Computed-Tomography (CT-scan*) images of a cadaver right leg specimen were obtained from and used with permission of the VAKHUM project (Virtual Animation of the Kinematics of the Human for Industrial, Educational and Research Purposes), managed by the Department of Anatomy of the University of Brussels. The donor was an 88-years-old male, 166 cm tall, weighing 56 kg, who died of a heart attack. No

* CT-scan is a medical imaging technique that uses x-rays to produce cross-section images at different locations along of a body part. The x-ray dose for scanning a complete leg is not ethically acceptable for a living human and can only be administered to cadaver specimens.

degenerative bone disease was recorded in the donor's medical file, or apparent on the specimen. The images were acquired at every millimetre along the leg, at a resolution of 512 by 512 pixels with 0.84 mm square pixels. The stacked slices created a volume made of 1.0×0.84×0.84 mm voxels. Bone segmentation* and identification was performed manually on each image, using version 2.3 of the Amira software (TGS Template Graphic Software Inc., San Diego, CA) (Figure 5-3).

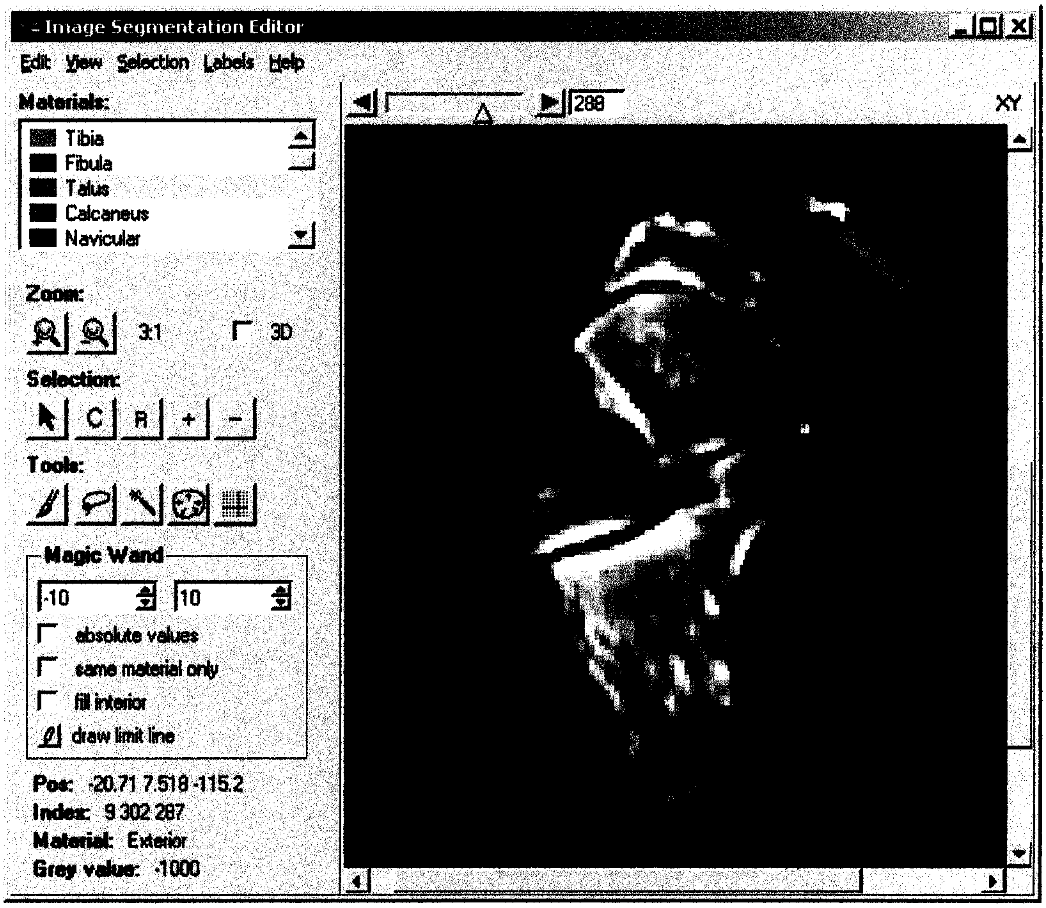

Figure 5-3: Segmentation window in the Amira software displaying a transverse slice of the leg at the ankle level, showing the calcaneus (red), the talus (green) and the navicular bone (blue).

---

* Segmentation is the process of separating the anatomical content of a biomedical image, usually by tagging the pixels that belong to an anatomical structure. In the case of the lower leg and foot, all 24 bones were segmented and given a name.

Once the contour of each bone was identified on each cross-section, a surface model of each bone was created by the Amira software (Figure 5-4). For the lower leg and complete foot, the model used 59755 triangles distributed as follows: 18454 for the tibia, 8496 for the fibula, 3450 for the talus, 5896 for the calcaneus and 23459 for all the other bones in the forefoot.

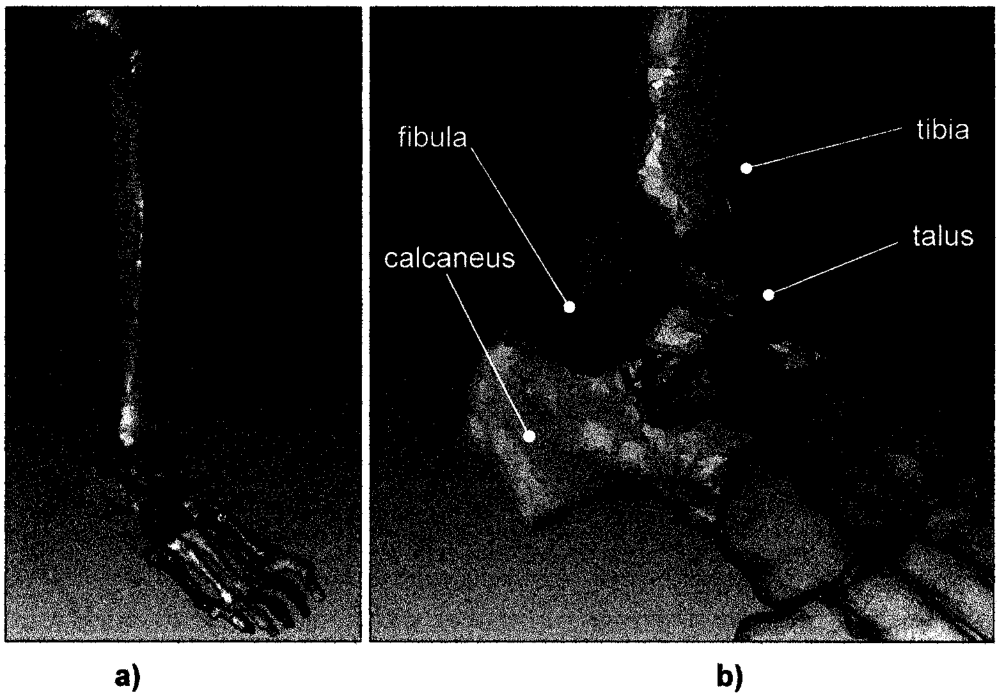

Figure 5-4: Surface model generated and displayed by the Amira software: a) bones of the right lower leg and foot; b) zoom on the ankle, forefoot displayed in transparency.

5.2.2 Axes of rotation

The axes of rotation for the talocrural and the subtalar joints (refer to Figure 2-11 and Figure 2-12 for anatomy) were extracted from the geometry of the articular surface of the talus. A program was developed under Matlab to calculate the cylinder that best fits, in the least square sense, a set of points. As shown on Figure 5-5, a cylinder is defined in 3D space by its axis vector,

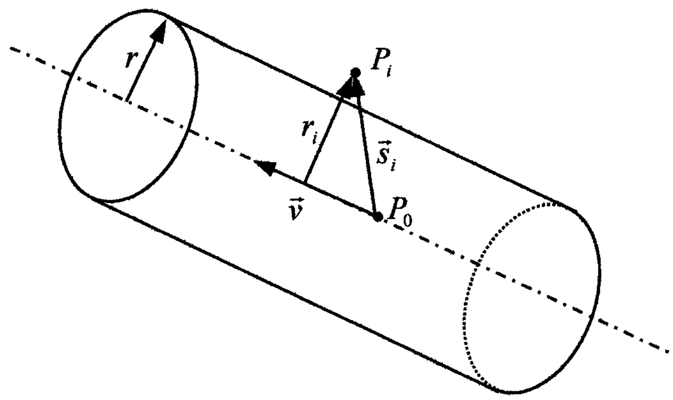

Figure 5-5: Mathematical definition of a cylinder.

$$\vec{v} = a\vec{i} + b\vec{j} + c\vec{k} \qquad [5\text{-}1]$$

a point on its axis,

$$P_0 = (x_0, y_0, z_0) \qquad [5\text{-}2]$$

and its radius, r. For any point $P_i = (x_i, y_i, z_i)$ located on the surface of the cylinder, a vector can be defined as

$$\vec{s}_i = (x_i - x_0)\vec{i} + (y_i - y_0)\vec{j} + (z_i - z_0)\vec{k}\,. \qquad [5\text{-}3]$$

Then, if $\vec{v}$ has unit length, the distance from point P_i to the axis of the cylinder is

$$r_i = \left|\vec{v} \times \vec{s}_i\right|. \qquad [5\text{-}4]$$

Developing [5-4] yields

$$r_i = \sqrt{[b(z_i - z_0) - c(y_i - y_0)]^2 + [c(x_i - x_0) - a(z_i - z_0)]^2 + [a(y_i - y_0) - b(x_i - x_0)]^2}\,. \qquad [5\text{-}5]$$

A constrained non-linear optimization can then be used to find the values for P_0, $\vec{v}$ and r that minimize the least square error given by

$$e = \sum_i \left(r_i^2 - r^2\right) \qquad [5\text{-}6]$$

with the constraint of a unit vector $\vec{v}$

$$a^2 + b^2 + c^2 = 1. \qquad [5\text{-}7]$$

Using this algorithm, a cylinder was best-fitted to the convex surface of the talus that articulates with the tibia, and another cylinder was best-fitted to the concave articular surface of the talus that articulates with the calcaneus (Figure 5-6a). The axis of each cylinder was used as the axis of rotation of the corresponding revolute joint. The axis of the subtalar joint passes through the calcaneus (Figure 5-6b). The axis of rotation of the talocrural joint passes through the talus but does not coincide with the line that joins the medial and lateral malleoli (Figure 5-6c).

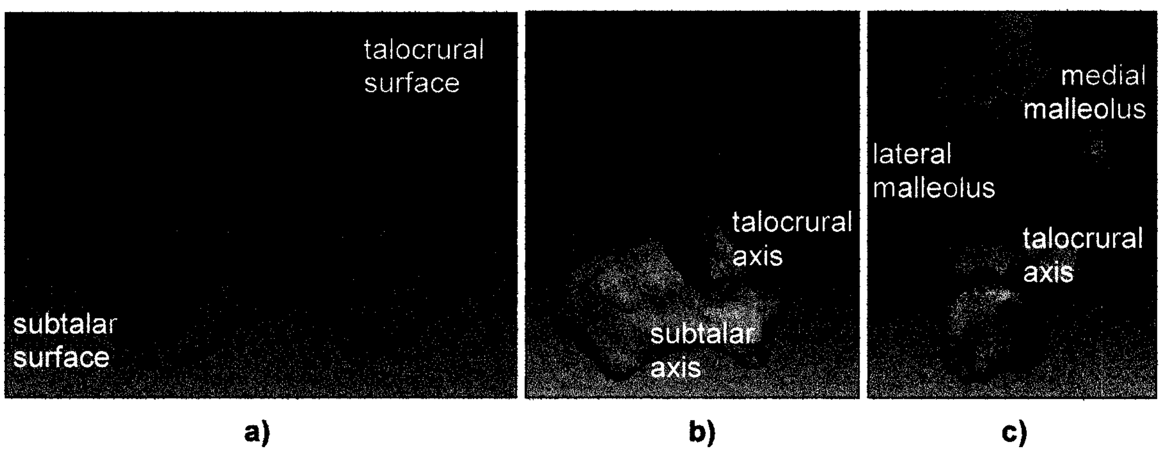

Figure 5-6: Axes of rotation: a) articular surfaces in orange on an antero-lateral view of the transparent talus (the subtalar surface is seen from inside the talus); b) axes of rotation in orange displayed with the calcaneus, talus and tibia in lateral view; c) malleoli and axis of the talocrural joint with the calcaneus, talus, tibia and fibula in frontal view.

5.2.3 Ligaments

The origin and insertion points of ligaments were identified interactively on the surface model in the Amira software, based on anatomy drawings[25,72,127,141,156]. On the medial side (Figure 5-7a), the deltoid ligament complex has its origin on the tibia, and two insertions, on the calcaneus and talus, corresponding to two of its superficial fascicles, namely the TCL, and the STTL (see Figure 2-8 for anatomy). On the lateral side (Figure 5-7b), each ligament has its origin on the fibula and its insertion on the calcaneus (CFL) or the talus (ATFL, PTFL).

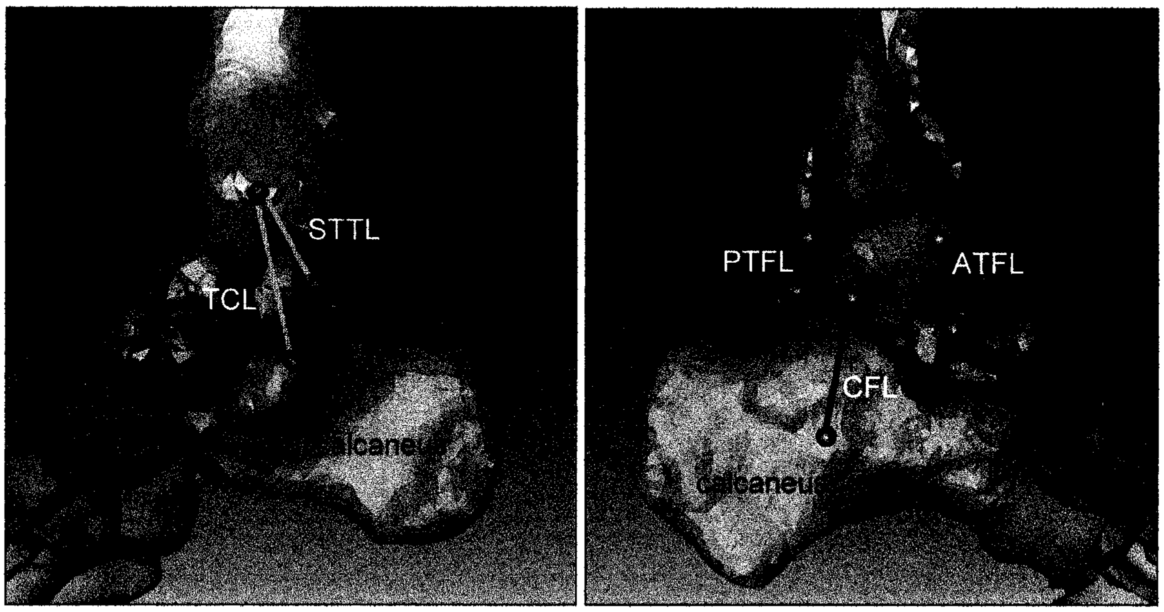

a) b)

Figure 5-7: Origin and insertion points of ankle ligaments on the a) medial side and b) lateral side of the ankle.

5.2.4 Personalization

The geometrical model was personalized to each snowboarder's specific morphology in four steps.

1. The same anatomical landmarks used for the anatomical calibration (Table 3-1, Figure 3-7) were identified on the surface model in the Amira software (Figure 5-8). Those points provide enough data to define a BECS on the foot bones (talus, calcaneus) and a BECS on the shank bones (tibia, fibula). The bones in the surface model were expressed in their respective BECS. A left leg surface model was also created from the right leg surface model by making a mirror copy across the sagittal plane (inversion of the z coordinates of all the points).
2. From the anatomical calibration data measured on a snowboarder, the rigid body transformation to express the foot BECS in the shank BECS was calculated. This transformation was applied to the bones in the surface model that were expressed in the foot BECS (talus, calcaneus).

The effect of these first two steps is to rotate the ankle of the surface model so that it is oriented like the ankle of the snowboarder that was measured.

3. A 3D deformation was calculated using 3D geometrical kriging to fit the anatomical landmarks on the surface model (points $\widetilde{P}_j$ in equation [G-1]) onto the anatomical landmarks measured on the snowboarder (points P_i in equation [G-2]), by solving equation [G-5].
4. The deformation was applied to every point on the surface model, ligament origin and insertion point and axis of rotation.

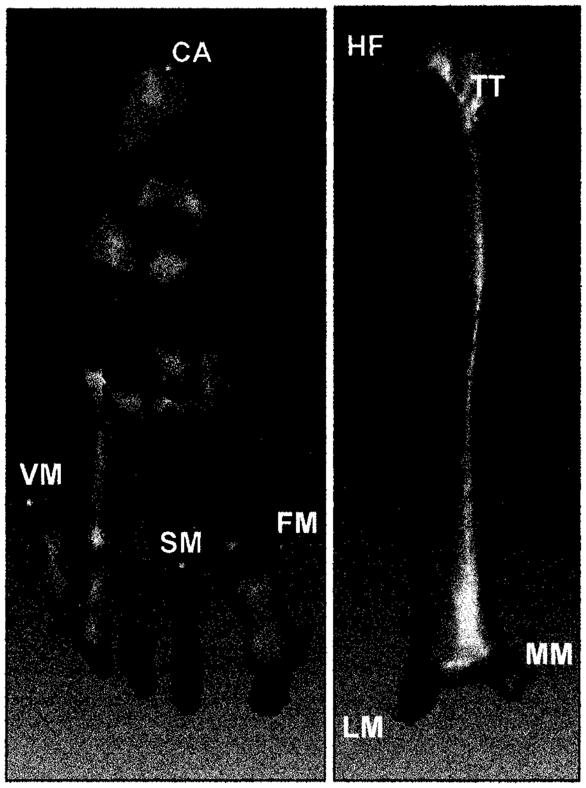

Figure 5-8: Anatomical landmark identification on the surface model: a) foot bones, b) shank bones.

The geometrical reconstruction of a cadaver leg specimen (Section 5.2.1), the extraction of the axes of rotation (Section 5.2.2), the identification of ligament origins and insertion points (Section 5.2.3), and the identification of anatomical landmarks (step 1 of the personalization) are tasks that were done only once for the whole project. However, steps 2 to 4 of the personalization were done for every anatomical calibration measured, i.e. twice for each snowboarder (once for every type of snowboarding equipment).

5.2.5 Solution

For every time step in the experimental data signals, the position and orientation of the talus was predicted from the kinematic measurements using three methods. The first method uses optimization tools to minimize the misalignment between the axes of rotation. The last two methods consider the open kinematic chain made of the Ca, Ta and TiFi as a 2-joint robotic arm, and use inverse kinematics to calculate the joint rotations that will give the desired position and orientation of its tool relative to its base. The last two methods differ slightly in the way the solution is constrained. These three methods are described in the following sub-sections.

5.2.5.1 Kinematic model #1: Axes matching

An axis of rotation between two rigid bodies can be completely described in 3D by two points expressed in the local coordinate system (LCS) of each body. For instance in Figure 5-9, points P_1 and P_2 are expressed in LCS_A by vectors $\vec{v}_{1A}$ and $\vec{v}_{2A}$, and in LCS_B by vector $\vec{v}_{1B}$ and $\vec{v}_{2B}$. These vectors can be transformed into the global coordinate system (GCS) using the transformation matrices that describe the position

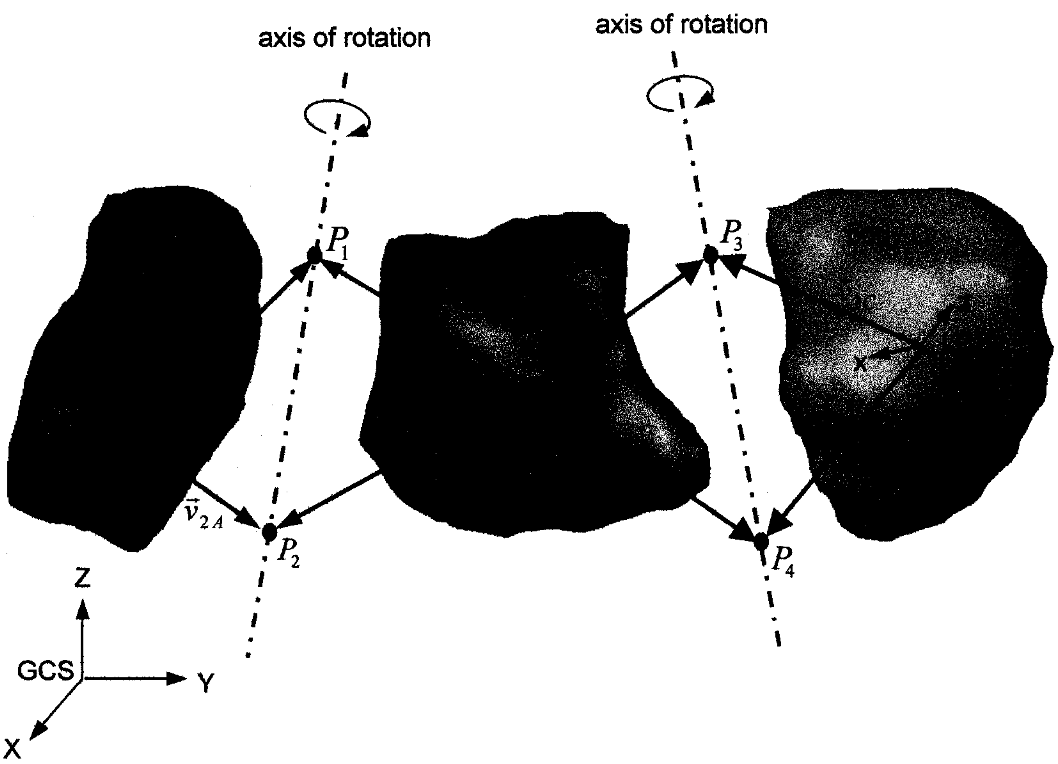

Figure 5-9: Axes matching with three rigid bodies.

and orientation of bodies A and B, ${}_{GCS}[M]^{LCS_A}$ and ${}_{GCS}[M]^{LCS_B}$:

$$\vec{v}_1 = {}_{GCS}[M]^{LCS_A}\,\vec{v}_{1A} \qquad [5\text{-}8]$$

$$\vec{v}_1 = {}_{GCS}[M]^{LCS_B}\,\vec{v}_{1B}\,. \qquad [5\text{-}9]$$

Two expressions are written similarly for $\vec{v}_2$:

$$\vec{v}_2 = {}_{GCS}[M]^{LCS_A}\,\vec{v}_{2A} \qquad [5\text{-}10]$$

$$\vec{v}_2 = {}_{GCS}[M]^{LCS_B}\,\vec{v}_{2B}\,. \qquad [5\text{-}11]$$

The axis of rotation constrains [5-8] and [5-9], as well as [5-10] and [5-11], to be equal.

$${}_{GCS}[M]^{LCS_A}\,\vec{v}_{1A} = {}_{GCS}[M]^{LCS_B}\,\vec{v}_{1B} \qquad [5\text{-}12]$$

$${}_{GCS}[M]^{LCS_A}\,\vec{v}_{2A} = {}_{GCS}[M]^{LCS_B}\,\vec{v}_{2B}\,. \qquad [5\text{-}13]$$

Similarly for $\vec{v}_3$ and $\vec{v}_4$, between body B and body C,

$${}_{GCS}[M]^{LCS_C}\,\vec{v}_{3C} = {}_{GCS}[M]^{LCS_B}\,\vec{v}_{3B} \qquad [5\text{-}14]$$

$${}_{GCS}[M]^{LCS_C}\,\vec{v}_{4C} = {}_{GCS}[M]^{LCS_B}\,\vec{v}_{4B}\,. \qquad [5\text{-}15]$$

For the ankle, body A is the tibia-fibula, body B is the talus, and body C is the calcaneus. Vectors $\vec{v}_{1A}$ $\vec{v}_{2A}$, $\vec{v}_{1B}$, $\vec{v}_{2B}$, $\vec{v}_{3B}$, $\vec{v}_{4B}$, $\vec{v}_{3C}$ and $\vec{v}_{4C}$ are calculated from the axes of rotations extracted from the articular surface of the talus as explained in Section 5.2.2. Since the position and orientation of the tibia-fibula and the calcaneus are known in the GCS at every time frame, then matrices ${}_{GCS}[M]^{LCS_A}$ and ${}_{GCS}[M]^{LCS_C}$ are known. The only unknown is matrix ${}_{GCS}[M]^{LCS_B}$.

Even if it is a 4-by-4 matrix with 16 components like Equation [3-2], ${}_{GCS}[M]^{LCS_B}$ really represents 6 independent unknowns, 3 for the position (x, y, z) and 3 for the orientation (θ_x, θ_y, θ_z). Equations [5-12] to [5-15] provide 12 independent equations (x, y, and z component for each equation) to solve for the position and orientation of body B. Hence, the system is over-determined. Moreover, because of measurement and model uncertainties, there may not exist a solution that perfectly satisfies [5-12] to [5-15] anyway. Therefore, an optimization technique was chosen to iteratively solve for x, y, z, θ_x, θ_y and θ_z, with the following steps:

1. The 6 variables are set to represent the talus in the position and orientation it had with respect to the calcaneus on the surface model of the cadaver specimen.
2. Matrix ${}_{GCS}[M]^{LCS_B}$ is calculated from the 6 variables using [3-2] and [3-3].
3. An objective function $f(x,y,z,\theta_x,\theta_y,\theta_z)$ is calculated as the sum of the vector differences between the right-hand-side and the left-hand-side of [5-12] to [5-15].

$$\vec{e}_1 = {}_{GCS}[M]^{LCS_A}\,\vec{v}_{1A} - {}_{GCS}[M]^{LCS_B}\,\vec{v}_{1B} \qquad [5\text{-}16]$$

$$\vec{e}_2 = {}_{GCS}[M]^{LCS_A}\,\vec{v}_{2A} - {}_{GCS}[M]^{LCS_B}\,\vec{v}_{2B}. \qquad [5\text{-}17]$$

$$\vec{e}_3 = {}_{GCS}[M]^{LCS_C}\,\vec{v}_{3C} - {}_{GCS}[M]^{LCS_B}\,\vec{v}_{3B} \qquad [5\text{-}18]$$

$$\vec{e}_4 = {}_{GCS}[M]^{LCS_C}\,\vec{v}_{4C} - {}_{GCS}[M]^{LCS_B}\,\vec{v}_{4B}. \qquad [5\text{-}19]$$

$$f(x,y,z,\theta_x,\theta_y,\theta_z) = \sum_{i=1}^{4} \left|\vec{e}_i\right|. \qquad [5\text{-}20]$$

4. An unconstrained optimization algorithm (optimization toolbox in Matlab) is used to iteratively calculate the x, y, z, θ_x, θ_y and θ_z values that minimizes the objective function in [5-20].

5. The optimized values are used as an initial guess for the next time step of the experimental data signal, and the process goes back to step 2 until the end of the experimental data signal is reached.

5.2.5.2 Kinematic model #2: Inverse kinematics

Mechanically, the ankle can be compared to a type of robot called a serial-link manipulator (Figure 5-10), consisting of a set of bodies called links, connected by joints and forming an open kinematic chain. In a serial-link manipulator, each joint has one translational or rotational DOF. In a manipulator with n joints numbered from 1 to *n*, there are *n*+1 links numbered from 0 to *n*. Link 0 is the base of the manipulator, which is generally fixed, and link *n* is the end-effector.

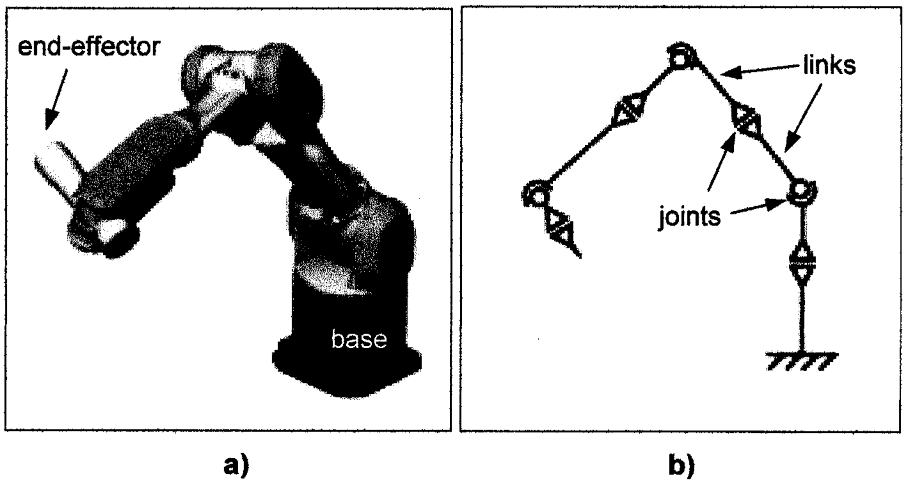

Figure 5-10: Example of a serial-link manipulator in a) solid view and b) schematic view (adapted from http://www.meganic.dk/old/parallelrobots.html. © Copyright 2002, Meganic ApS. Reprinted with permission).

The Denavit-Hartenberg[53] formulation is a systematic way to mathematically describe links and joints (Figure 5-11). It first defines axis z_{i-1} along axis of joint i and axis z_i along the axis of joint i+1. Axis x_i is then defined perpendicularly to axes z_{i-1} and z_i. Finally, axis y_i is the cross product of z_i and x_i.

Only two parameters are necessary to describe the link:

Link length (a_i): the distance between axes z_{i-1} and z_i, along the x_i axis.

Link twist (α_i): the angle from axis z_{i-1} to axis z_i, about the x_i axis.

Two parameters describe the joint:

Link offset (d_i): the distance between the x_{i-1} and x_i axes, along the z_{i-1} axis.

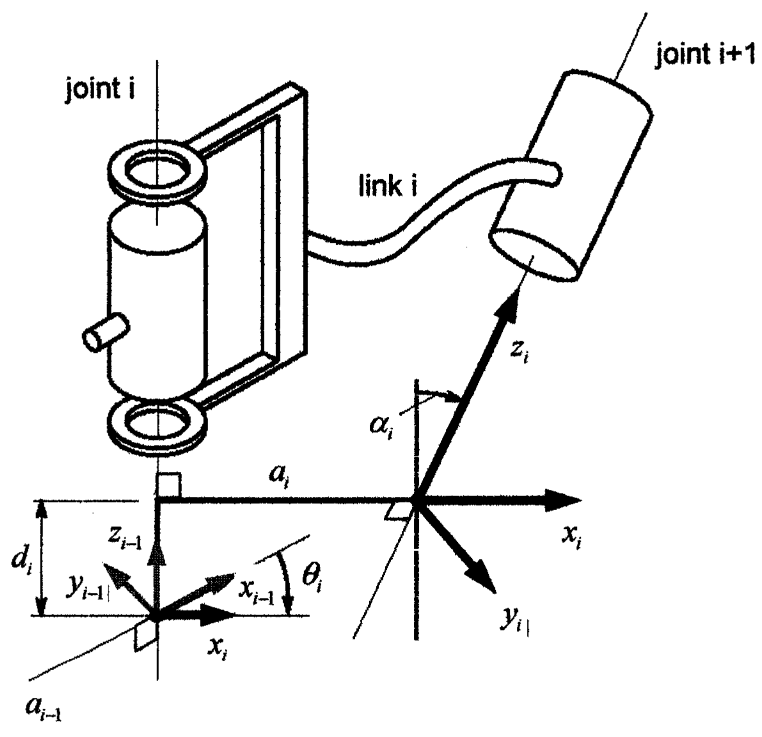

Figure 5-11: Denavit-Hartenberg parameter definition (adapted from Jochheim et al., 1999[90], reproduced with permission).

Joint angle (θ_i): the angle from axis x_{i-1} to axis x_i, about the z_{i-1} axis.

The ankle can be modeled as a serial-link manipulator of 4 links connected by 3 joints, as described in Table 5-1. The base (link 0) is the tibia-fibula and is considered fixed. The end-effector (link 3) is the sensor on the calcaneus, which is considered to be rigidly attached to the calcaneus (link 2) through a 0 DOF joint called skin (joint 3).

Table 5-1: List of joints and links in the ankle model.

	Joint		Link	
	name	**type**	**name**	**type**
0			tibia-fibula	base
1	talocrural	rotational	talus	
2	subtalar	rotational	calcaneus	
3	skin	rigid	sensor	end-effector

For each link, the four Denavit-Hartenberg parameters (a_i, α_i, d_i, θ_i) were calculated from the anatomical calibration data and from the axes of rotation extracted from the surface model. The system was solved using a Matlab inverse kinematics toolbox developed by Corke[42] and available freely over the internet.[*] The "ikine" function (for inverse kinematics) requires as input the geometry of the serial-link manipulator (link parameters), the type of joint (translational, rotational), and the rigid transformation matrix between the end-effector (calcaneus sensor) and the base (tibia-fibula). It computes the solution iteratively with the pseudo-inverse of the manipulator Jacobian matrix, and outputs the rotation (θ_i) or translation (d_i) value at each joint.

If the manipulator has less than 6 joints, it may not be possible for the end-effector to satisfy all possible positions and orientations. To bypass this problem, the *ikine* function allows requesting the end-effector to satisfy only some selected DOF amongst the 3 positions and 3 orientations. In the present case, the ankle has only two joints. Therefore, only two DOF were used, namely the x and z positions. These two specific DOF were chosen because the rotation of the ankle with the widest range of motion, the DF/PF (see Figure 4-3 and Figure 4-4), occurs in the sagittal plane, which correspond approximately to the x-z plane of the base link.

After the joint rotations were calculated, the forward kinematics was calculated on a one-joint serial-link manipulator ending at the talus with the "fkine" function (for forward kinematics). This function generated the transformation matrix between the talus (end-effector) and the tibia-fibula (base), from which the position and orientation of the talus in the GCS was calculated.

5.2.5.3 Kinematic model #3: Inverse kinematics with constrained joint rotations

Kinematic model #2 does not limit the rotation around the two joints. This sometimes creates situations where the talus would penetrate into the calcaneus, whereas in reality the rotation around the subtalar joint is physically limited by bone surfaces. In order to solve this bone collision problem, a constraint was imposed on the rotation at the subtalar joint. This third kinematic model is thus essentially the same as model #2, except that a constraint was imposed on the minimum and maximum rotation at the subtalar joint.

Because the *ikine* function does not allow imposing a limit to a joint, an iterative approach was chosen, using Matlab's constrained optimization with the *fkine* function. The range of motion at the subtalar joint was limited to 10°, based on reported experimental values ranging from 4 to 14°.[110]

---

* http://www.cat.csiro.au/cmst/staff/pic/robot

5.2.6 Ligament elongations and strains

Once the positions and orientations of all the bones in the ankle are found for every time step in the experimental data signals (TiFi and Ca directly from experimental measurements, Ta from the predictions of the kinematic models), the elongations of the ligaments can be calculated from the distance between the origin and insertion points of each ligament. In order to compare these results to the ones obtained with the statistical model, ligament strains were calculated using

$$\varepsilon = \frac{L - L_0}{L_0} \qquad [5\text{-}21]$$

where L is the length of the ligament

L_0 is the initial length of the ligament.

Because it is not possible to know the length of the ligament in its un-stretched state, the value for L_0 was taken when the ankle is in neutral position, i.e. 0° for all three anatomical rotations. Therefore, ε is a relative strain.

6 Analysis of the Results and Discussion

Section 6.1 discusses the limitations of the present study related to the experiment design and method. More particularly, the measurement uncertainties from various sources are identified and estimated, and their effect on the rotations of the ankle joint complex is evaluated. In Section 6.2, the experimental results are examined and interpreted. The data are analysed first as a single group and then as two groups separated according to the type of snowboard equipment.

In Section 6.3, the assumptions behind the statistical and kinematic models used to predict ligament strains are discussed and, when possible, expressed in terms of uncertainties on model parameters. The effect of these model parameter uncertainties on ligament strain predictions is evaluated. Finally, Section 0 presents the ligament strains predicted by the models and discusses their biomechanical significance.

6.1 Limitations of the experiment

6.1.1 Study design and control of experimental conditions

One of the main limitations of this study is the small number of snowboarders enrolled. Although one may plausibly assess that the intra-individual variability is adequately represented by having the snowboarders perform 3 trials of 10 turns each, it is still debatable whether the small snowboarder sample is representative of the inter-individual variability found in the snowboarder population. Remember, however, that the objective of the present study was not to gather statistics on snowboarder performance but to identify possible differences on each snowboarder's characteristics due to differences in types of equipment. Thus, conclusions drawn from comparisons of equipment effects on individuals would likely be more representative of a larger sample than those drawn from averages on the values measured.

Another issue of concern is whether the results might have been biased by differences in experimental conditions, such as the outside temperature or the type of snow. For example, one might argue that temperature differences might have affected the stiffness of the boot materials. To reduce or eliminate such effects, we scheduled each snowboarder's trials with the two types of boots on the same day, such that the temperature could be assumed to be approximately the same for the two types of boots. Again, this approach validates conclusions drawn from equipment comparison more than those based on average values.

6.1.2 Fastrak system accuracy

The accuracy of the Fastrak system is reported by the manufacturer to be 0.8 mm for position values (verified experimentally in the present project, see Section F.3) and 0.15° for orientation values. The combined uncertainty of experimental rotation values for the ankle joint complex (see Appendix I for details on the method), as shown in Table 6-1, is almost always less than 1 degree, even with a measurement uncertainty 4 times larger than the Fastrak manufacturer's specifications.

6.1.3 Skin movement artefact

In the present study, position and orientation sensors attached to the skin are used to measure the kinematics of the underlying bones. These sensors are assumed to be rigidly linked to the bones, while in fact there exists some movement between the sensor and the bones. This phenomenon, referred to as "skin movement artefact", has been observed and measured in other studies[29,32,66,81,116,123,124,128,163]. The most obvious

Table 6-1: Combined uncertainties of rotations of the ankle joint complex. Estimated measurement uncertainties are in boldface font. Other values illustrate the sensitivity of the rotations to uncertainties.

uncertainty		DF/PF	EV/IV	IR/ER
Fastrak system accuracy	**0.8 mm, 0.15°**	**0.1°**	**0.2°**	**0.3°**
	1.6 mm, 0.30°	0.2°	0.4°	0.6°
	3.2 mm, 0.60°	0.5°	0.8°	1.2°
skin movement artefact	2 mm, 0.75° (shank) 1 mm, 1.5° (foot)	1.9°	2.6°	1.1°
	4 mm, 1.5° (shank) 2 mm, 3° (foot)	**3.6°**	**5.1°**	**2.2°**
	8 mm, 3° (shank) 4 mm, 6° (foot)	7.5°	10.9°	4.5°
anatomical landmark identification	2 mm	1.0°	0.5°	1.1°
	5 mm	**2.1°**	**1.2°**	**2.3°**
	10 mm	5.8°	3.2°	6.6°

workarounds to this problem involve either using external markers attached to metal pins percutaneously screwed into the bones, or using fluoroscopy, a system that produces dynamic radiographic images. For ethical and practical reasons, these invasive techniques could not be used in the present study. Having observed larger skin movement in areas with thick underlying soft tissues or close to joints, some researchers[8,124] have had some success in alleviating this problem by attaching the sensors to rigid plates glued to the skin in order to filter out local skin motion. Others[5,30,31,116] have developed techniques to numerically compensate for skin movement by measuring the geometric distortion of a cluster of sensors attached to the skin. However, such techniques require several sensors to be attached to the same body segment and are more appropriate for 3-DOF optical measurements rather than 6-DOF electromagnetic measurements.

In the present experiment, every precaution was taken to minimize skin movement artefacts. The locations of sensor attachment were chosen based on the thickness of underlying tissue, proximity of a joint and constraints relative to the snowboard boots. The tibial sensor was placed at a couple of centimetres above the top of the boot to make sure that the boot did not push the sensor upwards when the snowboarder dorsiflexed his ankle. It was also located over very thin skin covering a flat part of the tibia, facing the antero-medial direction. Moreover, a thermoplastic plate was moulded to the skin of each snowboarder and glued on the skin under the sensor. This part of the tibia was also shaved to make the glue bond more resistant. The calcaneal sensor was located over thin underlying tissue. A thermoplastic heel cup was moulded to the snowboarder's heel and glued to his skin.

Even with these precautions, skin movement artefact was not completely avoided in the present study. Based on reported values[32,128], it was estimated as 4 mm and 1.5° for the shank and 2 mm and 3° for the foot (see Section I.2 for details). These uncertainties due to skin movement propagate to ankle joint complex rotations with uncertainties between 2 and 5° (Table 6-1), which are nearly one order of magnitude greater than uncertainties due to the Fastrak accuracy. This makes skin movement artefact the biggest source of uncertainty on the rotations of the ankle joint complex.

6.1.4 Anatomical landmark identification

The anatomical landmarks measured with the Fastrak system are bony landmarks located through the skin by palpation. Based on reported intra-observer repeatability of the identification and measurement of those landmarks[48], the uncertainty of the anatomical landmarks was estimated at 5 mm on the x, y and z coordinates. The propagation of this uncertainty to rotations of the ankle joint complex is limited to 1 or 2°, as shown in Table 6-1. The uncertainty associated with the Fastrak system accuracy is very small compared to the anatomical landmark identification uncertainty. Even when considering the use of a stylus to measure those points, the Fastrak system uncertainty does not increase substantially. The orientation uncertainty (0.15°), combined with the length of the stylus (115 mm), would only add 0.3 mm at the tip of the stylus to the 0.8 mm positional uncertainty at the sensor.

Because only one anatomical calibration was done for each type of snowboarding equipment, differences in ankle rotations between the two types of equipment must be considered carefully, to ensure that they cannot be caused by measurement uncertainty alone. This possibility was discarded, because the smallest statistically significant differences in rotations detected by the Mann-Whitney U-tests (2.4° in DF/PF, 4.2° in EV/IV and 2.6° in IR/ER, Table 4-3 and Table 4-4) were all found to be larger than these uncertainties.

6.2 Interpretation of the measured rotations of the ankle joint complex

The experimental results are first analysed for the average heel-side and toe-side turns, then in two groups according to equipment type.

6.2.1 Average heel-side and toe-side turns

Disregarding the type of snowboard equipment used, one would find that, during both the average heel-side turn (Figure 4-3) and the average toe-side turn (Figure 4-4), the front ankle joint complex (AJC) was everted, while the back AJC was slightly inverted (Figure 2-9). These observations could be attributed to an effort of the snowboarders to centre their weight over the front leg in order to achieve better control of the snowboard with the back leg. This hypothesis is consistent with Bally and Taverney's[14] observation of a higher normal force under the front foot than under the back foot of snowboarders.

Dorsiflexion on the back AJC was also observed to be 10 to 12° higher than on the front AJC, during both heel-side and toe-side turns. This observation suggests that minimum flexion of the bindings should be asymmetrically set through different adjustment of the highbacks for the two feet.

Both feet were externally rotated, although the legs were rotated slightly more towards the nose of the snowboard during heel side turns than during toe-side turns. This observation, along with the asymmetric dorsiflexion, probably reflects a tendency of the snowboarders to turn their trunk toward the nose of the snowboard during heel-side turns. During the toe-side turns, both AJC dorsiflexed by 12 to 14° more than they did during the heel-side turns, as the snowboarders shifted their centre of gravity past the toe-side edge of the snowboard.

Asymmetries in snowboarder's body positions and joint rotations are clearly documented by the present results, although the information available is not sufficient to decide conclusively whether the asymmetry in binding settings contributes significantly to the asymmetry in ankle joint rotations or not. Nonetheless, one could speculate that the shift in binding settings toward the nose of the snowboard might have helped the snowboarder shift his trunk forward, thus reducing the asymmetrical rotations of his AJC.

6.2.2 Equipment comparison

The effect of boot stiffness (Table 4-3, Table 4-4) is most clearly observed in DF/PF for which a smaller range of motion is observed with stiff step-in boots (equipment B) than with soft boots (equipment A). Moreover, in toe-side turns, mean and maximum DF on the front leg were also found to be smaller with step-in boots. In other situations, mean, maximum and minimum DF/PF values were too scattered for their differences to be statistically significant.

Equipment differences also manifest on the front leg in a lower range and maximum EV allowed by the stiff step-in boots than by the soft boots. The front leg is the one with the EV/IV values furthest from the neutral position (0° rotation). Close to the neutral position, the difference in stiffness between the two boots would not create rotation differences large enough to be detected with the present experimental method.

External rotation is represented by negative IR/ER values. Therefore, the minimum IR/ER values correspond to the maximum ER and an increase in IR/ER values means a decrease in ER. The ER on the back leg with the soft boots was shifted towards the neutral position with the step-in boots, as seen by an increase of mean, minimum, and maximum values, without any significant change in range. On the front leg, the range of ER was reduced and the minimum IR/ER values were increased with step-in boots. These differences could mean that the step-in boots provide more resistance to external rotation of the foot than the soft boots.

Internal rotation, inversion and plantar flexion are AJC rotations that stretch the anterior talofibular ligament (ATFL), which is the most often sprained ligament of the ankle. Very little movement of these types was observed in the present work. On the contrary, most of the time, both feet were externally rotated, everted and dorsiflexed. In these situations, the statistical or kinematic models are not expected to predict any significant differences in ATFL strains. Therefore, it is very difficult to assess whether one type of snowboard equipment would better protect the ATFL against overstretching than the other from the experimental data alone.

6.3 Limitations of the models

The statistical and kinematic models used to predict ligament strains each have their strengths and weaknesses. The hypotheses behind the construction of each model and the sensitivity of their predictions to various sources of uncertainty are discussed below.

6.3.1 Statistical model

The statistical model is based on experimental data rather than theoretical relationships between the ankle kinematics and ligament strains. Because it expresses average relationships based on measurements done on only 5 specimens, it cannot be expected to take into account the inter-individual variability of the snowboarder sample in the present study. Moreover, compared to other experimental studies, the strain values reported by Renström *et al.*[164] and used in the statistical model are relatively small. For instance, for the ATFL in DF/PF only, Ozeki *et al.*[147] measured 12 cadaver specimens and reported average strain values ranging from –3.5% at 10° DF to +3.5% at 40° PF, whereas Renström *et al.* reported values of –0.6% to +2.1% for the same DF/PF range. Colville *et al.*[41] reported values even higher with 10 specimens, although it is unclear how their zero strain value was defined. Whether this discrepancy in the results from different studies is due to the measurement technique (Hall effect strain transducer for Renström *et al.*, liquid-filled strain gauges for Colville *et al.* and Ozeki *et al.*), the age of the specimens, or solely to inter-individual variability and small number of specimens cannot be determined. Based on all above considerations, we may assert that the values used in the statistical model would more likely be approximately 60% lower than actual ligament strains.

The values predicted by the statistical model depend on the rotations of the ankle joint complex. Therefore, measurement uncertainties that propagate to rotations of the ankle joint complex also propagate to ligament strains predicted by the statistical model. Table 6-2 shows that skin movement artefact and anatomical calibration uncertainty play an important role.

Finally, the statistical model only predicts the strain in the ATFL and CFL, pointing out the need for more data on other ligaments of the ankle.

6.3.2 Kinematic models

The kinematic models are personalized to the geometry of each snowboarder and should thus better represent the inter-individual variability than the statistical model. Even so, present analysis cannot determine the extent by which the personalization of a generic model through a 3D deformation based on 8 points accurately represents the morphology of the leg of a particular individual.

The talocrural and subtalar joints are modelled as pure revolute joints, i.e. joints that only allow rotation about a fixed axis. As mentioned in sections 2.2.4 and 2.8, even though this simplifying hypothesis has been used in several other models[58,155,174,187,194], there is experimental evidence showing that the axis of rotation of the talocrural[22,61,109,117,120,161,181] and subtalar[86,87,126,195] joints move continuously throughout the entire range of motion. This simplification can be represented by an uncertainty on the position and orientation of the axes of rotation and was estimated from reported data on instantaneous helical axis dispersion[22,110] (Section I.3). The propagation of this uncertainty to the prediction of ligament strain is presented in Table 6-2.

Table 6-2: Propagation of uncertainties to ligament strain (in %) predicted with the statistical model (S) and the three kinematic models (K1, K2, K3). Estimated measurement and model parameter uncertainties are in boldface font. Other values illustrate the sensitivity of the ligament strains to uncertainties.

Source of uncertainty	Uncertainty value	ATFL				CFL				PTFL			TCL			STTL		
		S	K1	K2	K3	S	K1	K2	K3	K1	K2	K3	K1	K2	K3	K1	K2	K3
Fastrak system accuracy	**0.8 mm, 0.15°**	**0.05**	**11**	**0.11**	**0.03**	**0.08**	**2.4**	**2.4**	**2.4**	**5.6**	**1.3**	**0.19**	**1.9**	**1.9**	**1.9**	**2.7**	**0.91**	**0.18**
	1.6 mm, 0.30°	0.10	47	0.23	0.06	0.16	5.0	5.1	5.1	8.3	2.5	0.34	3.9	3.9	3.9	6.4	1.8	0.34
	3.2 mm, 0.60°	0.20	24	0.53	0.11	0.32	9.8	10.0	10.0	10	4.9	0.62	7.5	7.6	7.6	9.3	3.4	0.57
skin movement artefact	2 mm, 0.75° (shank) 1 mm, 1.5° (foot)	0.45	22	0.71	0.23	0.71	10	10	10	13	6.2	1.3	7.6	7.6	7.6	9.9	4.5	1.2
	4 mm, 1.5° (shank) 2 mm, 3° (foot)	**0.89**	**32**	**3.4**	**0.45**	**1.40**	**21**	**21**	**21**	**17**	**13**	**2.0**	**14**	**15**	**15**	**17**	**17**	**1.9**
	8 mm, 3° (shank) 4 mm, 6° (foot)	1.84	44	7.4	0.79	2.89	41	41	41	27	18	3.7	29	29	29	30	20	3.5
anatomical landmarks identification	2 mm	0.18	32	1.1	1.2	0.31	3.8	3.8	3.8	6.5	2.0	1.6	2.6	2.6	2.6	4.2	2.0	1.8
	5 mm	**0.40**	**44**	**4.3**	**1.8**	**0.70**	**12.7**	**12.8**	**12.8**	**11**	**6.0**	**2.5**	**5.7**	**5.7**	**5.7**	**7.1**	**5.6**	**3.4**
	10 mm	1.15	50	5.6	6.6	1.93	16.1	16.1	16.1	13	6.0	6.8	9.5	9.4	9.4	11	12	10
axes of rotation (talocrural, subtalar)	1.9°, 3.05°		99	2.1	0.64		0	0	0	15	7.1	2.4	0	0	0	18	5.3	2.2
	3.8°, 7.1°		**49**	**2.4**	**0.50**		**0**	**0**	**0**	**11**	**8.4**	**2.2**	**0**	**0**	**0**	**7.5**	**5.9**	**2.2**
	7.6°, 14.2°		41*	3.3	0.28		0	0	0	13	9.6	1.5	0	0	0	7.1	9.1	1.6
ligament origin and insertion points	0.5 mm		2.4	2.4	2.1		1.0	1.1	1.1	0.96	0.79	0.52	0.51	0.52	0.52	0.88	1.3	1.0
	2 mm		**11**	**9.6**	**8.5**		**4.4**	**4.5**	**4.5**	**2.5**	**3.3**	**2.2**	**2.0**	**2.1**	**2.1**	**3.0**	**4.9**	**3.8**
	5 mm		28	30	30		9.2	9.4	9.4	9.1	13	7.8	3.6	3.7	3.7	6.5	12	8.9
	10 mm		29	37	33		24	24	24	13	16	12	8.3	8.4	8.4	12	22	18

* In this particular case, rotations were unresolved for 4.4% of measured data points.

In the kinematic models, each ligament is represented as one straight fibre with each end attached to a bone at a unique point. This is a simplification of anatomy. Ankle ligaments have been shown to consist of multiple fibres, attached to the bones over a small but not negligible area, and progressively recruited over the entire range of motion of the ankle joint complex[25,156].

The origin and insertion of each ligament was interactively identified virtually on a 3D surface model of the four bones included in the model with the help of precise anatomical descriptions and figures. The repeatability of this identification was estimated to be approximately 2 mm in the x, y and z directions, a value smaller than that of the anatomical calibration points which were found by palpation over the skin. The propagation of this 2 mm uncertainty to ligament strain is presented in Table 6-2. The sensitivity of ligament strain was also evaluated at neighboring uncertainty values (0.5 mm, 5 mm, 10 mm).

Although the viscoelastic nature of the ligaments manifests by strain-rate dependant ultimate loads, failure strains are believed to be strain-rate independent (see Section 2.6.2). Therefore, kinetic effects are completely disregarded in the kinematic models, which only predict ligament strains rather than ligament loads.

The kinematic models can be compared to each other on the basis of their sensitivity to measurement uncertainties (Fastrak system accuracy, skin movement artefact, anatomical landmarks identification) and model parameter uncertainties (axes of rotation, ligament origin and insertion points) presented in Table 6-2. The kinematic models are used to complement the kinematic measurements and predict the position and orientation of the talus. Therefore, the strains of ligaments connected to the talus (ATFL, PTFL, STTL) are particularly useful in comparing the 3 kinematic models. The prediction of ligament strains with model K1 seems to lead to widely scattered values, with uncertainties of one or two orders of magnitude greater than with the other two models, and even produced cases for which the optimization algorithm did not converge. One possible explanation for this behaviour is the fact that, contrary to models K2 and K3, model K1 does not constrain any of the 6 DOF of the talus. In view of these results, ligament strains predicted by model K1 are considered unreliable. Models K2 and K3 appear to avoid these problems by constraining the talus to move around 2 axes of rotation and thus limiting its DOF to 2. Model K3 reduces the sensitivity to input data uncertainties more than model K2 does, by limiting the motion around the subtalar joint. One must keep in mind, however, that the accuracy of a model is not necessarily linked to its sensitivity to input data uncertainties. One could, for instance, consider a model that would consistently predict the same output value irrespectively of the input value. Such model would have no sensitivity to input data uncertainty but would probably be inaccurate. From a geometrical and anatomical point of view, model K3 was found to be free of inconsistencies, such as bone penetration prediction, unlike model K2, which was subject to such problems. For this reason, model K3 is considered to be the best predictor of ligament strain amongst the three kinematic models developed and used in the present study. An accurate prediction of subtalar joint rotation is not critical because none of the ligaments considered connect the talus to the calcaneus. Nevertheless, it is inferred that a more rigorous selection of subtalar joint rotation limits could improve model K3 even more.

Focussing on the K3 columns in Table 6-2, one can observe that ligaments attached to the calcaneus (CFL, TCL) are not sensitive to variations in the axes of rotation, because the strains in these ligaments are predicted from kinematic measurements only (sensors attached to the tibia-fibula and the calcaneus). However, they are more sensitive to measurement uncertainties (Fastrak accuracy, skin movement, anatomical landmarks) than ligaments attached to the talus (ATFL, PTFL, STTL), which indicates that the constrained K3 model filters out some of the measurement uncertainties by using as an input only 2 of the 6 DOF of the foot sensor. Sources of uncertainty other than the Fastrak system accuracy have moderate effects (approximately between 2 and 4%) on the prediction of ligament strains, except for the ATFL, which is very sensitive to ligament origin and insertion point uncertainty (9%). The distance between the axis of rotation of the talocrural joint and the origin or insertion points of a ligament might be considered to act as a lever arm, with zero strain for ligaments inserted exactly on the axis and increasing strains on ligaments further away from the axis. However, this distance alone does not explain the differences in sensitivities observed between the ligaments. Besides the relative position of the axis of rotation, ligament origin and ligament insertion point also have an impact on ligament strain predictions.

6.4 Model prediction of ligament strains and interpretation

Similarly to the ankle rotations, the ligament strains of the ATFL, CFL, PTFL, TCL and STTL were calculated over the 419 turn-legs included in the study (Table 4-2). The results are first presented for the average heel-side and toe-side turns. Then, the data are separated in two groups according two equipment type and the ligament strains with each type of equipment are compared.

6.4.1 Average heel-side and toe-side turns

The strains predicted by the statistical model (ATFL and CFL only) and by the three kinematic models, are presented in Figure 6-1 to Figure 6-5. In these graphs, the vertical bars stretch from the minimum to the maximum strain for the average turn-leg. The empty square over the bars indicates the mean strain value during the average turn-leg. Each graph shows the values for the back and front leg, during heel-side and toe-side turns. Some strain values are negative because the strain value was set to zero at the elongation of the ligaments for which the ankle was in neutral position. For the ATFL, CFL and PTFL, the horizontal dotted line indicates the ultimate strain of the ligament (pooled average from the literature[10,180], see Table 2-2).

As discussed, the statistical model is believed to underestimate ligament strains, which explains why the values predicted with this model are always smaller (in absolute value) than those predicted with the kinematic models. Moreover, the fact that model K1 predicts the widest ranges of ligament strains was attributed to its high sensitivity to uncertainties in input data. Strain values predicted for the CFL and TCL are similar with the 3 kinematic models because these values do not depend on the prediction of talus position and orientation by the model.

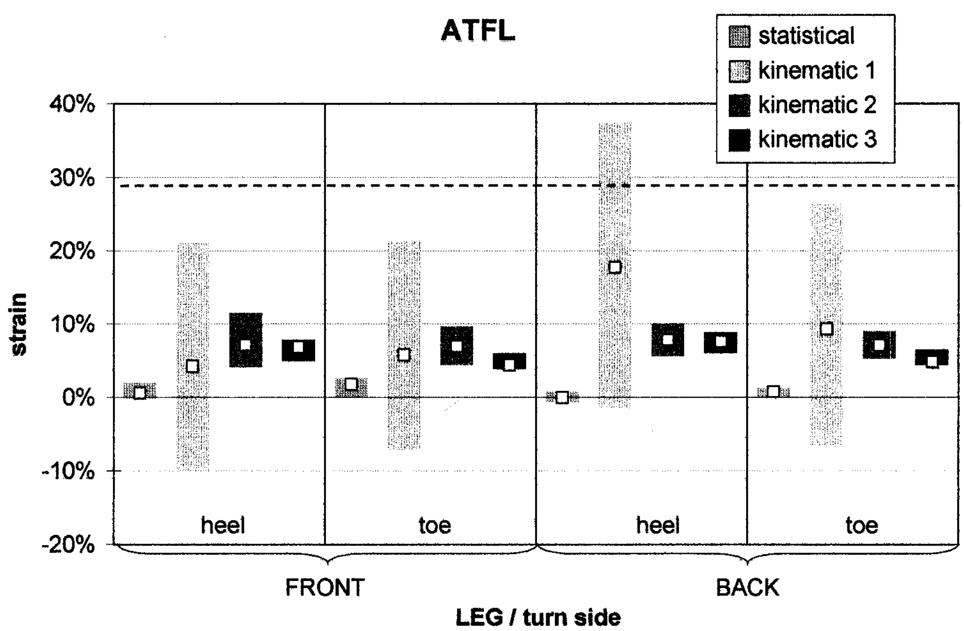

Figure 6-1: Strains in the anterior talofibular ligament (ATFL).

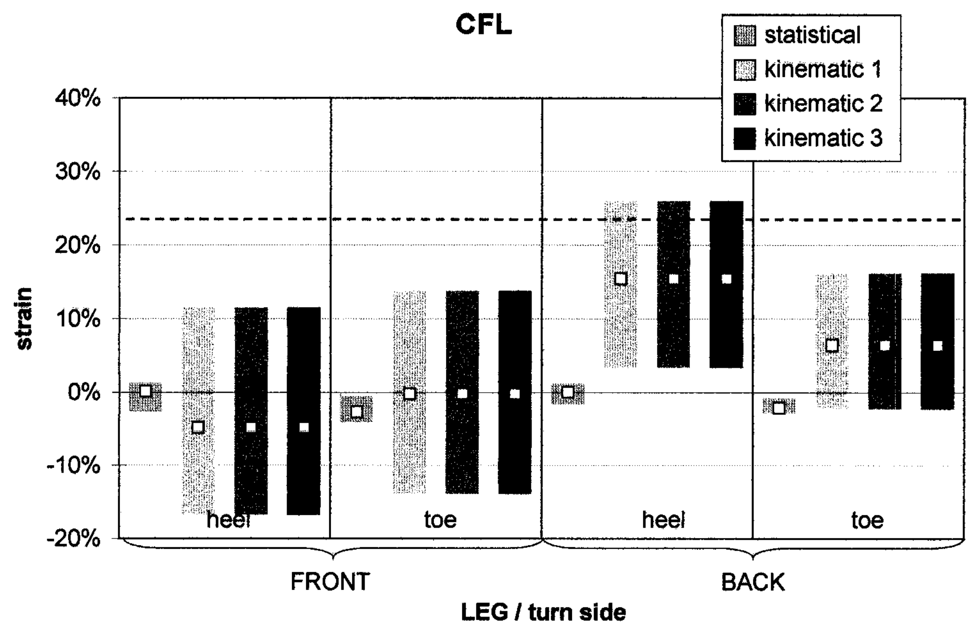

Figure 6-2: Strains in the calcaneofibular ligament (CFL).

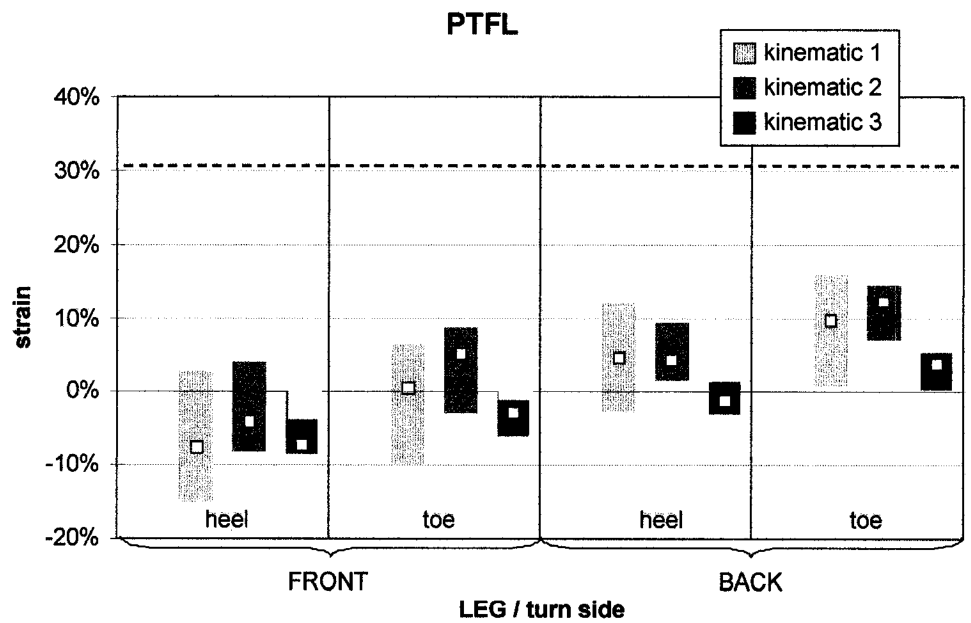

Figure 6-3: Strains in the posterior talofibular ligament (PTFL).

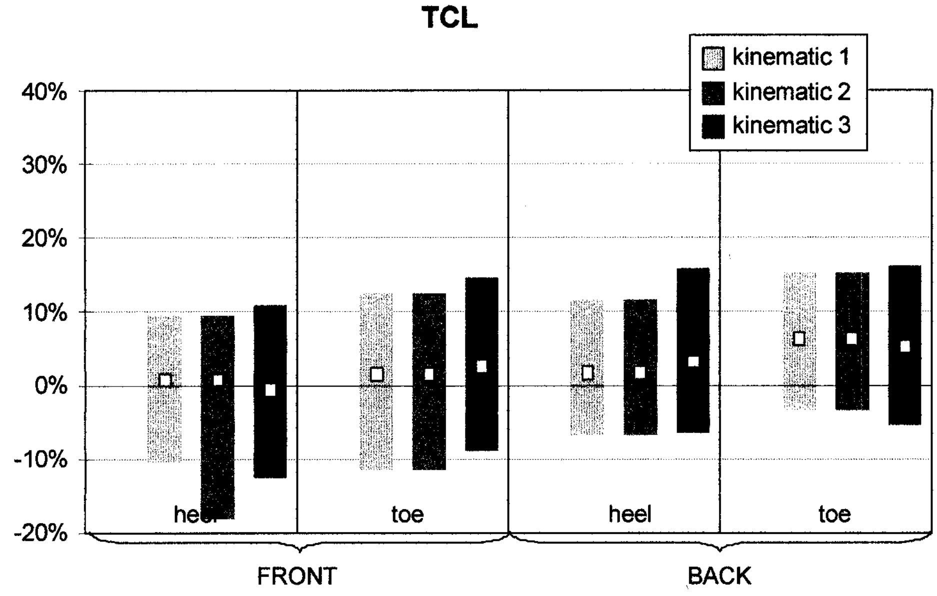

Figure 6-4: Strains in the tibiocalcaneal ligament (TCL).

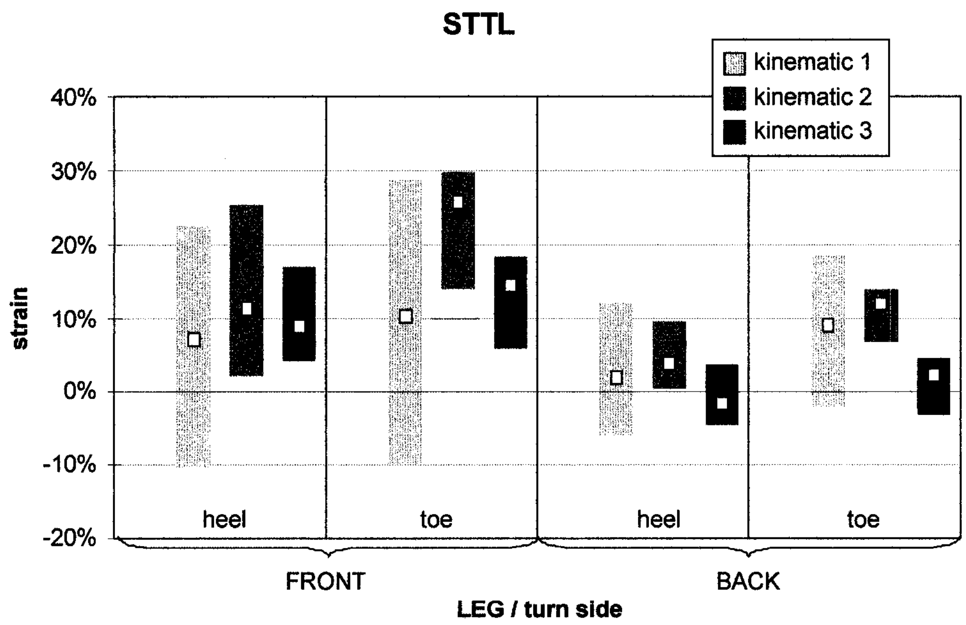

Figure 6-5: Strains in the superficial tibiotalar ligament (STTL).

More specifically, it was observed from the predictions with model K3 that the ATFL (Figure 6-1) is more stretched during heel-side turns than during toe-side turns, while the opposite behaviour was noted for the PTFL (Figure 6-3). This is probably due to the fact that dorsiflexion, which is higher during toe-side turns, stretches the ligaments connected to the posterior side of the talus like the PTFL, while plantar flexion, which only occurs during heel-side turns, would rather pull on the ligaments connected to the anterior part of the talus, like the ATFL. It was also observed that some ligaments, like the CFL and PTFL (Figure 6-2, Figure 6-3), are more stretched on the back leg, while others, like the STTL (Figure 6-5), are more stretched on the front leg. This is because, during both heel-side and toe-side turns, the AJC of the front leg is everted, stretching the ligaments on the medial side of the ankle, like the STTL. On the back leg, the AJC is slightly inverted, which would load the ligaments on the lateral side of the ankle, like the CFL and PTFL.

6.4.2 Equipment comparison

Similarly to ankle rotation values, mean and maximum ligament strain values were calculated for each turn-leg (minimum and range are meaningless for ligament strains because ligaments only fail in tension and not in compression). The values were averaged on the front leg and back leg to represent the typical heel-side turn and toe-side turn. Values obtained with each type of equipment were compared using Mann-Whitney's U-test. Table 6-3 presents a comparison of the results for the two types of equipment for values obtained with the statistical model and kinematic model #3 only.

Table 6-3: Comparison of means and maxima of ligament strains (expressed in %) with snowboard equipment A and B (average absolute deviation in parentheses).

turn side	leg	ligament	index	statistical model			kinematic model #3		
				A	B	*p*-value	A	B	*p*-value
heel	back	ATFL	mean	**0.3 (1.5)**	**-0.3 (1.0)**	**<0.01**	10.0 (12.7)	5.7 (5.9)	0.531
			max	1.1 (1.5)	0.6 (1.1)	0.043	11.6 (13.5)	6.7 (6.2)	0.531
		CFL	mean	**-0.3 (1.9)**	**0.3 (1.2)**	**<0.01**	14.4 (17.8)	16.2 (12.6)	0.985
			max	1.0 (2.0)	1.4 (1.4)	0.171	25.9 (20.7)	26.1 (14.3)	0.531
		PTFL	mean				-2.6 (7.7)	-0.5 (6.4)	0.823
			max				1.1 (7.8)	1.4 (6.7)	0.115
		TCL	mean				**-1.7 (4.4)**	**7.1 (8.4)**	**<0.01**
			max				**4.0 (4.8)**	**24.8 (9.4)**	**<0.01**
		STTL	mean				-1.7 (11.0)	-1.4 (7.9)	0.523
			max				3.8 (10.9)	3.4 (6.9)	0.906
	front	ATFL	mean	0.9 (1.1)	0.3 (0.5)	0.107	9.3 (12.0)	4.5 (4.8)	0.597
			max	**2.5 (0.9)**	**1.4 (0.4)**	**<0.01**	10.5 (12.8)	5.3 (5.1)	0.637
		CFL	mean	-0.3 (2.3)	0.5 (1.2)	0.167	-3.3 (14.9)	-6.2 (10.3)	0.540
			max	1.0 (2.3)	1.6 (1.4)	0.230	9.6 (16.6)	13.3 (10.8)	0.536
		PTFL	mean				-8.7 (9.0)	-6.0 (2.8)	0.214
			max				-4.4 (9.1)	-3.6 (2.9)	0.238
		TCL	mean				-1.3 (12.8)	0.3 (10.0)	0.647
			max				7.7 (16.8)	13.9 (14.0)	0.113
		STTL	mean				12.3 (22.4)	5.7 (14.8)	0.750
			max				19.7 (25.1)	14.3 (16.5)	0.667
toe	back	ATFL	mean	**1.5 (1.6)**	**0.2 (1.2)**	**<0.01**	5.3 (10.6)	4.5 (4.8)	0.706
			max	**2.0 (1.5)**	**0.7 (1.1)**	**<0.01**	7.6 (11.7)	5.6 (5.2)	0.835
		CFL	mean	**-3.3 (2.1)**	**-1.2 (1.3)**	**<0.01**	-0.1 (19.0)	11.7 (9.4)	0.023
			max	**-1.6 (2.2)**	**-0.1 (1.4)**	**<0.01**	12.3 (20.7)	19.4 (10.2)	0.503
		PTFL	mean				3.6 (9.2)	3.9 (8.1)	0.152
			max				5.6 (9.2)	5.1 (8.1)	0.146
		TCL	mean				**-9.2 (4.9)**	**17.1 (9.3)**	**<0.01**
			max				**0.9 (4.8)**	**28.3 (11.9)**	**<0.01**
		STTL	mean				3.4 (10.8)	1.6 (6.6)	0.545
			max				5.5 (10.8)	3.8 (6.8)	0.537
	front	ATFL	mean	2.0 (1.2)	1.5 (0.5)	0.086	6.6 (9.8)	2.4 (3.3)	0.353
			max	**3.1 (0.8)**	**2.2 (0.3)**	**<0.01**	8.5 (11.3)	3.7 (4.1)	0.410
		CFL	mean	-3.4 (2.1)	-2.1 (0.8)	0.028	-3.6 (14.9)	2.9 (10.5)	0.117
			max	-0.7 (2.8)	-0.3 (1.3)	0.697	12.2 (15.9)	15.2 (8.9)	0.764
		PTFL	mean				-3.2 (9.1)	-2.7 (3.3)	0.372
			max				-1.1 (8.8)	-1.4 (3.3)	0.528
		TCL	mean				-0.2 (13.6)	5.4 (14.9)	0.152
			max				11.0 (18.8)	17.6 (16.0)	0.167
		STTL	mean				17.0 (23.4)	12.4 (15.9)	0.666
			max				20.5 (25.1)	16.4 (16.5)	0.656

The statistical model predicted smaller maximum values for the ATFL strain with equipment B than with equipment A. These differences were always larger than the 0.8% sensitivity of the ATFL strain prediction (Table 6-2), except for the back leg during heel turns. The statistical model also predicted higher values for the CFL with equipment B than with equipment A. However, no biomechanical significance can be given to these differences, because they were smaller than the sensitivity of CFL strain (1.4%, Table 6-2) for the back leg during heel turns, and strain values were negative for all other statistically significant differences. These observations point out that the ATFL would be more protected by step-in boots and bindings than by soft boots with strap bindings.

Model K3 did not predict ATFL and CFL strains that were significantly different between the two types of equipment. The only significant difference is in the prediction of TCL strain, which is larger on the back leg with equipment B than with equipment A.

These differences in ligament strain are difficult to explain by the differences observed on the rotations of the AJC, because ligaments are often stretched by a combination of rotations. For instance, the CFL strain would have been expected to be different between the two types of snowboard equipment on the front leg, where differences were observed in EV/IV, rather than on the back leg, where no difference was observed in the level of EV/IV. A possible explanation is that small differences on other rotations added up to cause a significant difference in CFL strain. The same applies to other ligaments as well.

One peculiar observation about these data is that the only difference that could be detected by the kinematic model was on a ligament that is not connected to the talus. This might indicate that the model is not sensitive enough and filters out too much of the experimental information. The idea behind the kinematic model is to complement the experimental data with *a priori* knowledge on the mechanical behaviour of the talucrural and subtalar joints, in order to predict the position and orientation of the talus, which is very difficult to measure experimentally with external markers. However, because the kinematic model only has 2 DOF (one per joint), it can only keep 2 out of the 6 DOF measured. It is possible that the *a priori* information is too constraining or not sufficiently personalized. This might make model K3 discard experimental data that are not consistent with the movements allowed by the model. One possible way to improve the model would be to use some of the experimental data to personalize the model. For instance, a functional determination of the axes of rotation, as described by van den Bogert[194], could be used to adjust the position and orientation of the axes of rotation. The limit of the subtalar joint rotation could also be adjusted to each individual, based on the experimental data.

7 Conclusions and Recommendations for Further Research

The present research addressed the problem of ankle injuries in snowboarding by investigating ankle kinematics during normal snowboarding manoeuvres.

The first objective consisted of documenting experimentally the kinematics of the lower extremities in snowboarding. Accurately measuring the movement of the ankle joint complex, which is completely covered by structural equipment like a snowboard boot, was a challenging task. Moreover, the experiment was done outside the laboratory in weather conditions less than ideal when working with battery-operated electronic equipment. Despite the difficulties, the original experimental method developed for this study allowed to successfully record the kinematics of the ankle joint complex of five snowboarders. The experimental results, expressed in anatomically relevant joint rotations, demonstrate the highly asymmetric nature of snowboarding movements. Notably, during both heel-side and toe-side turns, the front foot was slightly everted and more dorsiflexed than the back foot by 10° to 12°. This may suggest that bindings should be asymmetrically adjusted not only in axial rotation of the feet but also in highback minimum flexion.

The second objective was to use the experimentally measured kinematics of the ankle to predict the strains in some of its most often injured ligaments. Two predictive models were developed. A statistical model was created based on published experimental *in vitro* ligament strains (ATFL and CFL) measured at various rotations of the ankle joint complex of five cadaver leg specimens. For each combination of 3 orthogonal rotations of the snowboarder's ankle joint complex, the ligament strains were predicted using interpolation and extrapolation of the published data points. The statistical model predicted small strain values for the ATFL and the CFL (less than 5%), which are believed to be a 60% underestimation of actual strains.

Alternatively, a 2-DOF kinematic model was constructed based on the CT-scan reconstruction of a cadaver leg specimen. The geometry was personalized to each snowboarder using percutaneously measured anatomical landmarks. The model can predict the strain in 5 ligaments of the ankle based on the position and orientation of the three links of this kinematic chain (calcaneus, talus and tibia-fibula). The position and orientation of the first and last links were obtained from the experimental measurements on snowboarders. The position and orientation of the middle link (talus) were solved using three methods based on numerical optimization. The third approach, which uses constrained optimization of forward kinematics to solve the inverse kinematics problem, was proven to be the least sensitive to uncertainties in the input values. It predicted more strain in the ATFL during heel-side than toe-side turns, and the opposite behaviour for the PTFL, presumably because of the level of dorsiflexion during those movements. It also predicted higher strains in the medial ligaments like the STTL of the front leg, and higher strains in the lateral ligaments like the CFL and PTFL of the back leg, apparently because of the higher level of eversion of the front leg than of the back leg.

The third objective consisted of comparing the effects of different designs of snowboard boots and bindings on ankle kinematics and ligament strains. Several parameters (range of DF), particularly on the front leg (mean and maximum DF, range and maximum EV, range of ER), indicate that step-in boots and bindings allow significantly less rotation of the ankle joint complex than soft boots and strap bindings. Considering that the ATFL, the most often sprained ligament of the ankle, is loaded by IR, IV and PF movements, it cannot be concluded from the experimental data alone that step-in boots better protect the ATFL against overstretching. However, the statistical model predicted significantly smaller ATFL strains with the step-in boots and bindings than with the soft boots and strap bindings, pointing out that the ATFL would be better protected with step-in boots and bindings. The kinematic model was not sensitive enough to detect those differences between the two types of equipment on the ligaments that are connected to the talus, probably because it filters out 4 of the 6 DOF in the experimental data when solving the inverse kinematic problem. However, it detected significantly higher strains on the TCL with the step-in boots and bindings than with the soft boots and strap bindings, a difference that is difficult to explain from differences in rotations of the ankle joint complex.

Based on the experience of this study, several recommendations are formulated to suggest paths for future work. Future experimental recordings of snowboarder's movement should be done on steeper hills so that higher ranges of joint rotations are recorded. This could amplify the difference between two types of snowboarding equipment.

The statistical and kinematic models are both promising and neither approach should be discarded before pursuing their development further. The statistical model uses published experimental measurements of ligament strains that were done over a range of motion that goes from 40° of plantar flexion to 10° of dorsiflexion, which is not representative of the rotations of the ankle joint complex observed in snowboarding (15° of plantar flexion to 35° of dorsiflexion). Therefore, extrapolation was used for predicting the snowboarder's ligament strains almost half of the time. The statistical model would thus greatly benefit from using new experimental measurements of ligament strains done over the full range of motion of the ankle joint complex.

The kinematic model approach is promising because it can be personalized to the morphology of each snowboarder. However, the results have shown that when formulated to account for all redundant DOF (model K1), the model is too sensitive to measurement uncertainties. Also, when formulated to filter out the redundant DOF (models K2 and K3), the model is not sensitive enough to detect differences in the two types of equipment, even though those differences were statistically significant in the input kinematic data. This is probably because the axes of rotation of the model are too different from the axes of rotation of the snowboarder. Therefore, it is believed that a functional determination of the axes of rotations from kinematic measurements of each snowboarder in the laboratory, as described by van den Bogert[194], would be an interesting non-invasive approach to explore in order to improve the performance of the kinematic model. How the origin and insertion points of the ligaments are related to the position and orientation of the axes of rotations still needs to be taken into account to get a consistent kinematic model. The kinematic approach is also based on the hypothesis that the ultimate strain of ligaments is not sensitive to strain rate. This hypothesis still needs to be tested on human ankle ligaments. If the hypothesis is proven wrong, then a more refined viscoelastic constitutive model could be used to represent the behaviour of ligaments.

Although the overall scope of the project was the understanding of ankle injuries in snowboarding, the present work focused on normal snowboarding manoeuvres because it is not ethically acceptable to have humans participate in experiments involving injuries. Another experimental approach could be to have an anthropometric dummy mounted on a snowboard make a fall or hit an obstacle to simulate an ankle injury. The design of an appropriate impact test is complicated by the fact that little information is currently available on the type of movement that initiates ankle injuries in snowboarding, because of the difficulty to observe ankle injuries as they occur.

Therefore, in order to fully understand the mechanisms responsible for ankle injuries in snowboarding, parallel work is needed with several approaches: 1) epidemiological studies on snowboarding injuries; 2) simulations with mechanical models of the ankle; 3) impact tests with anthropometric dummies; and 4) ankle loading measurement in normal snowboarding. The present study has established an innovative experimental methodology coupled with predictive models for the indirect measurement of ligament strain in normal snowboarding.

References

1 National Sporting Goods Association. 2001 Sports Participation Study. http://www.snowlink.com/newsresearch/stats/stats-basic.shtml.

2 1996 Snowboarding business resort survey. Transworld Snowboarding 1996 :1.

3 Abu-Laban RB. Snowboarding injuries: an analysis and comparison with alpine skiing injuries. Canadian Medical Association Journal 1991;145(9):1097-103.

4 Ahl T, Dalen N, Lundberg A, Selvik G. Mobility of the ankle mortise. A roentgen stereophotogrammetric analysis. Acta Orthop Scand 1987; 58:401-2.

5 Alexander EJ, Andriacchi TP. Correcting for deformation in skin-based marker systems. J Biomech 2001;34(3):355-61.

6 Allard P, Thiry PS, Duhaime M, Geoffroy G. Kinematics of the foot. Canadian Journal of Neurological Sciences 1982;9(2):119-25.

7 Allinger TL, Engsberg JR. A method to determine the range of motion of the ankle joint complex, *in vivo*. Journal of Biomechanics 1993;26(1):69-76.

8 Angeloni C, Cappozzo A, Catani F, Leardini A. Quantification of relative displacement of skin- and plate-mounted markers with respect to bones. J Biomech 1993;26:864.

9 Aström M, Arvidson T. Alignment and joint motion in the normal foot. J Orthop Sports Phys Ther 1995;22(5):216-22.

10 Attarian DE, McCrackin HJ, DeVito DP, McElhaney JH, Garrett WE. Biomechanical characteristics of human ankle ligaments. Foot Ankle 1985;6(2):54-8.

11 Azangwe G, Mathias KJ, Marshall D. Preliminary comparison of the rupture of human and rabbit anterior cruciate ligaments. Clin Biomech (Bristol, Avon) 2001;16(10):913-7.

12 Bahniuk E, Schneider R, Tompkin E. The effect of ankle motion on ski binding release tests using an anthropometric dummy. In: Johnson RJ, Mote CDJ, Binet M-H, eds. Skiing Trauma and Safety: ASTM, 1989:210-221.

13 Bahniuk E, Strunc J. The use of an anthropometric dummy for testing a new ski binding-boot system. In: Mote CDJ, Johnson RJ, eds. Skiing Trauma and Safety: ASTM, 1987:225-232.

14 Bally A, Taverney O. Loads transmitted in the practice of snowboarding. In: Mote CD, Johnson RJ, Hauser E, *et al.*, eds. Skiing Trauma and Safety: ASTM, 1996:110-113.

15 Baud PM, Bourgeois FP. Releasable binding assembly. United States: Salomon S.A., 1991 (patent).

16 Berghold F, Seidl AM. Snowboarding accidents in the Alps. Assessment of risk, analysis of the accidents and injury profile. Schweizerische Zeitschrift fur Sportmedizin 1991;39(1):13-20.

17 Biasca N, Biattaglia H, Simmens HP, *et al.* An overview of snow-boarding injuries. Unfallchirurg 1995;98(1):33-39.

18 Bjornstig J, Bjornstig U. Snow-boarding injuries can be prevented. Nordisk Medicin 1996;111(1):7-9.

19 Bladin C, Giddings P, Robinson M. Australian snowboard injury data base study. A four-year prospective study. American Journal of Sports Medicine 1993;21(5):701-4.

20 Boldrino C, Furian G. Risk factors in skiing and snowboarding in Austria. In: Johnson RJ, editor. Skiing Trauma and Safety; 1999: ASTM; 1999. p. 166-174.

21 Boruta PM, Bishop JO, Braly WG, Tullos HS. Acute lateral ankle ligament injuries: a literature review. Foot Ankle 1990; 11:107-113.

22 Bottlang M, Marsh JL, Brown TD. Articulated external fixation of the ankle: minimizing motion resistance by accurate axis alignment. J Biomech 1999;32(1):63-70.

23 Bryson S. Measurement and calibration of static distortion of position data from 3D trackers. In: SPIE Conference on Stereoscopic Displays and Applications III; 1992; 1992. p. 244-255.

24 Buquet T. Releasable binding for ski, monoski, snowboard or the like. United States: Look Fixations SA, 1999 (patent).

25 Buzzi R, Todescan G, Brenner E, Segoni F, Indester A, Aglietti P. Reconstruction of the lateral ligaments of the ankle: an anatomic study with evaluation of isometry. J Sports Traumatol Rel Res 1993;15:55-74.

26 Cadman R, Macnab AJ. Age and gender: two epidemiological ractors in skiing and snowboarding injury. In: Mote CDJ, Johnson RJ, Hauser W, Schaff PS, editors. Skiing Trauma and Safety; 1996: ASTM; 1996. p. 58-65.

27 Caldwell RT, Berbaum KS, Borah J. Correcting errors in eye-position data arising from the distortion of magnetic fields by display devices. Behav Res Methods Instrum Comput 2000;32(4):572-8.

28 Calle SC, Evans JT. Snowboarding trauma. Journal of Pediatric Surgery 1995;30(6):791-4.

29 Cappello A, Cappozzo A, Della Croce U, Leardini A. Bone position and orientation reconstruction using external markers. In: Allard P, Cappozzo A, Lundberg A, Vaughan C, editors. Three-dimensional Analysis of Human Locomotion: John Wiley & Sons; 1997. p. 145-171.

30 Cappello A, Cappozzo A, La Palombara PF, Lucchetti L, Leardini A. Multiple anatomical landmark calibration for optimal bone pose estimation. Human Movement Science 1997; 16:259-274.

31 Cappozzo A, Cappello A, Della Croce U, Pensalfini F. Surface-marker cluster design criteria for 3-D bone movement reconstruction. IEEE Trans Biomed Eng 1997;44(12):1165-74.

32 Cappozzo A, Catani F, Leardini A, Benedetti MG, Croce UD. Position and orientation in space of bones during movement: experimental artefacts. Clin Biomech (Bristol, Avon) 1996;11(2):90-100.

33 Cappozzo A, Della Croce U, Lucchetti L. Gait data: terminology and definitions. In: Allard P, Cappozzo A, Lundberg A, Vaughan C, editors. Three-dimensional Analysis of Human Locomotion. West Sussex, England: John Wiley & Sons; 1997. p. 129-146.

34 Castaing J, Delplace J, Le Roy JD. "La cheville" in *Anatomie fonctionnelle de l'appareil locomoteur*. Editions Vigot, Europrinte, Portugal 1960.

35 Chen J, Siegler S, Schneck CD. The three-dimensional kinematics and flexibility characteristics of the human ankle and subtalar joint--Part II: Flexibility characteristics. Journal of Biomechanical Engineering 1988; 110:374-85.

36 Chen WP, Tang FT, Ju CW. Stress distribution of the foot during mid-stance to push-off in barefoot gait: a 3-D finite element analysis. Clin Biomech (Bristol, Avon) 2001;16(7):614-20.

37 Cheriet F, Delorme S, Labelle H, Aubin CÉ, De Guise JA, Dansereau J. Reconstruction 3D per-opératoire de la colonne vertébrale scoliotique à partir de radiographies biplanaires. Annales de Chirurgie 1999; 53:808-815.

38 Cheriet F, Meunier J. Self-calibration of a biplane X-ray imaging system for an optimal three dimensional reconstruction. Comput Med Imaging Graph 1999;23(3):133-141.

39 Choi J. Acute conditions incidence and associated disability. Vital. Health Statistics 1978; 10:10.

40 Chow TK, Corbett SW, Farstad DJ. Spectrum of injuries from snowboarding. J Trauma 1996;41(2):321-5.

41 Colville MR, Marder RA, Boyle JJ, Zarins B. Strain measurement in lateral ankle ligaments. Am J Sports Med 1990;18(2):196-200.

42 Corke PI. A robotics toolbox for MATLAB. IEEE Robotics and Automation Magazine 1996;3(1):24-32.

43 Cornwall MW, McPoil TG. Three-dimensional movement of the foot during the stance phase of walking. J Am Podiatr Med Assoc 1999;89(2):56-66.

44 Crisco JJ, Moore DC, McGovern RD. Strain-rate sensitivity of the rabbit MCL diminishes at traumatic loading rates. J Biomech 2002;35(10):1379-85.

45 Davidson TM, Laliotis AT. Snowboarding injuries, a four-year study with comparison with alpine ski injuries. Western Journal of Medicine 1996;164(3):231-7.

46 Day JS, Dumas GA, Murdoch DJ. Evaluation of a long-range transmitter for use with a magnetic tracking device in motion analysis. J Biomech 1998;31(10):957-61.

47 Day JS, Murdoch DJ, Dumas GA. Calibration of position and angular data from a magnetic tracking device. J Biomech 2000; 33:1039-45.

48 della Croce U, Cappozzo A, Kerrigan DC. Pelvis and lower limb anatomical landmark calibration precision and its propagation to bone geometry and joint angles. Med Biol Eng Comput 1999;37(2):155-61.

49 Delorme S, Petit Y, de Guise JA, Aubin CE, Labelle H, Landry C, *et al.* Three-dimensional modelling and rendering of the human skeletal trunk from 2D radiographic images. In: Second International Conference on 3-D Digital Imaging and Modeling; 1999; Ottawa, ON, Canada; 1999. p. 497-505.

50 Delorme S, Petit Y, de Guise JA, Aubin CE, Labelle H, Dansereau J. Assessment of the 3D reconstruction and high-resolution geometrical modelling of the human skeletal trunk from 2D radiographic images. IEEE Trans Biomed Eng (in press).

51 Delp S, Loan J, Hoy M, Zajac F, Topp E, Rosen J. An interactive graphics-based model of the lower extremity to study orthopaedic surgical procedures. IEEE Transactions on Biomedical Engineering 1990;37(8):757-67.

52 Dempster WT. The anthropometry of manual work space for the seated subjects. Am J Phys Anthrop 1959;17:289-317.

53 Denavit J, Hartenberg RS. A kinematic notation for lower-pair mechanisms based on matrices. Journal of Applied Mechanics 1955:215-221.

54 Dennis D. Releasable binding system for snowboarding. Unites States: Look Alpine Products, Inc., 1991 (patent).

55 Dinko S. Snowboard binding with release mechanism. Canada: 1997 (patent).

56 Dorius LK, Hull ML. Dynamic simulation of the leg in torsion. Journal of Biomechanics 1984; 17:1-9.

57 Downing JW, Klein SJ, D'Amico JC. The axis of motion of the rearfoot complex. J Am Podiatry Assoc 1978;68(7):484-99.

58 Dul J, Johnson GE. A kinematic model of the human ankle. Journal of Biomedical Engineering 1985;7(2):137-43.

59 Elftman H. The orientation of the joints of the lower extremity. Bull Hosp Joint Dis 1945;6(139-145).

60 Elftman H, Manter J. The evolution of the human foot, with especial reference to the joints. J Anat 1935;70:56.

61 Engsberg JR, Andrews JG. Kinematic analysis of the talocalcaneal/talocrural joint during running support. Med Sci Sports Exerc 1987;19(3):275-84.

62 Engsberg JR, Grimston SK, Wackwitz JH. Predicting talocalcaneal joint orientations from talocalcaneal/talocrural joint orientations. J Orthop Res 1988;6(5):749-57.

63 Estes M, Wang E, Hull ML. Analysis of ankle deflection during a forward fall in snowboarding. Journal of Biomechanical Engineering 1999;121(2):243-8.

64 Fauvet. Releasable binding assembly. United States: Salomon S.A., 1991 (patent).

65 Friedrichs E, van Bergen B. Sensor plates designed for measuring forces between ski and binding-- A developmental summary. In: al. Me, ed. Skiing and Science. London: E & FN Spon, 1997:180-187.

66 Fuller J, Liu L-J, Murphy MC, Mann RW. A comparison of lower-extremity skeletal kinematics measured using skin- and pin-mounted markers. Human Movement Science 1997;16:219-242.

67 Funk JR, Hall GW, Crandall JR, Pilkey WD. Linear and quasi-linear viscoelastic characterization of ankle ligaments. J Biomech Eng 2000;122(1):15-22.

68 Ganong RB, Heneveld EH, Beranek SR, Fry P. Snowboarding injuries. A report on 415 patients. The Physician and Sportsmedicine 1992;20(12):114-122.

69 Garrick JG. The frequency of injury, mechanism of injury, and epidemiology of ankle sprains. Am J Sports Med 1977; 5(6):241-242.

70 Gentili A, Masih S, Yao L, Seeger LL. Pictorial review: foot axes and angles. Br J Radiol 1996;69(826):968-74.

71 Goss BR, Botting CA, Knight SW. Releasable snowboard binding. United States: 1997:

72 Gray H. Anatomy of the Human Body. 20th ed. New York: Bartleby.com; 2000.

73 Greenwald RM, Swanson SC, McDonald TR. A comparison of the effect of ski sidecut on three-dimensional knee joint kinematics during a ski run. Sportverletzung Sportschaden 1997;11(4):129-33.

74 Grimston SK, Nigg BM, Hanley DA, Engsberg JR. Differences in ankle joint complex range of motion as a function of age. Foot & Ankle 1993;14(4):215-22.

75 Hackam DJ, Kreller M, Pearl RH. Snow-related recreational injuries in children: assessment of morbidity and management strategies. Journal of Pediatric Surgery 1999;34(1):65-8; discussion 69.

76 Hagel BE, Meeuwisse WH, Mohtadi NG, Fick GH. Skiing and snowboarding injuries in the children and adolescents of Southern Alberta. Clin J Sport Med 1999;9(1):9-17.

77 Hancock S, Lamontagne M, Stothart JP, Sveistrup H. The influence of three hockey skate boots on the range of motion, elastic moment and stiffness of the human ankle joint complex. In: Herzog W, Jinha A, eds. International Society of Biomechanics XVIIth Congress. Calgary: Publisher of the Proceedings ISB99, 1999:497.

78 Hicks JH. The mechanics of the foot--I. The joints. J Anat 1953;87:345-357.

79 Hill KJ. Releasable binding for snowboards. United States: 1988 (patent).

80 Hintermann B, Nigg BM. *In vitro* kinematics of the axially loaded ankle complex in response to dorsiflexion and plantarflexion. Foot & Ankle International 1995;16(8):514-8.

81 Holden JP, Orsini JA, Lohmann Siegel K, Kepple TM, Gerber LH, Stanhope SJ. Surface movement errors in shank kinematics and knee kinetics during gait. Gait & Posture 1997;5:217-227.

82 Holzach P, Bruesch M, Matter P. Epidemiology of internal knee injuries in alpine skiing. Helvetica Chirurgica Acta 1994;60:531-537.

83 Hull ML, Mote CD, Jr. Leg loading in snow skiing: computer analyses. Journal of Biomechanics 1980;13(6):481-91.

84 Ikits M, Brederson JD, Hansen CD, Hollerbach JM. An improved calibration framework for electromagnetic tracking devices. In: Proc IEEE VR; 2001. p. 63-70.

85 Industry Statistics Sheet. Englewood, CO: National Snowboard Inc, 1990.

86 Inman VT. The Joints of the Ankle. Baltimore: Williams and Wilkins; 1976.

87 Isman RE, Inman VT. Anthropometric studies of the human foot and ankle. Bull Prosth Res 1969;11:97-112.

88 Janes PC, Abbott PJ. The Colorado snowboarding injury study: eight year results. In: Johnson RJ, editor. Skiing Trauma and Safety; 1999: ASTM; 1999. p. 141-149.

89 Janes PC, Fincken GT. Snowboarding injuries. In: Johnson RJ, Mote CDJ, Zelcer J, eds. Skiing Trauma and Safety: ASTM, 1993:255-261.

90 Jochheim A, Gerke M, Bischoff A. Modeling and simulation of kinematic systems. Report. Hagen, Germany: University of Hagen; 1999 August 27.

91 Karrholm J, Hansson LI, Selvik G. Mobility of the lateral malleolus. A roentgen stereophotogrammetric analysis. Acta Orthop Scand 1985; 56:479-83.

92 Kearney RE, Hunter IW. Dynamics of human ankle stiffness: variation with displacement amplitude. Journal of Biomechanics 1982; 15:753-6.

93 Kearney RE, Stein RB, Parameswaran L. Identification of intrinsic and reflex contributions to human ankle stiffness dynamics. IEEE Transactions on Biomedical Engineering 1997; 44:493-504.

94 Kincheloe CV. Releasable snowboard binding. United States: 1991 (patent).

95 Kindratenko V. Calibration of electromagnetic tracking devices. Virtual Reality: Research, Development, and Applications 1999;4:139-150.

96 Kindratenko V. Evaluation of rotation correction techniques for electromagnetic position tracking systems. In: Virtual Environments 2000: Proceedings of the Eurographics Workshop. Berlin: Springer-Verlag; 2000. p. 13-22.

97 Kirkpatrick DP, Hunter RE, Janes PC, Mastrangelo J, Nicholas RA. The snowboarder's foot and ankle. Am J Sports Med 1998;26(2):271-7.

98 Knünz B, Nachbauer W, Schindelwig K, Brunner F. Forces at the boot sole during skidded and carved snowboard turns. In: Herzog W, Jinha A, eds. International Society of Biomechanics XVIIth Congress. Calgary: Publisher of the Proceedings ISB99, 1999:912.

99 Kobayashi K, Gransberg L, Knutsson E, Nolén P. A new system fo three-dimensional gait recording using electromagnetic tracking. Gait & Posture 1997;6:63-75.

100 Konradsen L, Voigt M. Inversion injury biomechanics in functional ankle instability: a cadaver study of simulated gait. Scand J Med Sci Sports 2002;12(6):329-36.

101 Kuo CY, Louie JK, Mote CD, Jr. Field measurements in snow skiing injury research. Journal of Biomechanics 1983;16(8):609-24.

102 Lafontaine D, Lamontagne M, Dupuis D, Diallo B. Analysis of the distribution of pressure under the feet of elite alpine ski instructors. 16th International Symposium on Biomechanics in Sports. Konstanz, Germany, 1998.

103 Lafontaine D, Lamontagne M, Dupuis D, Diallo B. Plantar pressure distribution measured during alpine ski turns. VIth EMED Scientific Meeting. Brisbane, Australia., 1998.

104 Lafontaine D, Lamontagne M. Plantar pressure and porce values for alpine ski instructors performing a variety of turns on groomed terrain. In: Herzog W, Jinha A, editors. Internation Society of Biomechanics XVIIth Congress; 1999; Calgary: Publishers of the Proceedings ISB99; 1999. p. 916.

105 Lafontaine D, Lamontagne M. Timing and values of peaks of plantar pressure and force for alpine ski instructors performing a variety of turns on groomed terrain. Fourth ISB Footwear Symposium. Canmore, Canada, 1999.

106 LaMont JG. Functional anatomy of the lower limb. Clin Plast Surg 1986;13(4):571-9.

107 Lamont M. Ski field injuries: the snowboarders. In: Mote CDJ, Johnson R, Hauser W, Schaff PS, eds. Skiing Trauma and Safety: ASTM, 1996:82-86.

108 Leardini A, O'Connor JJ, Catani F, Giannini S. A geometric model of the human ankle joint. Journal of Biomechanics 1999;32(6):585-91.

109 Leardini A, O'Connor JJ, Catani F, Giannini S. Kinematics of the human ankle complex in passive flexion; a single degree of freedom system. Journal of Biomechanics 1999; 32:111-8.

110 Leardini A, Stagni R, O'Connor JJ. Mobility of the subtalar joint in the intact ankle complex. J Biomech 2001;34(6):805-9.

111 Ledoux WR, Camacho DLA, Ching RP, Sangeorzan BJ. A finite element model of the foot and ankle: validation of quiet stance. In: Fourth World Congress of Biomechanics; 2002; Calgary; 2002.

112 Lee CW, Mote CD. Identification of the human lower extremity in torsion: application to snow ski injuries. U.C. Berkeley: Department of Mechanical Engineering, 1980.

113 Lewis G, Shaw KM. Tensile properties of human tendo Achillis: effect of donor age and strain rate. J Foot Ankle Surg 1997;36(6):435-45.

114 Livingston MA, State A. Magnetic tracker calibration for improved augmented reality registration. Presence 1997;6:532-546.

115 Louie JK, Kuo CY, Gutierrez MD, Mote CD, Jr. Surface EMG and torsion measurements during snow skiing: laboratory and field tests. Journal of Biomechanics 1984;17(10):713-24.

116 Lucchetti L, Cappozzo A, Cappello A, Della Croce U. Skin movement artefact assessment and compensation in the estimation of knee-joint kinematics. J Biomech 1998;31(11):977-84.

117 Lundberg A, Goldie I, Kalin B, Selvik G. Kinematics of the ankle/foot complex: plantarflexion and dorsiflexion. Foot & Ankle 1989;9(4):194-200.

118 Lundberg A, Svensson OK, Bylund C, Goldie I, Selvik G. Kinematics of the ankle/foot complex--Part 2: Pronation and supination. Foot & Ankle 1989;9(5):248-53.

119 Lundberg A, Svensson OK, Bylund C, Selvik G. Kinematics of the ankle/foot complex--Part 3: Influence of leg rotation. Foot & Ankle 1989;9(6):304-9.

120 Lundberg A, Svensson OK, Nemeth G, Selvik G. The axis of rotation of the ankle joint. J Bone Joint Surg Br 1989;71(1):94-9.

121 MacGregor D, Hull ML, Dorius LK. A microcomputer controlled snow ski binding system--I. Instrumentation and field evaluation. Journal of Biomechanics 1985;18(4):255-65.

122 MacGregor D, Hull ML. A microcomputer controlled snow ski binding system--II. Release decision theories. Journal of Biomechanics 1985;18(4):267-75.

123 Manal K, McClay Davis I, Galinat B, Stanhope S. The accuracy of estimating proximal tibial translation during natural cadence walking: bone vs. skin mounted targets. Clin Biomech (Bristol, Avon) 2003;18(2):126-31.

124 Manal K, McClay I, Stanhope S, Richards J, Galinat B. Comparison of surface mounted markers and attachment methods in estimating tibial rotations during walking: an *in vivo* study. Gait Posture 2000;11(1):38-45.

125 Mann HB, Whitney DR. On a test of whether one of two random variables is stochastically larger than the other. The Annals of Mathematical Statistics1947; 18:50-60.

126 Manter JT. Movements of the subtalar and transverse tarsal joints. Anat Rec 1941;80:397-410.

127 Martini FH, Timmons MJ, McKinley MP. Human Anatomy. Third Edition ed. Upper Saddle River, New Jersey: Prentice Hall; 2000.

128 Maslen BA, Ackland TR. Radiographic study of skin displacement errors in the foot and ankle during standing. Clin Biomech (Bristol, Avon) 1994;9(5):291-296.

129 Maxwell SM, Hull ML. Measurement of strength and loading variables on the knee during Alpine skiing. Journal of Biomechanics 1989;22(6-7):609-24.

130 McLennan JC, McLennan JG. Snowboarding: What injuries to expect in this rapidly growing sport. J Musculoskeletal Med 1991;8(11):75-89.

131 Medoff H, Pierce J, Pope M, Johnson R, Mote CD. On-slope testing of an instrumented alpine ski boot. In: Johnson RJ, ed. Skiing Trauma and Safety: Fifth International Symposium. A symposium sponsored by ASTM Committee F-27 on Snow Skiing and by the International Society for Skiing Safety. Philadelphia: American Society for Testing and Materials, 1985:165-172.

132 Meskers CG, Fraterman H, van der Helm FC, Vermeulen HM, Rozing PM. Calibration of the "Flock of Birds" electromagnetic tracking device and its application in shoulder motion studies. J Biomech 1999;32(6):629-33.

133 Milgrom C, Giladi M, Simkin A, Stein M, Kashtan H, Margulies J, et al. The normal range of subtalar inversion and eversion in young males as measured by three different techniques. Foot Ankle 1985;6(3):143-5.

134 Milne AD, Chess DG, Johnson JA, King GJ. Accuracy of an electromagnetic tracking device: a study of the optimal range and metal interference. J Biomech 1996;29(6):791-3.

135 Morris JM. Biomechanics of the foot and ankle. Clin Orthop 1977(122):10-7.

136 Mote CD, Jr., Kuo CY. Identification of knee joint models for varus-valgus and internal-external rotations: snow skiing experiments. Journal of Biomechanics 1989;22(3):245-59.

137 Mote CDJ, Johnson RJ, Hauser W, Schaff PS, eds. Skiing Trauma and Safety: ASTM, 1996:58-65.Chow TK, Corbett SW, Farstad DJ. Spectrum of injuries from snowboarding. J Trauma 1996;41(2):321-5.

138 Müller E. Analysis of the biomechanical characteristics of different swinging techniques in alpine skiing. Journal of Sports Sciences 1994;12:261-278.

139 Müller E, Schwameder H, Schiefermüller C. Skiing with carved skis: challenges on performance and safety. In: Fourth World Congress of Biomechanics; 2002; Calgary; 2002.

140 National Snowboard Rider Survey 1994. Marketing Strategies 1994 :1-18.

141 Netter FH. Atlas of Human Anatomy. Second Edition ed. Summit, New Jersey: Novartis; 1997.

142 Niessen W, Müller E, Schwameder H. Force and moment measurements during alpine skiing depending on height position. Internation Society of Biomechanics XVI Conference, 1998:544-547.

143 Nigg BM, Fisher V, Allinger TL, Ronsky JR, Engsberg JR. Range of motion of the foot as a function of age. Foot & Ankle 1992;13(6):336-43.

144 Nigg BM, Skarvan G, Frank CB, Yeadon MR. Elongation and forces of ankle ligaments in a physiological range of motion. Foot & Ankle 1990; 11:30-40.

145 Nixon MA, McCallum BC, Fright WR, Price NB. The effect of metals and interfering fields on electromagnetic trackers. Presence 1998;7:204-218.

146 Oberthaler G, Primavesi C, Niederwieser B, Hertz H. Snowboarding accidents 1991 to 1994--an analysis. Sportverletzung Sportschaden 1995;9(4):118-22.

147 Ozeki S, Yasuda K, Kaneda K, Yamakoshi K, Yamanoi T. Simultaneous strain measurement with determination of a zero strain reference for the medial and lateral ligaments of the ankle. Foot Ankle Int 2002;23(9):825-32.

148 Pankovich AM, Shivaram MS. Anatomical basis of variability in injuries of the medial malleolus and the deltoid ligament. I. Anatomical studies. Acta Orthop Scand 1979;50(2):217-23.

149 Parenteau CS, Viano DC, Petit PY. Biomechanical properties of human cadaveric ankle-subtalar joints in quasi-static loading. J Biomech Eng 1998;120(1):105-11.

150 Paul CC, Janes PC. The snowboarder's talus fracture. In: Mote CDJ, Johnson R, Hauser W, Schaff PS, eds. Skiing Trauma and Safety: ASTM, 1996:388-393.

151 Pigozzi F, Santori N, Di Salvo V, Parisi A, Di-Luigi L. Snowboard traumatology: an epidemiological study. Orthopedics (Thorofare, NJ) 1997;20(6):505-9.

152 Pino EC, Colville MR. Snowboard injuries. American Journal of Sports Medicine 1989;17(6):778-81.

153 Piziali RL, Nagel DA. Modeling of the human leg in ski injuries. Orthopedic Clinics of North America 1976; 7:127-39.

154 Polhemus Incorporated. 3Space Fastrak User's Manual. 2000 Edition, Rev. A.

155 Procter P, Paul JP. Ankle joint biomechanics. Journal of Biomechanics 1982;15(9):627-34.

156 Quiles M, Requena F, Gomez L, Garcia-Sancho L. Functional anatomy of the medial collateral ligament of the ankle joint. Foot Ankle 1983;4(2):73-82.

157 Quinn TP, Mote CD, Jr. Prediction of the loading along the leg during snow skiing. Journal of Biomechanics 1992;25(6):609-25.

158 Quinn TP, Mote CD, Jr., Skinner HB. The effect of ankle constraint on the torsional laxity of the knee during internal-external rotation of the foot. Journal of Biomechanics 1991;24(7):511-25.

159 Quinn TP, Mote CDJ. Optimal design of an uncoupled six-degree-of-freedom dynamometer. In: Johnson R, Mote CDJ, Zelcer J, eds. Skiing Trauma and Safety: ASTM, 1993:94-111.

160 Ramming J, Hull M. Microcomputer - based instrumentation for measuring boot loading in snow skiing. In: Shoup TE, Thacker JG, eds. International Conference on Medical Devices and Sports Equipment. New York: American Society of Mechanical Engineers, 1980:15-21.

161 Rasmussen O, Tovborg-Jensen I. Mobility of the ankle joint: recording of rotatory movements in the talocrural joint *in vitro* with and without the lateral collateral ligaments of the ankle. Acta Orthopaedica Scandinavica 1982;53(1):155-60.

162 Ratzek T, Niedermayer C. Safety binding for snowboards. United States: F2 International Ges. m.b.H., 1998 (patent).

163 Reinschmidt C, van den Bogert AJ, Nigg BM, Lundberg A, Murphy N. Effect of skin movement on the analysis of skeletal knee joint motion during running. Journal of Biomechanics 1997;30(7):729-732.

164 Renström P, Wertz M, Incavo S, Pope M, Ostgaard HC, Arms S, et al. Strain in the lateral ligaments of the ankle. Foot Ankle 1988;9(2):59-63.

165 Roaas A, Andersson GB. Normal range of motion of the hip, knee and ankle joints in male subjects, 30-40 years of age. Acta Orthopaedica Scandinavica 1982; 53:205-8.

166 Rockar PA, Jr. The subtalar joint: anatomy and joint motion. J Orthop Sports Phys Ther 1995;21(6):361-72.

167 Root ML, Weed JH, Sgarlato TE, Bluth DR. Axis of motion of the subtalar joint. J Am Podiatr Ass 1966;56:149-155.

168 Sacco DE, Sartorelli DH, Vane DW. Evaluation of alpine skiing and snowboarding injury in a northeastern state. Journal of Trauma-Injury Infection & Critical Care 1998;44(4):654-9.

169 Sammarco GJ, Burstein AH, Frankel VH. Biomechanics of the ankle: a kinematic study. Orthopedic Clinics of North America 1973;4(1):75-96.

170 Schaff P, Hauser W. 3-D video motion analysis on the slope--A practical way to analyze motion patterns in alpine skiing. In: Johnson R, Mote CDJ, Zelcer J, eds. Skiing Trauma and Safety: ASTM, 1993:169-176.

171 Schaff P, Senner V, Kaiser F. Pressure distribution measurements for the alpine skier--From the biomechanical high tech measurement to its application as swingbeep-feedback system. In: al. Me, ed. Skiing and Science. London: E & FN Spon, 1997:159-172.

172 Schnitzhofer JP. Binding for snowboards. Canada: 1997 (patent).

173 Schrank C, Gaulrapp H, Rosemeyer B. Pattern and risk of injuries of profile athletes in snow boarding. Sportverletz Sportschaden 1999;13(1):8-13.

174 Scott SH, Winter DA. Talocrural and talocalcaneal joint kinematics and kinetics during the stance phase of walking. J Biomech 1991;24(8):743-52.

175 Sepic SB, Murray MP, Mollinger LA, Spurr GB, Gardner GM. Strength and range of motion in the ankle in two age groups of men and women. American Journal of Physical Medicine 1986; 65:75-84.

176 Shealy JE, Ettlinger CF, Buonomo V. Epidemiology of snowboarding injuries: 1988 to 1995. In: Johnson RJ, Mote CDJ, Ekeland A, editors. Skiing Trauma and Safety; 1997: ASTM; 1997. p. 49-59.

177 Shealy JE, Ettlinger CF. Gender-related injury patterns in skiing. In: Mote CDJ, Johnson R, Hauser W, Schaff PS, eds. Skiing Trauma and Safety: ASTM, 1996:45-57.

178 Shealy JE, Sundman PD. Snowboarding injuries on alpine slopes. In: Johnson RJ, Mote CDJ, Binet M-H, eds. Skiing Trauma and Safety: ASTM, 1989:75-81.

179 Shealy JE. Snowboard vs. downhill skiing injuries. In: Johnson R, Mote CDJ, Zelcer J, eds. Skiing Trauma and Safety: ASTM, 1993:241-254.

180 Siegler S, Block J, Schneck CD. The mechanical characteristics of the collateral ligaments of the human ankle joint. Foot & Ankle 1988; 8:234-42.

181 Siegler S, Chen J, Schneck CD. The three-dimensional kinematics and flexibility characteristics of the human ankle and subtalar joints--Part I: Kinematics. Journal of Biomechanical Engineering 1988;110(4):364-73.

182 Siegler S, Wang D, Plasha E, Berman AT. Technique for *in vivo* measurement of the three-dimensional kinematics and laxity characteristics of the ankle joint complex. Journal of Orthopaedic Research 1994; 12:421-31.

183 Singh A, Starkweather K, Hollister A, Jatana S, Lupichuk A. Kinematics of the ankle: a hinge axis model. Foot and ankle 1992;13(8):439-46.

184 Soavi R, Girolami M, Loreti I, Bragonzoni L, Monti C, Visani A, *et al.* The mobility of the proximal tibio-fibular joint. A Roentgen Stereophotogrammetric Analysis on six cadaver specimens. Foot Ankle Int 2000; 21:336-42.

185 St. Pierre RK, Rosen J, Whitesides TE, Szczukowski M, Fleming LL, Hutton WC. The tensile strength of the anterior talofibular ligament. Foot Ankle 1983;4(2):83-5.

186 Stagni R, Leardini A, Ensini A. Recruitment of ankle ligaments fibres during passive flexion. Fourth World Congress of Biomechanics, Calgary, 2002.

187 Stauffer RN, Chao EY, Brewster RC. Force and motion analysis of the normal, diseased, and prosthetic ankle joint. Clin Orthop 1977;127:189-96.

188 Stiehl J. Inman's Joints of the Ankle: 2nd edition. 2 ed. Baltimore: Williams and Wilkins; 1991.

189 Stytz MR, Parrott RW. Using kriging for 3D medical imaging. Computerized Medical Imaging and Graphics 1993;17(6):421-442.

190 Sutherland AG, Holmes JD, Myers S. Differing injury patterns in snowboarding and alpine skiing. Injury 1996;27(6):423-5.

191 Trochu F. A contouring program based on dual kriging interpolation. Engineering with Computers 1993;9:160-177.

192 Ueland O, Kopjar B. Occurrence and trends in ski injuries in Norway. Br J Sports Med 1998;32(4):299-303.

193 van Bergen V. Different possibilities of measuring force transmission between ski and binding. In: al. Me, ed. Skiing and Science. London: E & FN Spon, 1997:189-199.

194 van den Bogert AJ, Smith GD, Nigg BM. *In vivo* determination of the anatomical axes of the ankle joint complex: an optimization approach. Journal of Biomechanics 1994;27(12):1477-88.

195 van Langelaan EJ. A kinematical analysis of the tarsal joints. An X-ray photogrammetric study. Acta Orthop Scand Suppl 1983;204:1-269.

196 Weiss PL, Kearney RE, Hunter IW. Position dependence of ankle joint dynamics--I. Passive mechanics. Journal of Biomechanics 1986; 19:727-35.

197 Weiss PL, Kearney RE, Hunter IW. Position dependence of ankle joint dynamics--II. Active mechanics. Journal of Biomechanics 1986; 19:737-51.

198 Wimmer MA, Holzner R. Constraint forces may influence the measurement of vertical ground reaction forces during slalom skiing. In: al. Me, ed. Skiing and Science. London: E & FN Spon, 1997:208-215.

199 Winter DA. Biomechanics and Motor Control of Human Movement. (Second Edition ed.) New York: John Wiley & Sons, Inc, 1990.

200 Woltring HJ. Model and measurement error influences in data processing. In: Berme N, Cappozzo A, editors. Biomechanics of Human Movement--Applications in Rehabilitation Sport and Ergonomics. Worthigton, Ohio: Bertec Corporation; 1990. p. 203-237.

201 Woltring HJ, Long K, Osterbauer PJ, Fuhr AW. Instantaneous helical axis estimation from 3-D video data in neck kinematics for whiplash diagnostics. J Biomech 1994;27(12):1415-32.

202 Woo SL, Debski RE, Zeminski J, Abramowitch SD, Saw SS, Fenwick JA. Injury and repair of ligaments and tendons. Annu Rev Biomed Eng 2000;2:83-118.

203 Woodburn J, Turner DE, Helliwell PS, Barker S. A preliminary study determining the feasibility of electromagnetic tracking for kinematics at the ankle joint complex. Rheumatology (Oxford) 1999;38(12):1260-8.

204 Wu G, Siegler S, Allard P, Kirtley C, Leardini A, Rosenbaum D, et al. ISB recommendation on definitions of joint coordinate system of various joints for the reporting of human joint motion--part I: ankle, hip, and spine. International Society of Biomechanics. J Biomech 2002;35(4):543-8.

205 Wunderly GS, Hull ML, Maxwell S. A second generation microcomputer controlled binding system for alpine skiing research. Journal of Biomechanics 1988;21(4):299-318.

206 Wunderly GS, Hull ML, Maxwell SM. Measurement of boot loads using a second-generation microcomputer-controlled snow ski binding system. In: Johnson RJ, Mote CDJ, Binet M-H, eds. Skiing Trauma and Safety: ASTM, 1989:181-198.

207 Yoganandan N, Pintar F, Butler J, Reinartz J, Sances A, Jr., Larson SJ. Dynamic response of human cervical spine ligaments. Spine 1989;14(10):1102-10.

208 Zachmann G. Distortion correction of magnetic fields for position tracking. In: Proc Computer Graphics International; 1997; 1997. p. 23-27.

209 Zhang M, Tak-Man Cheung J, Fan Y, Leung AKL. Development of a 3D finite element model of human foot and ankle. In: Fourth World Congress of Biomechanics; 2002; Calgary; 2002.

210 Zollinger H, Gorschewsky O, Cathrein P. Injuries in snowboarding--a prospective study. Sportverletzung Sportschaden 1994;8(1):31-7.

Appendix A Anatomical terminology

A.1 Planes

Three planes of reference can be defined on the human body: the sagittal, the frontal and the transverse planes (Figure A-1). The sagittal plane is defined as the vertical plane parallel to a postero-anterior axis of the head and passing through a mid-point between the two eyes. It is a symmetry plane of the head. By extension to the rest of the body, it is the vertical plane that divides the human body into "symmetric" right and left halves (apart from internal organ locations). The frontal plane is a vertical plane perpendicular to the sagittal plane. It divides the human body into an anterior part and a posterior part. The transverse plane is any plane perpendicular to both the sagittal and frontal planes.

A.2 Sides and ends

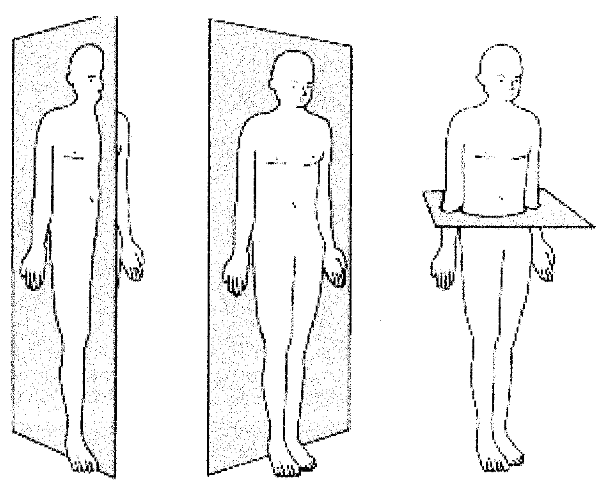

Figure A-1: The anatomical planes of the human body. Adapted from www.physiotherapy.net.au.

The medial side refers to the side that is towards the sagittal plane of the body while lateral refers to the side that is away from the sagittal plane of the body. The part of an appendix or organ that is closest to its attachment point is called the proximal end while the opposite (furthest from its attachment point) is called the distal end.

Appendix B Stereovideography

A stereovideographic protocol was tested during the winter of 2000 at Mont Habitant (Quebec, Canada). As shown in Figure B-1, two Panasonic video cameras were mounted on tripods and located along a course of 4 turns. The cameras were allowed to turn around only one axis, approximately normal to the ground. Two calibration objects of known coordinates were installed at the beginning and at the end of the course. Reflective markers were attached on the snowboarder's shanks and boots. The two cameras filmed the snowboarder as he went down the course. The experiment failed for the following reasons:

- Of more than 20 trials filmed, it was not possible to find one trial which showed the snowboarder during the whole course with the two cameras. The snowboarder was going too fast for the camera operators to follow him.

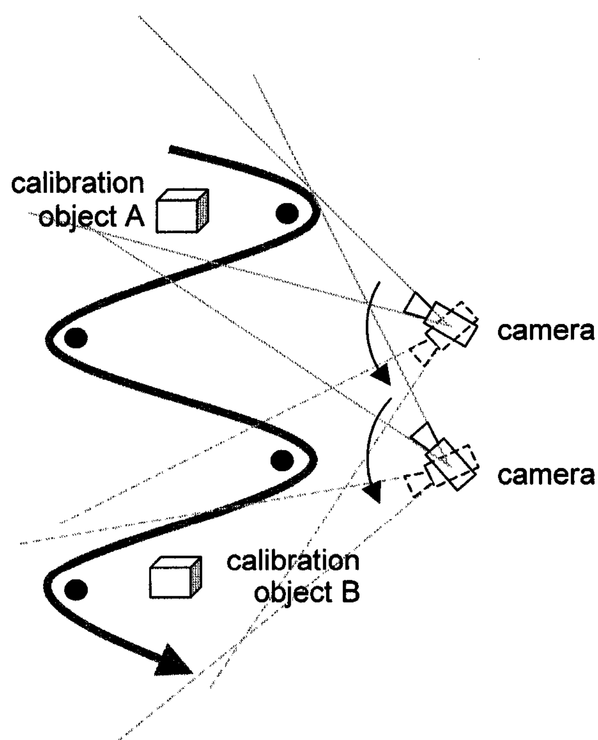

Figure B-1: Stereovideographic set-up.

- Because of the sideway stance of the snowboarder, it was not possible to place the markers on the lower limbs at a position where they could be seen by the cameras throughout one complete turn cycle (one toe turn and one heel turn).
- Even placed over dark pants, the reflective markers were difficult to identify on the videotapes because the experiment was done outside under daylight.

These difficulties are only related to the data acquisition itself and the data processing system (3D stereovideographic reconstruction with camera panning) could not even be tested because no complete usable set of data was acquired.

The stereovideographic technique was abandoned for this project as it was concluded that stereovideography is more suited to a highly controllable environment, like a motion analysis laboratory.

Appendix C Ethics approval and informed consent form

Appendix D Measuring equipment description

The following sections describe the apparatus, computers and software were used in this project.

D.1 Electromagnetic position sensors (Fastrak)

The Fastrak system (Polhemus, Colchester, VT, USA) is a real-time 6-DOF (position and orientation) electromagnetic motion tracker (Figure D-1a). It consists of:

- A source (transmitter). This is a fixed magnetic-dipole transmitting antenna, enclosed in a plastic shell, which emits the magnetic fields and acts as the system's reference frame for receiver measurements.
- One to four sensors (receivers). These are freely movable magnetic-dipole receiving antennas, enclosed in a plastic shell (Figure D-1b), which detect the magnetic fields

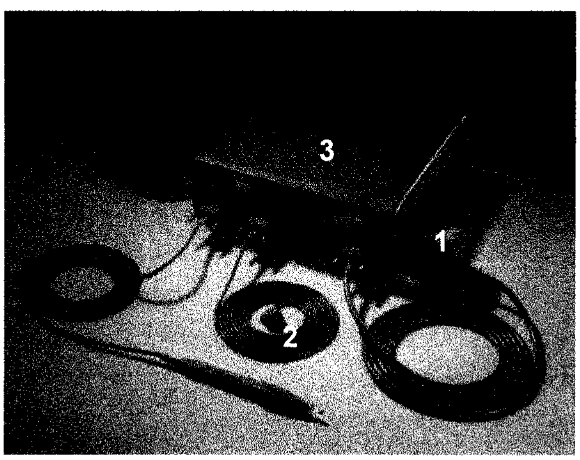

a)

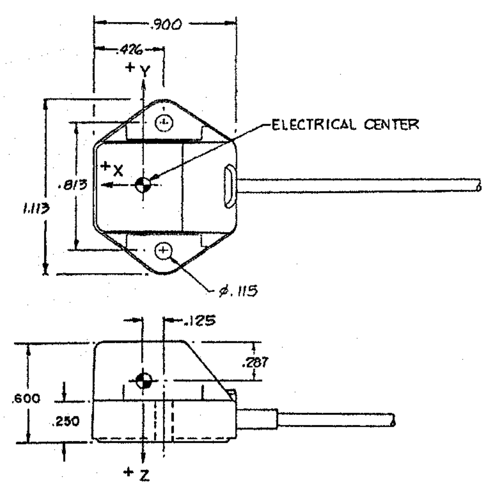

b)

Figure D-1: a) Fastrak system with 1) source, 2) sensor and 3) system electronics unit; b) Fastrak sensor dimensions in inches. (Adapted from Fastrak User's Manual[154], © Polhemus Inc., reproduced with permission).

emitted by the source. Each receiver is a lightweight cube whose position and orientation is precisely measured as it is moved. The receivers are completely passive, having no active voltage applied to them.

- The system electronics unit. This unit contains the hardware and software necessary to generate and sense the magnetic fields, compute the position and orientation, and interface with the host computer via an RS-232 cable and serial port.

Both the source and sensor antennas consist of three mutually orthogonal loops (coils). The loop diameters are kept very small compared to the distance separating the source and sensor so that each loop may be regarded as a point or infinitesimal dipole. Exciting a loop antenna produces an electromagnetic field consisting of a far-field component and a near or induction-field component. Each loop of the source antenna is, in turn, excited with a driving signal; all signals are identical in frequency and phase. Each excitation produces a single axis source dipole. The source excitation is a pattern of three states. Exciting the source results in an output at the sensor of nine values forming a set of three linearly independent vectors. Those three output vectors contain sufficient information to determine the position and orientation of the sensor relative to the source. The nine values are enough to solve for the six unknowns, x, y, z for position and ψ (azimuth), ϕ (elevation), and θ (roll) for orientation (Figure 3-9).

The system allows measurement of up to four sensors. It has a very small latency of 4 ms (the time between the measurement and the output of the values) and the measurements are sampled at a rate of 120 Hz. If more than one sensor is used, the sensors are updated successively rather than simultaneously. Therefore, with four sensors, each sensor is updated at 30 Hz (120 Hz divided by the number of sensors). Data is transmitted to the host at a rate of up to 100 Kbytes/sec. According to the manufacturer's specifications[154], positional and rotational accuracies are 0.8 mm and 0.15° RMS (root mean square), respectively. The corresponding resolutions are 0.005 mm/mm of distance between the source and the sensor and 0.025°. The standard range of measurement is a hemisphere with a 3 m radius.

The system is sensitive to perturbations of the magnetic field due to the presence of other magnetic fields or large metallic objects near the source, particularly ferromagnetic materials or highly conductive materials. For instance, a cathode ray tube (with the power on), and mild steel or aluminium objects would cause measurement errors while plastic, wood, ceramic, biological tissue or 316 stainless steel would not.

D.2 Computer hardware and software

An Epson laptop computer (80486 running under DOS 6.2) was used for the data acquisition. The data analysis was done with the MatLab software (Mathworks, Natick, MA) running on a Pentium 3 computer.

D.3 Digital video camera (JVC)

The high-speed digital video camera (JVC, model DVL9800u, Figure D-2) records video and audio on Mini DV Tape at a rate of up to 200Hz. Its zoom provides magnification in the range from 10x to 200x. One camera was used in the project.

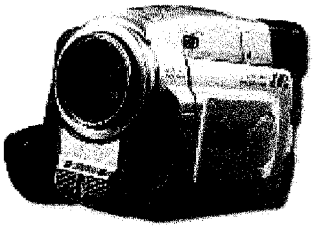

Figure D-2: High speed digital camera (JVC DVL9800u). Image adapted from www.jvc.ca.

Appendix E Pre-testing with the Fastrak system

E.1 Battery life

A test was performed to evaluate the behaviour of two types of batteries powering both the laptop computer and the Fastrak system. Since the Fastrak is normally powered by a source with constant voltage and batteries are known to have a decreasing voltage as they empty their charge, it was suspected that the measurements made when the Fastrak system is running on batteries would vary through time. The goal of these tests was to evaluate this variation with two different battery packs. Each battery packs consisted of two 12-Volt PowerSonic batteries connected in series:

- PS1229 (2.9 A-hr, 0.95 kg each).
- PS1270 (7.0 A-hr, 2.6 kg each).

Each battery pack was connected to the Fastrak and laptop computer. A series of 10 measurements were taken and averaged every 15 minutes for the 1229 and 30 minutes for the 1270, until the laptop would automatically shutdown because the voltage was too low. During the entire test, the source and one sensor were not moved.

Figure E-1 presents the variation of voltage, position and orientation readings with time. At least 22.5 V were necessary to keep the laptop computer running. This limit was reached after 3.5 hours of continuous operation for the PS-1270 and 1 hour with the PS-1229. The PS-1270 had a higher voltage than the PS-1229 at full charge (25.3 V and 24.6 V respectively). This resulted in big variations in the measurements with PS-1270 until 24.5 V was reached after one hour. Nevertheless, variations in positions and orientations (1.5 mm and 0.34 deg) after one hour of operation were still greater than the Fastrak precision of 0.8 mm and 0.15 deg. The PS-1229 lasted only an hour but

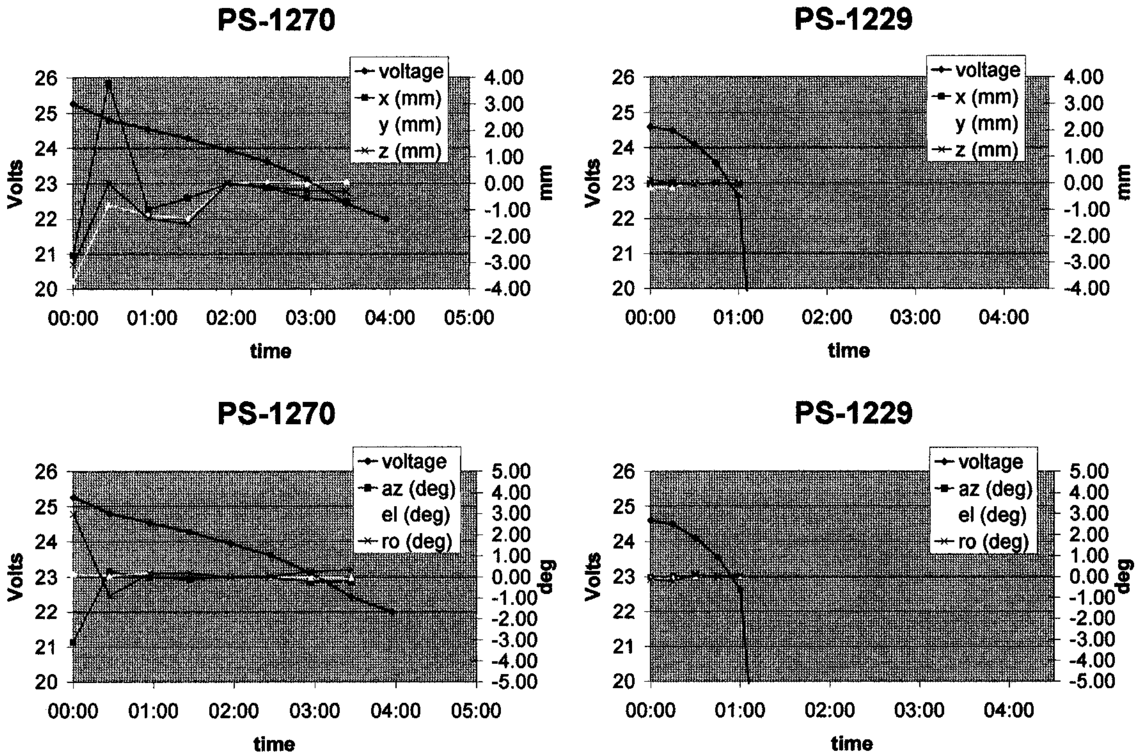

Figure E-1: Battery pack comparison: PS-1270 (left row) versus PS-1229 (right row). Voltage, position values (top line) and orientation values (bottom line) are plotted with time (hr:min). Az: azimuth; el: elevation; ro: roll.

measurements variation stayed in a range below the Fastrak precision (0.16 mm, 0.21 deg).

E.2 Metallic parts

A test was performed to evaluate the effect of metallic parts in the strap bindings and step-in bindings on data measured with the Fastrak system. The source and one sensor were attached to a piece of wood approximately 30 cm apart, so as to keep constant their relative position and orientation. If static metallic noise is present, the Fastrak system will record different position and orientation values while moving the piece of wood through space. Measurements were first done without the snowboard and binding. Then source was placed approximately on the centre of the snowboard and the sensor at different heights above the binding (heel side), while keeping them both attached to the piece of wood. With the step-in binding, the mating part on the boot is metallic. It was unscrewed from the boot and locked in position in the binding during the tests.

Figure E-2 shows how the position and orientation values vary with the vertical distance between the sensor and the snowboard. The sensor that is placed on the foot of the snowboarder is located approximately 10 cm above the snowboard with the strap bindings and 6 cm with the step-in bindings. At these distances, the step-in bindings still caused significant measurement errors as high as 5 mm for position and over 1 deg for orientation. In comparison, the effect of metallic parts in strap bindings disappeared above 2 cm over the board.

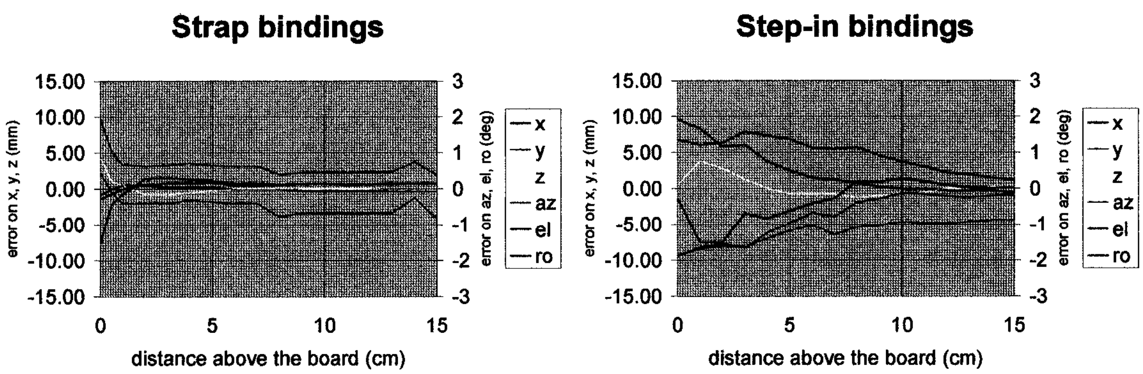

Figure E-2: Effect of metallic parts in strap bindings (left) and step-in bindings (right) on position and orientation measurements with the Fastrak. Az: azimuth; el: elevation; ro: roll.

Appendix F Measurements with the Fastrak and a stylus

Each Fastrak sensor measures the position of its centre, as shown in Figure D-1b, which makes it difficult to use a sensor to measure a precise point, such as an anatomical landmark. One way around this problem is to rigidly attach a stylus to a sensor, so that the tip of the sensor stays at the same position in the sensor coordinate system. If the vector between the origin of the sensor coordinate system and the stylus tip is known, then one set of measurements with the sensor (6 DOF) can be converted into the position of the stylus tip (3 DOF).

The present section describes the stylus and the algorithm used to "calibrate" the stylus tip and convert raw measurements into stylus tip positions. A validation of the technique is also presented.

F.1 Stylus design

The stylus (Figure F-1) is made of a 316 stainless steel tip (1.6 mm diameter) glued into a plastic rod (13 mm diameter). The rod is filleted and fastened with screws in a plastic cubic box (25 mm). The cubic box has two holes for attaching the sensor with 316

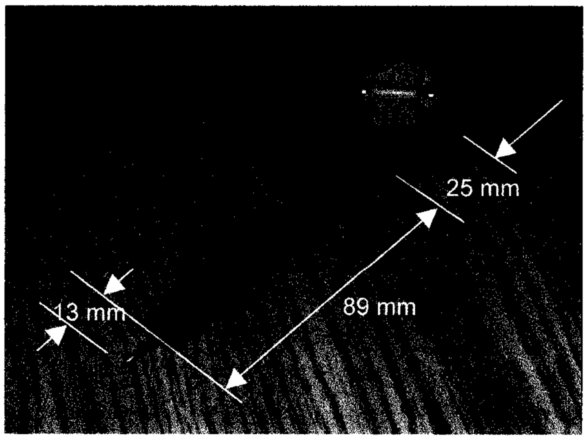

Figure F-1: Stylus tip with sensor.

stainless steel screws. The sensor is attached in such an orientation that its tip has only positive coordinate components in the local coordinate system of the sensor. This will be important in the calibration procedure, as will be seen in the next section.

F.2 Calibration algorithm

The procedure for calibrating the stylus in based on several measurements of the same point by the stylus tip, but with the stylus at different orientations. In practice, the stylus tip is placed on a non-slippery horizontal surface, with the stylus vertical. The stylus is then slightly tilted (approximately 20° from the vertical) and one measurement is taken. The stylus is then moved at several other orientations, describing an upside-down cone with its summit at the stylus tip, and measurements are taken at each position. The measurements are noted $(x_i \quad y_i \quad z_i \quad \psi_i \quad \phi_i \quad \theta_i)$.

Euler angles (ψ, ϕ, θ) can be transformed into a 3-by-3 rotation matrix (R) using

$$R = \begin{bmatrix} \cos\psi & -\sin\psi & 0 \\ \sin\psi & \cos\psi & 0 \\ 0 & 0 & 1 \end{bmatrix} \begin{bmatrix} \cos\phi & 0 & \sin\phi \\ 0 & 1 & 0 \\ -\sin\phi & 0 & \cos\phi \end{bmatrix} \begin{bmatrix} 1 & 0 & 0 \\ 0 & \cos\theta & -\sin\theta \\ 0 & \sin\theta & \cos\theta \end{bmatrix}. \qquad \text{[F-1]}$$

Let (x_0, y_0, z_0) be the position of the stylus tip in the global coordinate system (Fastrak source) and (u, v, w) be the stylus vector in the local coordinate system (Fastrak sensor), as shown in Figure F-2.

The rotation matrix (R) calculated above converts vectors expressed in the local coordinate system into vectors in the global coordinate system. For instance, for the stylus vector,

$$\begin{pmatrix} u \\ v \\ w \end{pmatrix}_G = [R] \begin{pmatrix} u \\ v \\ w \end{pmatrix}_L . \qquad \text{[F-2]}$$

Thus, the measurements must satisfy

$$\begin{bmatrix} 1 & 0 & 0 & \\ 0 & 1 & 0 & -[R_1] \\ 0 & 0 & 1 & \\ 1 & 0 & 0 & \\ 0 & 1 & 0 & -[R_2] \\ 0 & 0 & 1 & \\ 1 & 0 & 0 & \\ 0 & 1 & 0 & -[R_3] \\ 0 & 0 & 1 & \\ & \cdots & & \\ 1 & 0 & 0 & \\ 0 & 1 & 0 & -[R_N] \\ 0 & 0 & 1 & \end{bmatrix} \begin{pmatrix} x_0 \\ y_0 \\ z_0 \\ u \\ v \\ w \end{pmatrix} = \begin{pmatrix} x_1 \\ y_1 \\ z_1 \\ x_2 \\ y_2 \\ z_2 \\ x_3 \\ y_3 \\ z_3 \\ \cdots \\ x_N \\ y_N \\ z_N \end{pmatrix} . \qquad \text{[F-3]}$$

When more than two sets of measurements are used, the system would be over-determined. In such cases, the system is solved, in the least square sense, using MatLab's NNLS function (Non-Negative Least Squares). This function requires all unknowns (x_0, y_0, z_0, u, v, w) to be non-negative. This means that, unlike shown in Figure F-2, the stylus tip must be located at a place at which all its position components (x_0, y_0, z_0) would be non negative and the stylus must be attached to the sensor in such a way that the vector (u, v, w) would have no negative component.

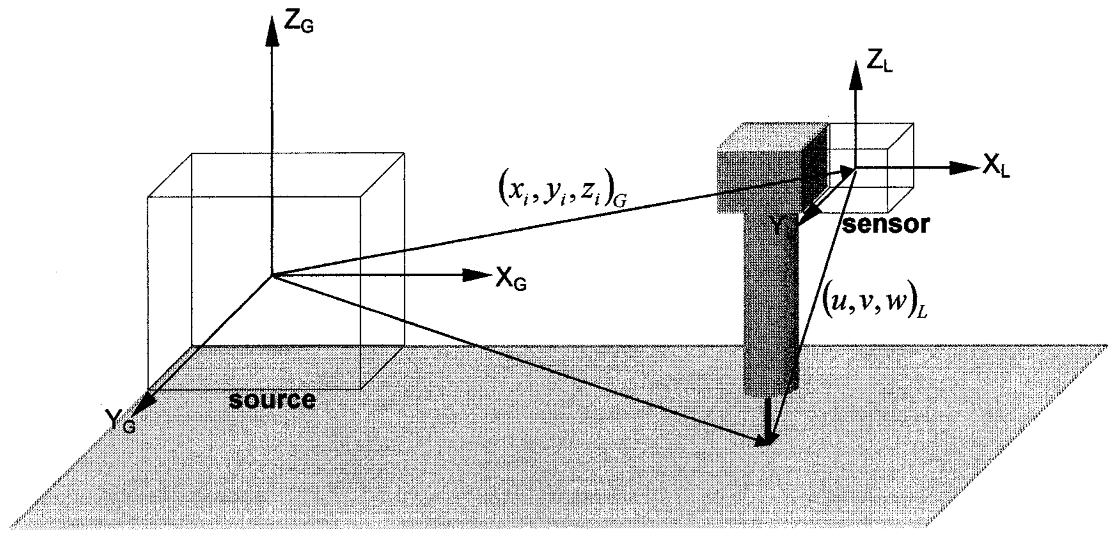

Figure F-2: Vectors in the global (G) and local (L) coordinate systems for the stylus calibration.

The calibration, expressed as the three components of the stylus vector (u,v,w), can then be applied to any sensor measurement to calculate the position of the stylus tip using equations [F-1] and [F-2].

F.3 Fastrak accuracy with a calibrated stylus

A validation was performed to verify the accuracy of the measurements taken with the stylus. The positions of 13 small conic holes on three of the faces of a rectangular box made of acrylic were measured with the MicroScribe (Immersion Corp., San Jose, CA), an articulated electro-mechanical measuring arm with 0.3 mm accuracy. The same 13 points were then measured with the stylus attached to a Fastrak sensor outside the lab at -10°C. The two sets of measurements were matched using a least square algorithm and the RMS (root mean square) difference between their coordinates was calculated. The RMS errors ranged from 0.6 to 0.9 mm. This result demonstrates that, if properly calibrated, the stylus would not appreciably reduce the accuracy of the Fastrak sensors, which is 0.8 mm according to the manufacturer.

Appendix G Static metallic noise correction

This section presents the jig and mathematical algorithm that were used for the static metallic noise correction, and tests performed with two types of snowboard equipment.

G.1 Design of jig

A jig (Figure G-1) was built to measure a 3D grid of positions and orientations, with and without metallic noise. All parts are made of acrylic, except for nuts and bolts, which are made of non-ferromagnetic 316 stainless steel. Four Fastrak sensors are bolted on an

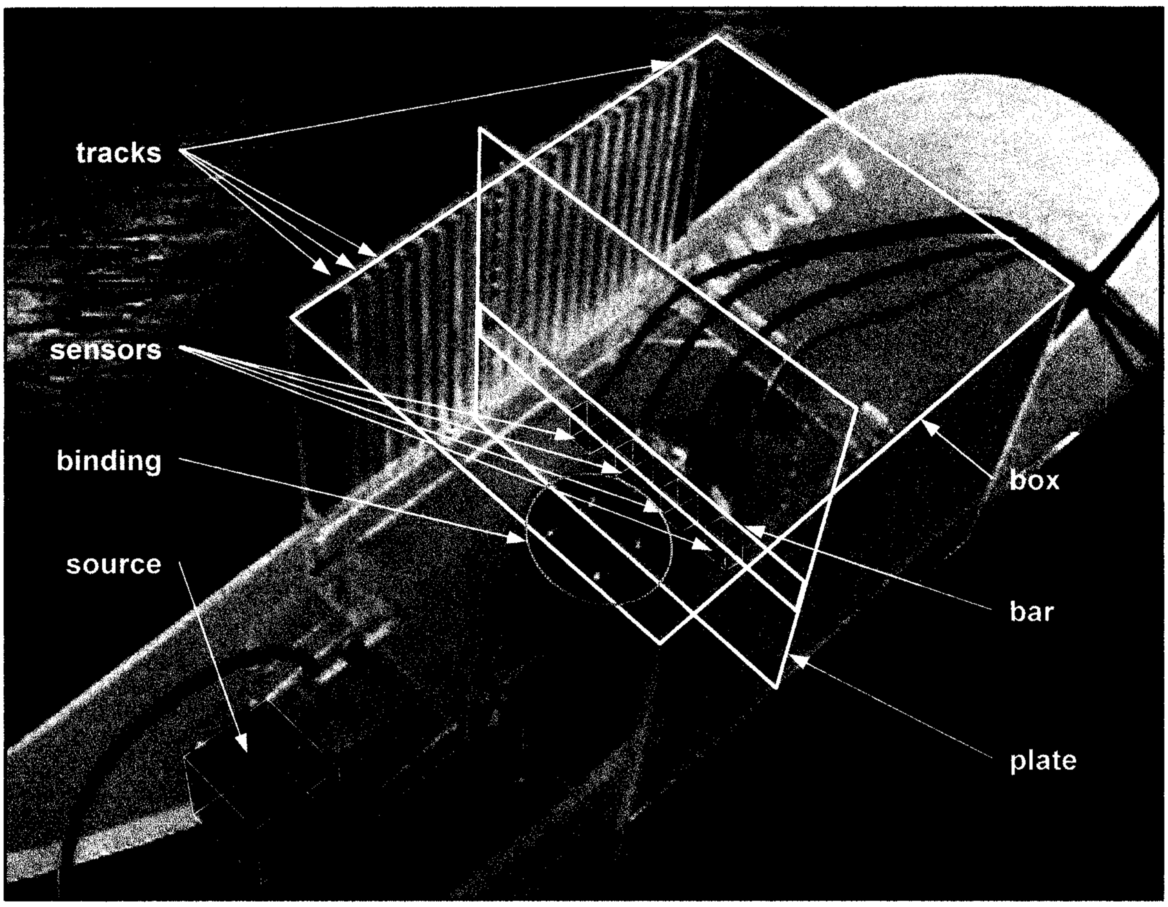

Figure G-1: Picture of the acrylic jig used for metallic noise correction, mounted over the right foot step-in binding. Important parts are outlined in white.

acrylic bar. The bar has equally spaced holes (0.4065 in or 10.3 mm centre to centre) to bolt the sensors at different horizontal positions along the bar. The bar is itself bolted to an acrylic plate. Just like the bar, the plate has two series of equally spaced holes (0.5 in or 12.7 mm centre to centre) near its two vertical edges, allowing bolting the bar horizontally at different vertical positions along the plate. The plate is inserted vertically in two tracks located on two parallel faces of a box with no top or bottom face. Two series of equally spaced tracks (0.5 in or 12.7 mm centre to centre) allow one to move the plate to different repeatable positions along the long axis of the snowboard. The box is roughly centred on the snowboard binding and is attached to the source through a telescopic, adjustable linkage. The source is attached to the snowboard via a polycarbonate part described in section 3.3.2.

When measurements are taken, a range of tracks on the box, a range of holes on the plate and a range of holes on the bar are selected. Lower resolution can also be selected by choosing to skip one or more positions on the holes or tracks. To minimise the time needed for the measurements, the points are measured in such an order that the manipulation that is most often done is to move the plate from one track to the next, and the manipulation that is least often done is to move the sensors along the bar. The jig does not allow measuring multiple orientations at every position. However, Day *et al.*[118] have demonstrated that measuring multiple orientations at every position does not significantly improve orientation correction over measuring only one orientation.

G.2 Three-dimensional geometrical kriging

Kriging (see Appendix H) is used to solve the problem of metal mapping and compensation in two steps[49]:

1. A 3D field of deformation is calculated from two sets of control points measured on the same grid in two states, the initial state (with static metallic noise) and the final state (without static metallic noise).
2. The 3D deformation is applied to any new point measured with static metallic noise.

The j control points in their initial state are denoted as

$$\widetilde{P}_j = \begin{bmatrix} \widetilde{x}_j \\ \widetilde{y}_j \\ \widetilde{z}_j \end{bmatrix} \qquad \text{[G-1]}$$

while the same control points in their final state are denoted as

$$P_j = \begin{bmatrix} x_j \\ y_j \\ z_j \end{bmatrix}. \qquad \text{[G-2]}$$

Then, the equation system that must be solved is

$$\begin{aligned} (x)_i &= a_x(\widetilde{x}_i, \widetilde{y}_i, \widetilde{z}_i) + \sum_{j=1}^{n} b_{xj} K_x(\widetilde{h}_{ij}) \\ (y)_i &= a_y(\widetilde{x}_i, \widetilde{y}_i, \widetilde{z}_i) + \sum_{j=1}^{n} b_{yj} K_y(\widetilde{h}_{ij}) \\ (z)_i &= a_z(\widetilde{x}_i, \widetilde{y}_i, \widetilde{z}_i) + \sum_{j=1}^{n} b_{zj} K_z(\widetilde{h}_{ij}) \end{aligned} \qquad \text{[G-3]}$$

$$\begin{aligned} \sum_{i=1}^{N} b_i &= 0 \\ \sum_{i=1}^{N} b_i \widetilde{x}_i &= 0 \\ \sum_{i=1}^{N} b_i \widetilde{y}_i &= 0 \\ \sum_{i=1}^{N} b_i \widetilde{z}_i &= 0 \end{aligned} \qquad \text{[G-4]}$$

where $a_x(\tilde{x}_i, \tilde{y}_i, \tilde{z}_i)$ is the drift for the x deformation,

$a_y(\tilde{x}_i, \tilde{y}_i, \tilde{z}_i)$ is the drift for the y deformation,

$a_z(\tilde{x}_i, \tilde{y}_i, \tilde{z}_i)$ is the drift for the z deformation,

b_{xj} are the fluctuation coefficients for the x deformation,

b_{yj} are the fluctuation coefficients for the y deformation,

b_{zj} are the fluctuation coefficients for the z deformation,

$\tilde{h}_{ij} = \sqrt{(\tilde{x}_i - \tilde{x}_j)^2 + (\tilde{y}_i - \tilde{y}_j)^2 + (\tilde{z}_i - \tilde{z}_j)^2}$ is the Euclidean distance between points $\tilde{P}_i$ and $\tilde{P}_j$,

$K_x(\tilde{h})$ is the generalized covariance for the x deformation,

$K_y(\tilde{h})$ is the generalized covariance for the y deformation,

$K_z(\tilde{h})$ is the generalized covariance for the z deformation.

In this case, a linear drift and linear covariance are used for each deformation. For each dimension (x, y and z), a set of drift and covariance parameters (a and b) must be calculated. For example, for the x dimension, the system to solve is

$$\begin{pmatrix} x_1 \\ x_2 \\ \cdots \\ x_N \\ 0 \\ 0 \\ 0 \\ 0 \end{pmatrix} = \begin{bmatrix} \tilde{h}_{11} & \tilde{h}_{12} & \cdots & \tilde{h}_{1N} & 1 & \tilde{x}_1 & \tilde{y}_1 & \tilde{z}_1 \\ \tilde{h}_{21} & \tilde{h}_{22} & \cdots & \tilde{h}_{2N} & 1 & \tilde{x}_2 & \tilde{y}_2 & \tilde{z}_2 \\ \cdots & \cdots & & \cdots & \cdots & \cdots & \cdots & \cdots \\ \tilde{h}_{N1} & \tilde{h}_{N2} & \cdots & \tilde{h}_{NN} & 1 & \tilde{x}_N & \tilde{y}_N & \tilde{z}_N \\ 1 & 1 & \cdots & 1 & 0 & 0 & 0 & 0 \\ \tilde{x}_1 & \tilde{x}_2 & \cdots & \tilde{x}_N & 0 & 0 & 0 & 0 \\ \tilde{y}_1 & \tilde{y}_2 & \cdots & \tilde{y}_N & 0 & 0 & 0 & 0 \\ \tilde{z}_1 & \tilde{z}_2 & \cdots & \tilde{z}_N & 0 & 0 & 0 & 0 \end{bmatrix} \begin{pmatrix} (b_x)_1 \\ (b_x)_2 \\ \cdots \\ (b_x)_N \\ (a_x)_1 \\ (a_x)_2 \\ (a_x)_3 \\ (a_x)_4 \end{pmatrix} \qquad \text{[G-5]}$$

The minimum number of control points to have a single solution to the system corresponds to the number of parameters in the drift, 4 in the case of a linear drift. After the drift and covariance parameters are computed, they can be inserted in Equation [G-5] to compensate for distortion of the magnetic field on other points measured in the presence of static metallic noise.

For orientations, the drift will be a function of the three position coordinates (x, y and z) and of the orientation measured at that position, while the covariance is the same as for the positions. For instance, for the roll (θ), Equation [G-5] becomes:

$$\begin{pmatrix} \theta_1 \\ \theta_2 \\ \cdots \\ \theta_N \\ 0 \\ 0 \\ 0 \\ 0 \\ 0 \end{pmatrix} = \begin{bmatrix} \tilde{h}_{11} & \tilde{h}_{12} & \cdots & \tilde{h}_{1N} & 1 & \tilde{x}_1 & \tilde{y}_1 & \tilde{z}_1 & \tilde{\theta}_1 \\ \tilde{h}_{21} & \tilde{h}_{22} & \cdots & \tilde{h}_{2N} & 1 & \tilde{x}_2 & \tilde{y}_2 & \tilde{z}_2 & \tilde{\theta}_2 \\ \cdots & \cdots & & & \cdots & \cdots & \cdots & \cdots & \cdots \\ \tilde{h}_{N1} & \tilde{h}_{N2} & \cdots & \tilde{h}_{NN} & 1 & \tilde{x}_N & \tilde{y}_N & \tilde{z}_N & \tilde{\theta}_N \\ 1 & 1 & \cdots & 1 & 0 & 0 & 0 & 0 & 0 \\ \tilde{x}_1 & \tilde{x}_2 & \cdots & \tilde{x}_N & 0 & 0 & 0 & 0 & 0 \\ \tilde{y}_1 & \tilde{y}_2 & \cdots & \tilde{y}_N & 0 & 0 & 0 & 0 & 0 \\ \tilde{z}_1 & \tilde{z}_2 & \cdots & \tilde{z}_N & 0 & 0 & 0 & 0 & 0 \\ \tilde{\theta}_1 & \tilde{\theta}_2 & \cdots & \tilde{\theta}_N & 0 & 0 & 0 & 0 & 0 \end{bmatrix} \begin{pmatrix} (b_\theta)_1 \\ (b_\theta)_2 \\ \cdots \\ (b_\theta)_N \\ (a_\theta)_1 \\ (a_\theta)_2 \\ (a_\theta)_3 \\ (a_\theta)_4 \\ (a_\theta)_5 \end{pmatrix} \qquad \text{[G-6]}$$

G.3 *Example of static metallic noise compensation*

The metal mapping and compensation algorithm was implemented in MatLab. Measurements were done with the Fastrak on the jig without the snowboard and with the jig installed on the left step-in binding and the freeride snowboard (Figure G-2). Validation of the technique has only been done for positions, but not for orientations.

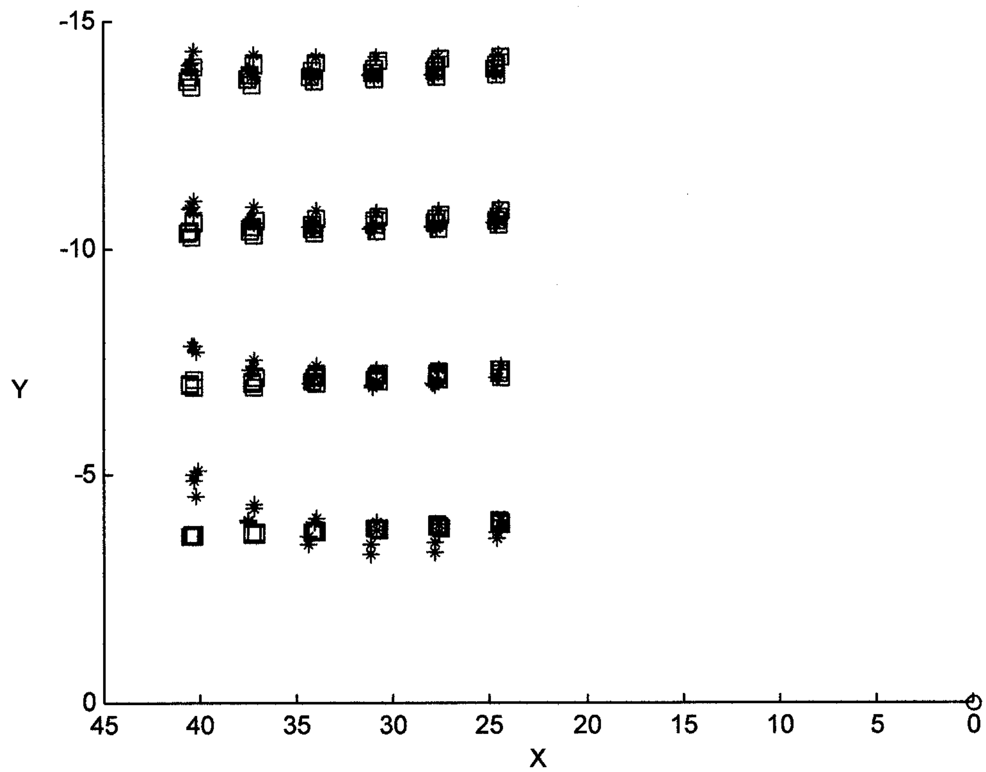

Figure G-2: Positions (in cm) measured on the jig for the static metallic noise compensation with the freeride snowboard and step-in bindings (stars) and without the snowboard (squares). The source is displayed as a circle at the origin of the coordinate system (bottom right corner of the graph). The snowboard is parallel to the *x* axis and normal to the *y* axis.

Appendix H Kriging

Kriging is an interpolation technique developed in the geosciences for estimating ore deposit spatial distributions. It was developed for predicting a spatial random process and has been mathematically proven to be the statistically optimal, linear, unbiased, estimation technique for spatially distributed data[189,191].

Values (X,u) are interpolated or extrapolated between measurements u_i of a phenomenon at taken locations X_i for $1 \le i \le N$, where the position vector is $X = x$ or $X = (x,y)$ or $X = (x,y,z)$ in the 1D, 2D and 3D formulations respectively. An approximate function $u(X)$ is then constructed such that

$$u(X_i) = u_i, \quad 1 \le i \le N. \tag{H-1}$$

In its dual formulation[191], the unknown function $u(X)$ is decomposed to the sum of two functions

$$u(X) = a(X) + b(X) \tag{H-2}$$

where $a(X)$ is the drift or average behaviour of the function, and $b(X)$ is the fluctuation or error term of the function. The choice of the drift function is arbitrary. It can be a constant

$$a(X) = a_1, \tag{H-3}$$

linear

$$a(X) = a_1 + a_2 x + a_3 y + a_4 z, \tag{H-4}$$

quadratic

$$a(X)=a_1+a_2x+a_3y+a_4z+a_5x^2+a_6xy+a_7xz+a_8y^2+a_9yz+a_{10}z^2, \qquad \text{[H-5]}$$

etc. The fluctuation term adjusts the evaluation function $u(X)$ so that it passes through the interpolation points. It depends on N parameters b_j, weighted by correction functions $g_j(X)$ for each observation point as follows:

$$b(X)=\sum_{j=1}^{n} b_j g_j(X). \qquad \text{[H-6]}$$

These correction functions $g_j(X)$ depend on the Euclidean distance $h=|X-X_j|$ and a shape function $K(h)$ called the generalized covariance. Thus,

$$b(X)=\sum_{j=1}^{n} b_j K(|X-X_j|). \qquad \text{[H-7]}$$

The generalized covariance can have many forms. For example, it can be linear

$$K(h)=h, \qquad \text{[H-8]}$$

logarithmic

$$K(h)=h^2 \ln h, \qquad \text{[H-9]}$$

or cubic

$$K(h)=h^3. \qquad \text{[H-10]}$$

The generalized covariance must satisfy the non-bias conditions

$$\sum_{i=1}^{N} b_i = 0$$
$$\sum_{i=1}^{N} b_i x_i = 0$$
$$\sum_{i=1}^{N} b_i y_i = 0 \qquad \text{[H-11]}$$
$$\sum_{i=1}^{N} b_i z_i = 0$$

Appendix I Propagation of uncertainty

I.1 Fastrak system precision

To evaluate the effect of the Fastrak system precision, one trial with one snowboarder was randomly selected. From this trial, a sample of kinematic data representing 20% of the recorded points was randomly selected. Normally distributed random values centred on zero were added to the position and orientation values of the kinematic data points, with a standard deviation of 0.8 mm for position values and 0.15° for orientation values, which is the precision of the Fastrak system as reported by the manufacturer. Standard deviation of twice and four times the values for position and orientation were also used to evaluate the sensitivity to measurement uncertainties. For each combination of standard deviations, 10 different kinematic data files were generated. The ankle rotation values were calculated for each kinematic data file. The standard deviation of the differences between the rotation values calculated with the intact and modified kinematic data is reported in Table 6-1.

I.2 Skin movement artefact

Using methodology similar to the one for the Fastrak system precision, the effect of the measurement uncertainty due to skin movement artefact was also evaluated. The effect of skin movement artefacts on measurements with optical markers has been documented in the literature. Skin movement has been shown to vary widely with marker location. For instance, markers located over big muscles or close to joints were found to be the most affected by movement of the underlying soft tissue. However, the published studies rarely used markers placed in similar locations as in the present study. Among the closest, Cappozzo et al.[32] reported x, y, and z components of skin movement artefact between 6 and 10 mm for a marker located on the shank over the tibialis anterior, the muscle responsible for dorsiflexion of the ankle. The marker in the present study was located over the antero-medial part of the tibia where there is no underlying muscle. Therefore, an uncertainty of 8 mm is considered an overestimate of the skin movement artefact for the present study. Similarly, Maslen and Ackland[128] observed 2 to 6 mm of vertical and horizontal displacements of a skin-marker located over the calcaneus. However, this marker was located on the medial side of the calcaneus (sustentaculum tali) while the one used in the present study was located on the posterior part of the calcaneus, below tendo calcaneus Achilli insertion point, a location further from joint centers and thus expected to undergo less movement of the underlying soft tissues. An uncertainty of 4 mm is considered an overestimate of the skin movement artefact for the foot sensor of the present study.

Electromagnetic sensors used in the present study have 3 translational and 3 rotational DOF, while optical markers only have 3 translational DOF. The literature only reports skin movement artefact with optical markers. Therefore, some assumptions must be done to estimate the rotational skin movement artefacts (Figure I-1). For the shank sensor, the greatest rotation is expected to be in the plane of contact with the skin, since the sensor is placed over a very flat part of the tibia and thin underlying soft tissues. The thermoplastic plate that acts as an interface between the skin and sensor is about 80 mm long. If each of its extremities moves by 8 mm in opposite directions, the plate is rotated by less than 3°. For the foot sensor, the thermoplastic heel cup is shaped like a dome and is expected to move around its centre of curvature. With a radius of curvature of the heel cup of approximately 40 mm, the expected rotation due to a 4 mm skin translation is less than 6°.

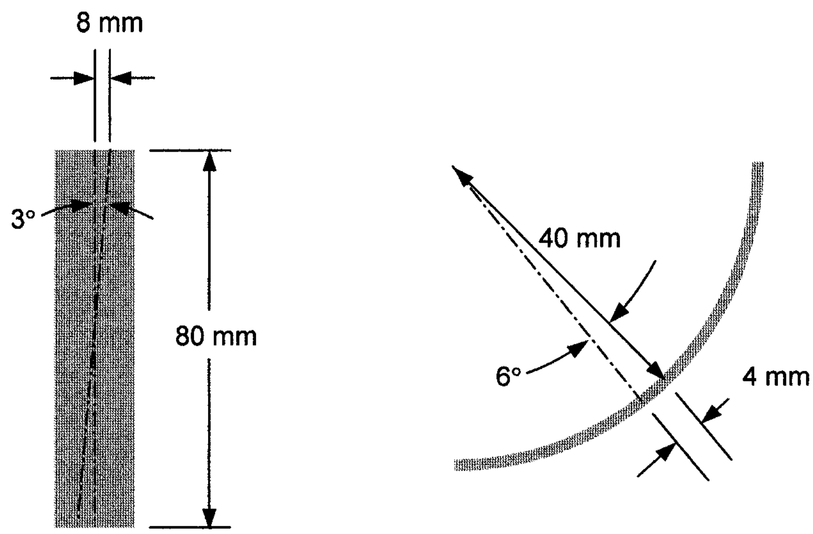

Figure I-1: Assumptions for rotational skin movement artefacts of the shank sensor (left) and foot sensor (right).

Since those values are all conservative estimations of the skin movement artefact in conditions worse than those of the present study, the effect of uncertainty values of 0.25, 0.5 and 1.0 times these estimations were calculated and are presented in Table 6-1.

I.3 Axes of rotation

The two axes of rotation of the ankle joint complex have been shown to have moving instantaneous helical axes, a concept introduced by Woltring[201]. Leardini *et al.*[110] reported the intra-individual linear dispersion (d_{eff}) and angular dispersion (χ_{eff}) of the subtalar joint axis measured on 6 cadaver ankle specimens and calculated using the method described by Woltring[200] (see equations [I-19], [I-20], and [I-21] below). Averaged over all specimens, the 10.475 mm linear dispersion and 7.05° angular dispersion represent the standard deviation of the position and orientation of the subtalar joint axis.

Bottlang *et al.*[22] reported the orientation of the talocrural joint axis in the frontal and transverse planes measured on 6 cadaver specimens at 8 different DF/PF values. In order to obtain a direction vector $\vec{n} = x\vec{i} + y\vec{j} + z\vec{k}$ from its projected orientations α and β, the following equations were developed (see Figure I-2).

$$\sin\alpha = \frac{x}{a} \qquad \text{[I-24]}$$

$$\sin\beta = \frac{y}{b}. \qquad \text{[I-25]}$$

For a unit vector $\vec{n}$,

$$y^2 + a^2 = 1 \qquad \text{[I-26]}$$

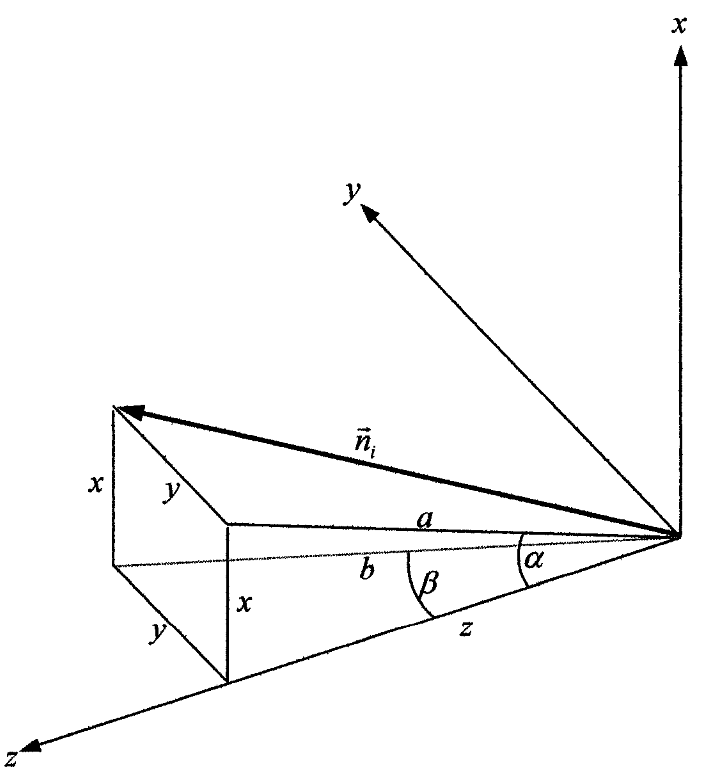

Figure I-2: Projected orientations of direction vector.

$$x^2 + b^2 = 1 \quad [I\text{-}27]$$

$$x^2 + y^2 + z^2 = 1. \quad [I\text{-}28]$$

Isolating a in [I-24] and substituting in [I-26],

$$y^2 + \frac{x^2}{\sin^2 \alpha} = 1. \quad [I\text{-}29]$$

Similarly for b,

$$x^2 + \frac{y^2}{\sin^2 \beta} = 1. \quad [I\text{-}30]$$

Then, solving [I-28], [I-29] and [I-30] for x, y and z, yields

$$x = \sqrt{\frac{AB - A}{AB - 1}} \quad [I\text{-}33]$$

where $A = \sin^2 \alpha$ and $B = \sin^2 \beta$,

$$y = \sqrt{1 - \frac{x^2}{A}} \quad [I\text{-}34]$$

$$z = \sqrt{1 - x^2 - y^2}. \quad [I\text{-}35]$$

The angular dispersion was then calculated from the direction vectors corresponding to Bottlang's data using Woltring's equations[200]. If $\vec{n}_i$ is the direction vector of the i^{th} axis measured, then

$$Q_i = I - \vec{n}_i \vec{n}_i' \quad [I\text{-}19]^{200}$$

$$Q = \frac{1}{n}\sum_{i=1}^{n} Q_i \qquad \text{[I-20]}^{200}$$

Then, finding the smallest eigenvalue λ of matrix Q, the angular dispersion is obtained by

$$\chi_{eff} = \arcsin\left(\sqrt{\lambda}\right) \qquad \text{[I-21]}^{200}$$

For Bottlang's data, the angular dispersion of the talocrural joint was 3.8°. The linear dispersion could not be calculated from Bottlang's data.

Ten sets of one new talocrural and one new subtalar axis were randomly generated with normally distributed uncertainties and 0.5, 1 and 2 times these standard deviations. These uncertainties propagated to the ligament strains as shown in Table 6-2.